

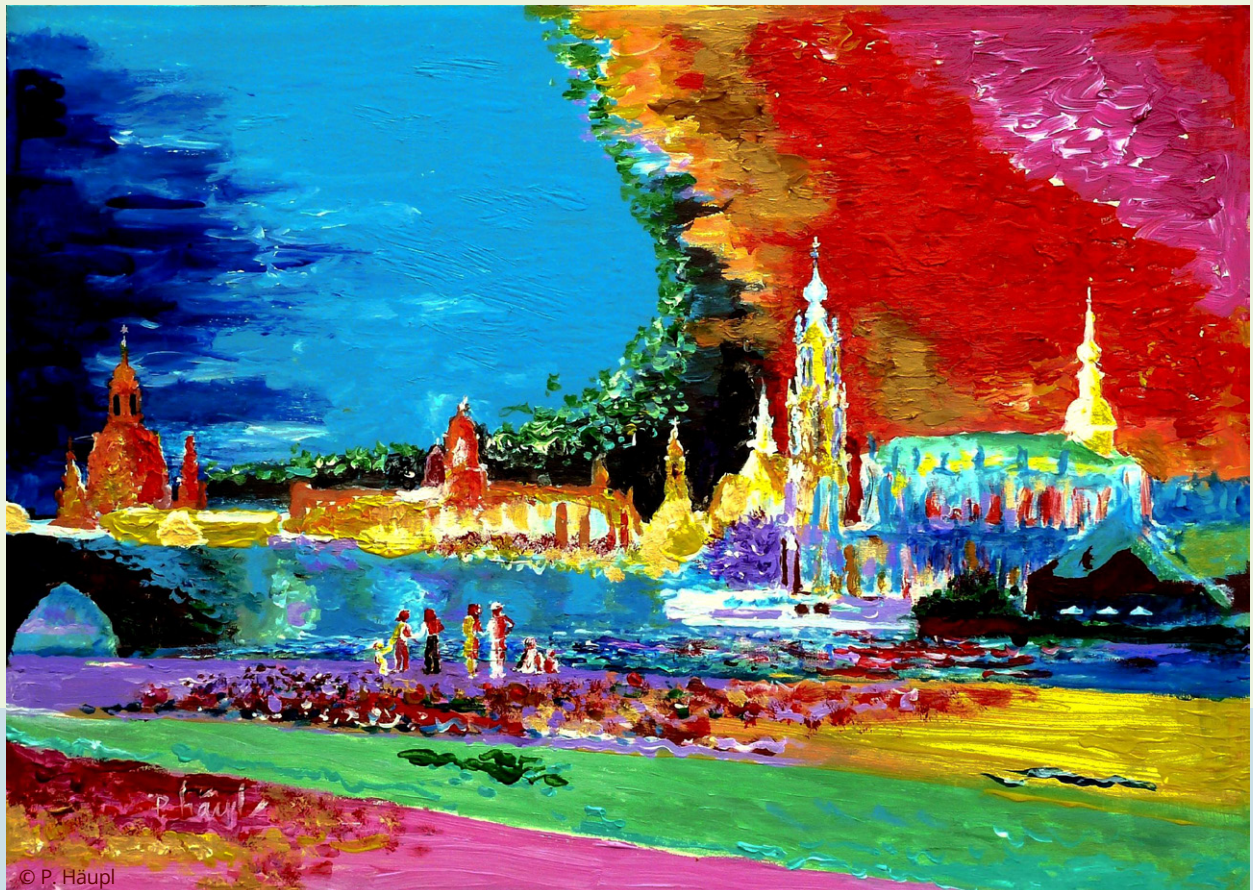
PROCEEDINGS

CESBP  2016

BauSIM
2016

CENTRAL EUROPEAN SYMPOSIUM ON BUILDING PHYSICS 2016 / BauSIM 2016

September 14–16, 2016
DRESDEN, GERMANY



© P. Häupl

Editor

Fraunhofer IRB  Verlag

 TECHNISCHE
UNIVERSITÄT
DRESDEN

J. Grunewald

PROCEEDINGS OF THE

**CESBP Central European
Symposium on Building Physics**

AND

BauSIM 2016

September 14 - 16, 2016
Dresden, Germany

IMPRINT

Editor:
Technische Universität Dresden
John Grunewald
Zentrum für Bauforschung – Institut für Bauklimatik
Zellescher Weg 17
D-01062 Dresden

Phone +49 351 463 35259
Fax +49 351 463 32627
URL <https://tu-dresden.de/bu/architektur/ibk>

Bibliographic information published by Die Deutsche Nationalbibliothek

Die Deutsche Nationalbibliothek lists this publication in the Deutsche Nationalbibliografie; detailed bibliographic data is available in the Internet at www.dnb.de.

ISBN (E-Book): 978-3-8167-9798-2

Copy-editing: Anita Morandell Meißner
Producer: Fraunhofer IRB Verlag
Cover design: K.I.T. Group GmbH Dresden

All rights reserved.

No part of this publication may be translated, reproduced, stored in a retrieval system or transmitted in any form or by any means, electronic, mechanical including photocopying, recording, fax or otherwise, without the written permission of the publisher.

Many of the designations used by manufacturers and sellers to distinguish their products are claimed as trademarks. The quotation of those designations in whatever way does not imply the conclusion that the use of those designations is legal without the consent of the owner of the trademark.

The publisher provides no guarantee for the accuracy, completeness, and currency of any laws, regulations or guidelines directly or indirectly invoked or quoted in this book. Should readers require any information for their own purposes, direct consultation of the full, current edition of the relevant laws, regulations or guidelines is recommended.

© by Fraunhofer IRB Verlag, 2016

Fraunhofer Information-Centre for Regional Planning and Building Construction IRB
P.O. Box 80 04 69, D-70504 Stuttgart
Nobelstrasse 12, D-70569 Stuttgart

Phone +49 711 970-2500
Fax +49 711 970-2508
E-Mail irb@irb.fraunhofer.de
URL www.baufachinformation.de

TABLE OF CONTENTS

IMPRINT	II
PREFACE	IX
COMMITTEES	XI
PLENARY LECTURES	1
A-02: Plenary Session	
A-02-3 AixLib – An open-source Modelica library within the IEA-EBC Annex 60 framework	3
A-03: Plenary Session	
A-03-1 Energy ⁺ -settlements and -quarters – definition, planning, operation, monitoring and certification	11
A-03-3 Making the performance gap smaller and predictable	19
CONFERENCE PAPERS	21
B-01: Building Envelope Systems	
B-01-1 Design rules for floor heating system using new analytical formulas.....	23
B-01-2 Exploring flooding and rising water problems related to heritage; Case study St. Catherine’s Chapel, Lemiers, The Netherlands	29
B-01-3 Calculating pareto-optimal airtightness levels for residential buildings	37
B-02: Salt and Frost Damage	
B-02-1 Salt Damage of the stone Buddha carved into the cliff.....	45
B-02-2 Comparison of frost damage indexes for two different weather years in the Czech Republic.....	53
B-02-3 Effect of salts and absorption cycles in the capillary coefficient of building materials with different joints.....	61
B-03: Building Envelope Systems	
B-03-1 A thermal conductivity prediction model for porous building blocks	67
B-03-2 Results of Belgian quality control framework for cavity wall insulation.....	75
B-03-3 Sensitivity analysis of hygrothermal performance of highly insulated wall assemblies	83
B-04: Degradation and Damage Processes	
B-04-1 Degradation of the wall paintings of Hagia Sophia in Istanbul	91
B-04-2 Prediction of wood decay progress with natural infection under fluctuated temperature within building envelopes.....	99
B-04-3 Modeling damage of building materials induced by sodium sulfate crystallization.	105
B-05: Building Material Properties	
B-05-1 Modelling of water vapour sorption in silicate-based building materials	111
B-05-2 Experimental investigation of capillary absorption along mortar-brick interface plane	117
B-05-3 Impact of gypsum pore clogging on moisture transfer properties of bricks.....	125
B-06: Urban Physics	
B-06-1 Development of hygrothermal reference years for Germany.....	133
B-06-2 Influences of wind-driven rain and radiation on urban microclimate	141
B-06-3 Local climate models for hygrothermal building component simulations	149

B-07: Building Envelope Systems	
B-07-1	Investigation of leakage moisture in walls with wood fibre insulation157
B-07-2	Numerical modeling of coupled hygrothermal phenomena and frost-induced strains in moist building materials.....165
B-07-3	Cavity ventilation behind brick veneer cladding: experimental and numerical investigation.....171
B-08: Building Envelope Systems	
B-08-1	A mathematical model for hysteresis of sorption isotherm of salt-laden porous materials.....179
C-01: Integral Energy Concepts for Buildings and Neighborhoods	
C-01-1	Optimising buildings based on renewable primary energy183
C-01-2	Energy performance and lifecycle cost optimization of a local smart heating and electricity grid191
C-01-3	Hygrothermal behaviour of prefabricated wood frame façade elements for building renovation197
C-02: Integral Energy Concepts for Buildings and Neighborhoods	
C-02-1	Houses as thermal batteries for the electric grid?205
C-02-2	Durability of thermal renderings: Durability assessment procedures213
C-02-3	Turbine-House: patented energy plus innovation221
C-03: Integral Energy Concepts for Buildings and Neighborhoods	
C-03-1	Non-residential buildings: Input parameters for modeling the energy demand227
C-03-2	Database development with “3D-CityGML”- and “EnergyADE”- schema for city-district-simulation modelling235
C-03-3	Density-based clustering algorithm for fault detection and identification in HVAC systems.....243
C-04: Energetisches Gebäudemonitoring & Betriebsoptimierung	
C-04-1	Analysen eines zellulären, regionalen Energiesystems in Theorie und Praxis.....251
C-04-2	Monitoring Based Commissioning (MBCx) in energy and facility management.....259
C-04-3	Monitoring und Bilanzrechnung: Ganz ohne Performance Gap267
C-05: Building Envelope Systems	
C-05-1	Effects of water repellent on frost damage in outer walls of rock-hewn churches in Cappadocia, Turkey277
C-05-2	Selecting moisture reference year for hygrothermal simulations.....285
C-05-3	Study on environmental performance evaluation method on advanced façade system293
C-06: Building Material Properties	
C-06-1	Numerical estimation of isothermal moisture storage and transport properties301
C-06-2	Numerical simulation of drying process in building materials309
C-06-3	Two-scale model of masonry on parallel computers315
C-07: Integral Energy Concepts for Buildings and Neighborhoods	
C-07-1	Modeling low temperature district heating networks for the utilization of local energy potentials.....323
C-07-2	Urban energy modeling using Multivariate Cluster Analysis329
C-07-3	Feasibility study of a multilevel district heating grid with dissolved supply and return using Modelica.....337
C-08: Human Comfort, Health and Indoor Air Quality	
C-08-1	Human decision making in energy-relevant interaction with buildings.....345
C-08-2	Promotion of natural ventilation during summer in a traditional Japanese dwelling with a small courtyard.....353

D-01: Modelling and Simulation Analysis of Buildings	
D-01-1	Generation of building geometry for energy performance simulation using Modelica361
D-01-2	Stochastic analysis for design space exploration and building performance optimisation369
D-01-3	Combination of Monte-Carlo approach and artificial neural network for the determination of Swiss typical building thermal load profiles.....377
D-02: Interoperability, Building Information Modelling (BIM)	
D-02-1	Model view definition for advanced building energy performance simulation383
D-02-2	eeBIM Lab – Towards a coherent green building design process.....391
D-02-3	Hysteresis of liquid moisture transport in porous building materials: experimental and computational analysis.....397
D-03: Modellierung und Simulation im Lebenszyklus von Gebäuden	
D-03-1	Modellprädiktive Einzelraumregelung auf Basis empirischer Modelle.....405
D-03-2	State space models as a common tool for control design, optimization and fault detection in building systems.....413
D-03-3	Dezentrale Einspeisung von solaren Wärmeerträgen in Nah- oder Fernwärmenetze – Ergebnisse einer Simulationsstudie421
D-04: Building Envelope Systems	
D-04-1	Exploring the implications of variance in urban microclimate for buildings’ energy performance: a simulation based approach429
D-04-2	The performance of vacuum glazing in existing window constructions: A case study.....435
D-04-3	Numerische Simulation am Praxisbeispiel der Hygrothermie von Holzbalkenköpfen441
D-05: Gebäude – Anlage – Mensch	
D-05-1	Fertigteile zur multifunktionalen thermischen Nutzung449
D-05-2	Numerische und experimentelle Untersuchung thermisch aktivierter Sandwichwände mit integriertem Paraffin.....457
D-05-3	Qualitative und quantitative tageslichttechnische Fassadenplanung für die Beratungspraxis465
D-06: Gebäude – Anlage – Mensch	
D-06-1	BuildingSystems - Eine modular hierarchische Modellbibliothek zur energetischen Gebäude- und Anlagensimulation.....473
D-06-2	Coupling a thermal comfort model with building simulation for user comfort and energy efficiency481
D-06-3	Exploring the effectiveness of window operation models for thermal comfort and energy performance assessments489
D-07: Gebäude – Anlage – Mensch	
D-07-1	Simulation und experimentelle Evaluierung thermoaktiver Textilien für die energieeffiziente Heizung und Kühlung von Räumen497
D-07-2	Betonkernaktivierung mit Luft im Vergleich zu etablierten Systemen der Raumkühlung505
D-07-3	Agentenbasierte Steuerung von thermischer Simulation in Echtzeit513
D-08: Algorithms for Computer-aided Decision Making	
D-08-1	Calibration of building energy use models: A case study of three residential buildings in Kosovo.....521
D-08-2	Numerical calculation of direct sound transmission using a combined finite element – statistical energy analysis approach527
E-01: Datenflussketten, Kopplung von Simulationsprogrammen	
E-01-1	Scalable design-driven parameterization of reduced order models using archetype buildings with TEASER535
E-01-2	Coupling building morphology optimization and energy efficiency – a proof of concept543
E-01-3	Erweiterung von Modellen zur Anwendung strukturvariabler Simulationen in Modelica551

E-02: Datenflusketten, Kopplung von Simulationsprogrammen	
E-02-1	Automated collocation of simulation modules in FMI-based Building Energy Co-Simulation.....559
E-02-2	Consideration of heating elements' behaviour in a co-simulation setting using model-predictive controls.....565
E-02-3	Schnittstellen für die Co-Simulationskopplung zwischen Gebäude- und Heizungsanlagensimulation573
E-03: Datenflusketten, Kopplung von Simulationsprogrammen	
E-03-1	Entwicklung von Algorithmen zur Simulatorkopplung unter Verwendung der FMI-Schnittstelle für Anwendungen in der Gebäudesimulation.....581
E-03-2	Integration von thermischer Gebäudesimulation und Strömungssimulation in einer Nutzeroberfläche - BIM HVACTool589
E-03-3	Instationäre energetische Bewertung von Wärmepumpen- und Mikro-KWK-Systemen – Simulation und Emulation597
E-04: Validierungsszenarien, Qualitätssicherung	
E-04-1	Simulation and validation of thermal air stratification in living spaces.....605
E-04-2	An inquiry into the reliability of urban-level CFD-based air flow field analysis.....613
E-04-3	Prüfung und Konvertierung von TGA ifcXML-Modellen zu SimModel621
E-05: Numerische Lösungsverfahren, Optimierung und Implementierung	
E-05-1	Ansätze zur Parallelisierung numerischer Lösungsverfahren in der Bauteilsimulation.....629
E-05-2	Vergleichende Betrachtung numerischer und messtechnischer Untersuchungen ausgewählter Referenzexperimente für die Heizungs- und Raumluftechnik637
E-05-3	Transformation der Gebäudeenergiesimulation NANDRAD mit variablem Zeitschrittlöser in eine FMU für Co-Simulation645
E-06: Numerische Lösungsverfahren, Optimierung und Implementierung	
E-06-1	Modellierung oberflächennaher Erdwärmeübertrager für Systemsimulationen in TRNSYS653
E-06-2	Adiabatic absorber model for the liquid desiccant distribution network at the technology park Berlin Adlershof using Modelica.....661
E-06-3	Analysis of cooling and heating energy provided by a green roof system with integrated air ducts for mid-latitude cities669
E-07: Wissenstransfer für die Simulationspraxis / Ausgewählte Praxisbeispiele	
E-07-1	Comparison of pipe network designs by CFD-simulations.....677
E-07-2	Application of calibrated CFD models for the assessment of a displacement ventilation system683
E-07-3	Softwaregestützte Wärmebedarfsermittlung bei Informations- und Ressourcenknappheit691
E-08: Gebäude – Anlage – Mensch	
E-08-1	Auswirkungen der Gebäudebegrünung auf das hygrothermische Verhalten der Gebäude und deren Umgebung.....697
E-08-2	Ganzheitliche energetische Modellierung von Privathaushalten unter Berücksichtigung von Gebäudestruktur und Nutzerverhalten705
POSTERS..... 713	
P-01-1	Exploring the effectiveness of building performance codes: A lighting standard case study.....715
P-01-2	Monolithic versus multilayered stone walls: capillary absorption723
P-01-3	Determination of moisture transport coefficients for cement mortar and cellular concrete in case of non-linear models of diffusion.....731
P-01-4	Experimental and theoretical analysis of water vapour accumulation in porous building materials.....739
P-01-5	Analytical model of transportation of saline solutions during drying745

P-02-1	Accounting for the temperature dependence in the sorption isotherms in the prediction of hygrothermal behavior of hemp concrete	751
P-02-2	An improvement of the airflow in the floor convector	759
P-02-3	From materials properties to modeling hygrothermal transfers of highly hygroscopic walls	767
P-02-4	The analysis of facing wall construction date on its humidity condition	775
P-02-5	Floating settlements – A new research area in the building physics	781
P-03-1	Development of a thermal building model for heat and electricity supply optimization in city quarters.....	787
P-03-2	Bestimmung, Bewertung und Reduktion von Wärmeverteilverlusten in Wohngebäuden.....	795
P-03-3	Global Dynamic Sensitivity Analysis using Functional Transformation for Energy Simulation of Residential Quarters	803
P-03-4	FMI-Kopplung von EnergyPlus mit MATLAB zur Abbildung von Interaktionen im Distrikt-Modell EmMi-transient	811
P-03-5	Modellbildung für thermische Arealvernetzung mit IDA-ICE	819
P-04-1	Simulation für Planungs-/Betrieboptimierung von Kreislaufverbund-Wärmerückgewinnungssystemen.....	827
P-04-2	Influence of control strategy on the performance of floor heating systems in unsteady state operation	835
P-04-3	LEXU II - Einsatz von außenliegender Wandtemperierung bei der Gebäudesanierung	843
P-05-1	Bedarfsberechnung vs. Simulation und Verbrauchsmessung am Beispiel einer Passivhaus-Sporthalle	851
P-05-2	Gesamtenergetische Gebäudeoptimierung im Spannungsfeld zwischen gesetzlichen Vorgaben und Praxis.....	859
P-05-4	An ontology-based tool for automated configuration and deployment of technical building management services	865

AUTHOR INDEX 873

PREFACE

DEAR PARTICIPANTS AND GUESTS OF CESBP AND BAUSIM 2016!

We are delighted to welcome you in Dresden at the joint-conference of CESBP and BauSIM. During the three days, researchers and experts will share and discuss their experiences and project results on different topics of building physics as well as of building and plant simulation. The large number of submitted papers on various topics finally selected by the scientific committee reflects the variety and complexity of specific research questions concerning building physics, buildings and systems. As shown in the official program, a large part is dedicated to those contributions in the field of simulation applications focused on lifecycle aspects of buildings, district balancing, as well as the interaction of Building – System – Human. Two full days of presentations on dataflow and numerical procedures are offering a sufficient number of topics for all fans of simulation techniques open for hopefully interesting and inspiring discussions with colleagues.

We hope that the event may provide an appropriate framework for the successful exchange of information and the permanent professional networking, so that you keep your stay in Dresden in good memory.

LIEBE TEILNEHMENDE UND GÄSTE VON CESBP UND BAUSIM 2016!

Wir freuen uns sehr, Sie hier in Dresden zu der gemeinsamen Konferenz von CESBP und BauSIM begrüßen zu dürfen. In den drei Veranstaltungstagen werden Forscher und Fachexperten ihre Erfahrungen und Projektergebnisse zu unterschiedlichsten Themen aus der Bauphysik sowie der Gebäude- und Anlagensimulation teilen und zur Diskussion stellen. Die große Zahl der eingereichten und durch die wissenschaftlichen Komitees für das Programm ausgewählten Beiträge zu den Themenschwerpunkten ist Ausdruck der Vielfalt und Komplexität konkreter bauphysikalischer, gebäude- und anlagentechnischer Forschungsfragen. Wie aus dem Programm ersichtlich, nehmen im Bereich der Simulationsanwendungen Beiträge zu den Lebenszyklusbetrachtungen von Gebäuden, der Quartiersbilanzierung, sowie der Interaktion von Gebäude-Anlage-Mensch einen großen Raum ein. Für die Freunde der Simulationstechniken bieten zwei volle Tage mit Referaten zu Datenflusketten und numerischen Lösungsverfahren auch ausreichend Stoff für hoffentlich interessante und anregende Gespräche mit Fachkolleginnen und -kollegen.

Wir wünschen uns, dass die Veranstaltung so einen geeigneten Rahmen für den erfolgreichen Informationsaustausch und die bleibende fachliche Vernetzungen bieten kann, so dass Sie Dresden in guter Erinnerung behalten.

Prof. Dr.-Ing. John Grunewald

Prof. Dr. Ing. Clemens Felsmann

COMMITTEES

INTERNATIONAL SCIENTIFIC COMMITTEE (CESBP)

John Grunewald (Dresden, Germany, chair)
Ardešhir Mahdavi (Vienna, Austria, vice-chair)
Dariusz Gawin (Łódź, Poland, vice-chair)
Robert Černý (Prague, Czech Republic, vice-chair)
Peter Matiasovsky (Bratislava, Slovakia, vice-chair)

Jesper Arfvidsson (Lund, Sweden)
Vasco Peixoto de Freitas (Porto, Portugal)
Stig Geving (Trondheim, Norway)
Carl-Eric Hagentoft (Gothenburg, Sweden)
Shuichi Hokoi (Kyoto, Japan)
Andreas H. Holm (Munich, Germany)
Hans Jansen (Leuven, Belgium)
Arnold Janssens (Ghent, Belgium)
Jan Kosny (Boston, USA)
Jaroslav Kruis (Prague, Czech Republic)
Bob Martens (Vienna, Austria)
Carsten Rode (Lyngby, Denmark)
Staf Roels (Leuven, Belgium)
Henk Schellen (Eindhoven, The Netherlands)
Matthias Schuß (Vienna, Austria)
Juha Vinha (Tampere, Finland)
Libor Vozar (Nitra, Slovakia)

SCIENTIFIC COMMITTEE (BAUSIM)

John Grunewald (Dresden, Germany)
Clemens Felsmann (Dresden, Germany)
Andreas Nicolai (Dresden, Germany)
Joachim Seifert (Dresden, Germany)
Martin Bauer (Augsburg, Germany)
Petra von Both (Karlsruhe, Germany)
Sebastian Herkel (Freiburg, Germany)
Werner Jensch (Munich, Germany)
Roland Koenigsdorff (Biberach, Germany)
Martin Kriegel (Berlin, Germany)
Hans-Peter Leimer (Hildesheim, Germany)
Anton Maas (Kassel, Germany)
Madjid Madjidi (Munich, Germany)
Dirk Müller (Aachen, Germany)
Christoph Nytsch-Geusen (Berlin, Germany)
Christian Schweigler (Munich, Germany)
Klaus Sedlbauer (Munich, Germany)
Volker Stockinger (Munich, Germany)
Christoph van Treeck (Aachen, Germany)
Andreas Wagner (Karlsruhe, Germany)

PLENARY LECTURES

AIXLIB – AN OPEN-SOURCE MODELICA LIBRARY WITHIN THE IEA-EBC ANNEX 60 FRAMEWORK

D. Müller¹, M. Lauster¹, A. Constantin¹, M. Fuchs¹, and P. Remmen¹

¹RWTH Aachen University, E.ON Energy Research Center, Institute for Energy Efficient Buildings and Indoor Climate, Germany

ABSTRACT

AixLib is a Modelica model library with focus on modeling the dynamic behavior of buildings, HVAC equipment and distribution networks to enable integrated analyses of energy systems on the scales from single building to city district. The library is available at www.github.com/RWTH-EBC/AixLib.

In this paper, we present the library and its integration within the IEA Annex 60. Possible applications are demonstrated using two use cases for the controls of a single building and for the heat demand of a city district. The paper concludes in a discussion of typical applications for AixLib and which developments we plan for the future.

INTRODUCTION

Modelica with its object-oriented and equation based approach is becoming a widely used modelling language for building performance simulation (BPS), as reflected by the IEA EBC Annex 60 project "New Computational Tools for Building Performance Simulation". Among other goals, this project aims at harmonizing the use of Modelica for BPS by means of the Annex 60 library, a common core library with basic functionalities. As explained by Wetter et al., 2015, this library is not meant to be used by end users directly, but to be merged into specialized model libraries that provide the user with additional models, further examples and documentation. Libraries using this approach and integrating the Annex 60 library include *Buildings* (Wetter et al., 2014), *BuildingSystems* (Nytsch-Geusen et al., 2013), *IDEAS* (Baetens et al., 2012) as well as *AixLib* (Fuchs et al., 2015). A major benefit of this approach is the increased collaboration on common base classes and increasing compatibility between these individual libraries. The open development of the Annex 60 library can be followed and contributed to at <https://github.com/iea-annex60/modelica-annex60>.

The main aim of AixLib is to provide a building performance library of Modelica models to enable integrated analyses of energy systems on the scales from single building to city district. In addition to the

models from the Annex 60 library core, AixLib consists of models for building physics, HVAC models and ready-to-use data sets. The range of building models includes a more detailed high order approach (Constantin et al., 2014) as well as a low order approach to reduce computing times for city district scale simulations (Lauster et al., 2014). AixLib follows an open-source approach and encourages third parties to take part in the development and application of the library. It is published using the open source Git repository hosting service GitHub. The library can be downloaded, cloned and forked at www.github.com/RWTH-EBC/AixLib.

In this paper, we present the library's structure and the basic concepts using Modelica. We show how the Annex 60 activities influence the design of AixLib and sketch the further steps of development for the library. Two examples illustrate the benefits of using Modelica and the application of simulation models for different scales. They show how the simulation's goal influences the modelling and which decisions have to be made when designing such models. The first use case focuses on a high order model of a single building with detailed HVAC system to analyze demand side management control strategies. The second use case combines multiple low order models and idealized HVAC to calculate heat demands of an entire city district. The paper concludes in a discussion of what typical applications for AixLib are and which developments we plan for the future. With this library, we contribute to the ongoing process towards harmonized open-source tools for powerful and interconnected BPS on various scales.

INTEGRATION WITH ANNEX 60 LIBRARY

The main goal of the Annex 60 library is to harmonize the work on building performance simulation model libraries in Modelica, which had suffered from fragmentation prior to the Annex 60 efforts. In addition to its function as a platform for collaborative development between different library development teams, one important focus of the

library with regard to this goal is to provide common base classes and basic functions for other libraries to use.

Especially the base class concept enabled by the object-oriented modeling approach of Modelica is a crucial factor for compatibility of models between different libraries for the end user. Prior to the Annex 60 development, e.g. different implementations for fluid connectors, media properties or energy balances would in many cases prevent using component models from different libraries to model a building energy system. In contrast, the Annex 60 library contains among other models two-port and four-port base classes that define standard connectors for fluid in- and outflow as well as energy balances. By merging these models into the respective target library, it can extend those base classes to model e.g. different HVAC components that, as a result, can then be connected to component models from other libraries using the Annex 60 base classes.

In addition, the collaborative development within the Annex 60 group allows for testing different model and function implementations and distributing the most efficient implementations into all participating libraries by means of merging the Annex 60 library into these target libraries.

With help of the Python package `BuildingsPy`, the Annex 60 library can be merged into other Modelica libraries automatically. This merging method fully integrates the package structure of the Annex 60 library into the target library's package structure. At the time of writing, in addition to a resources directory and experimental packages, the Annex 60 library contains the following main packages:

- Airflow
- Boundary Conditions
- Controls
- Fluid
- Media
- Types
- Utilities

In case the target library already contains a package of the same name at the same hierarchical level, both packages will be merged. If there is no corresponding package of the same name at the target library's corresponding level, the package will simply be copied into the target library.

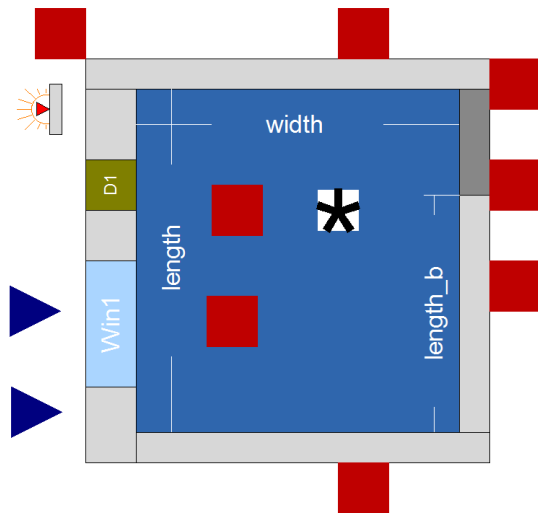


Figure 1: Scheme of a room model with thermal connectors (red squares) from HighOrder approach

Similar to other libraries using the Annex 60 library, AixLib not only integrates the Annex 60 library by this automatic merge, but also follows its design guidelines regarding model implementation, documentation and unit testing. More detail on how the integration of the Annex 60 library changed the structure of AixLib can be found in Fuchs et al., 2015. Furthermore, the Annex 60 library contains automated unit tests and reference results to check the library for side effects of changes and to verify its correct functioning. The unit tests are prepared by example models and `mos`-scripts that can then be automatically run in a test suite with the Python package `BuildingsPy`.

AIXLIB OVERVIEW

With the objective to model the dynamic behavior of buildings, HVAC equipment and distribution networks to enable integrated analyses of energy systems on the scales from single building to city district, AixLib contains model implementations with varying levels of detail. In many cases, analyses of a single building allow for (and may require) a more detailed modeling approach, while analyses of multiple buildings on a city district scale often rely on simplified models with a lesser level of detail. This concept applies to both the models for building physics and for HVAC components.

The AixLib adds three main packages to the Annex 60 library while integrating several sub-packages into the Annex 60 structure:

- Building
- DataBase
- HVAC

The models for building physics are collected in AixLib's Building package. The two modeling approaches with different levels of detail can be found in the sub-packages HighOrder and LowOrder, in reference to the order of states used to model the building envelope. While the HighOrder approach models all individual elements of the building envelope and their spatial context in high detail, the LowOrder approach uses a spatially aggregated model for thermal zones with less detail but also higher calculation speeds. Thus, the LowOrder model is a useful tool for analyses on district scale and fast parameter studies while the HighOrder model is designed for in-depth analyses of single buildings.

In addition, the HighOrder building model aims at facilitating case studies on different setups of typical building properties by means of user-friendly parametrization and pre-defined datasets. Currently, such datasets included in AixLib represent building envelope properties based on German energy saving ordinances from different years for light-weight, medium, and heavy building types. These datasets can not only be directly used by an end-user, they can also be used as a template to add own datasets according to own requirements. The model propagates these property datasets through the whole bottom-up approach in which wall elements (with optional window and door parts) are combined to room models which in turn are used to assemble building models. Fig. 1 shows the scheme of such a room model. As a result, the properties of the entire building with all its components can be varied at the top level, so that parameter studies can easily be performed once the model has been assembled. More information on the HighOrder building model can be found in Constantin et al., 2014.

In contrast to the high spatial resolution of the HighOrder approach, the LowOrder approach (Lauster et al., 2014) aggregates all wall elements of the same type (adiabatic interior walls and diabatic exterior walls) into one representative wall type element (Figure 2). Each element is represented by a resistance-capacitance model. The model is based on the VDI Guideline 6007 (German Association of Engineers, 2012), from which the methods for aggregation and calculation of the resistance and capacitance values are adapted. Lauster et al., 2013 give more details on the differences with the also widely used model specified in ISO 13790. With its fast simulation times, the LowOrder model has been shown to perform well for analyses of multiple buildings in an urban context (Lauster et al., 2014).

Through Modelica thermal connectors, both of these building models can be connected to models of HVAC systems to form an integrated model of the building energy system. To this end, AixLib contains

different models for components of heating and cooling systems as well as for ventilation and air conditioning components.

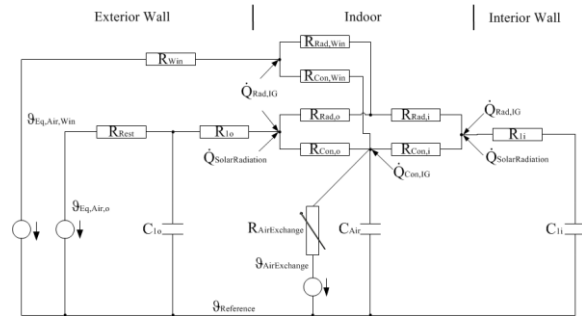


Figure 2: Thermal network of LowOrder model

As the Annex 60 library also contains a growing number of such component models, the user can in some cases freely choose between the AixLib and the Annex 60 implementation for a certain component. Because of the shared base classes, these models are often interchangeable, though they offer a different level of detail or modeling approach in most cases.

As the background of AixLib's development stems from German research project, the component models have a stronger focus on water-based heating systems than on cooling systems. Examples for basic component models included in the library are heat generation equipment like heat pumps, solar thermal collectors or gas boilers as well as components for the distribution and transmission of heat like pumps, pipes, valves and radiators.

For ventilation and air handling, the library similarly includes model for fans and ducts as well as models for air handling units, humidifiers and de-humidifiers. Especially the air handling unit model is designed to also work with the LowOrder building model, so that for city districts with a non-residential building stock (e.g. a research campus) the energy demand for air conditioning can be estimated in addition to the buildings' heating and cooling demand as a time-dependent function of the outdoor conditions.

USE CASE: DEMAND SIDE MANAGEMENT FOR AN APARTMENT

The first use case deals with an apartment in a multi-family dwelling configured as a heavy building and using the thermal insulation regulation WSchV1984. The apartment consists of two bedrooms, a living room, a corridor, a bath and a kitchen with an overall net floor area of about 70 m² (Figure 3). The heating system consists of a generation system with a boiler and a delivery system with radiators equipped with thermostatic valves.

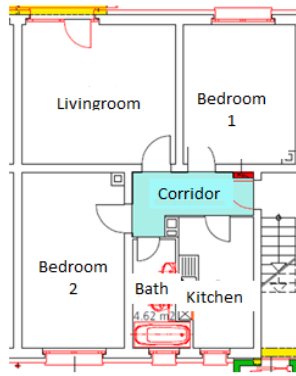


Figure 3: Floor plan of the investigated apartment

The intention of this use case is to investigate the possibilities of Demand Side Management (DSM) by overheating the apartment when it is empty. This allows storing heat within the walls and using this heat in times of high energy prices. The heat load is shifted from times of high energy prices to times of lower energy prices.

For this use case, we need to model the building physics as well as the hydraulic system in detail. The time constants within DSM concepts are within hours, thus all effects with similar time constants need to be considered. This includes a discretized modelling of thermal masses (primarily the walls) as well as of hydraulic circuits and radiators, boilers, etc. For that, we use the `HighOrder` building model with one wall model per actual wall and a layer-based discretization for each wall (each layer of a wall is modelled by two resistances and one capacitance) to model each room separately. Heat transfer through walls to adjacent rooms incorporated in this approach. The boundary conditions are defined for each room, which allows dedicated occupancy profiles per room. We combine the `HighOrder` model with detailed models for hydraulic components as pipes, valves, radiators, pumps and boiler all again representing one actual component in the “real” system and discretized in space if necessary (Figure 4).

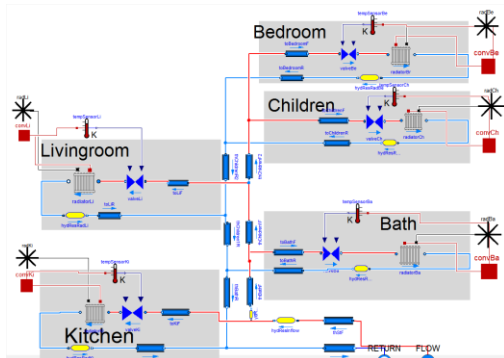


Figure 4: Hydraulic distribution system of investigated apartment

The following simple demand side scenario is simulated: two hours before the users return home after work, from 16:00 until 18:00 the house is pre-heated by setting a higher set temperature. Once the users arrive the temperature is set back. The usual set temperatures are 20°C during day time and 18°C during night time, from 22:00 to 6:00. A reference case, without DSM, uses only these set temperatures. During the short pre-heating period in the afternoon, energy will be stored in the buildings mass and given back to the room gradually over time.

Figure 5 shows the profiles for air temperature and the radiator power in the living room for both cases. For the DSM case the radiator power is lower throughout the day, around 14% less after the pre-heating, while at night there is no need for the thermostatic valve to open. Considering that period after 18:00 is considered peak time, with a flexible energy tariff cost reductions are achievable with such a strategy.

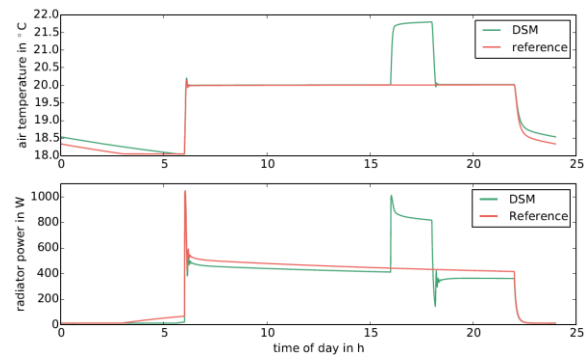


Figure 5: Simulation results for demand side management use case

USE CASE: HEAT DEMAND OF A CITY DISTRICT

Subject of this use case is a research campus with 200 buildings of different use (office and lab), year of construction and net floor area. All buildings are connected to a local heating grid. The aim is to predict heat loads for the years 2020 to 2050, considering a renovation rate of 1.7 % per year. Such predictions help to evaluate energy savings potential and design central heating systems that are not oversized in future scenarios.

To model such a complex city district, the AixLib provides the `LowOrder` building model that allows fast simulation times while focusing on predominant physical phenomena. Data acquisition is often elaborate on district scale, which leads to a sparse information density. A building model incorporating details of minor importance is hard to parameterize on such a basis and can hardly supply additional benefits considering the high uncertainties in data acquisition. In addition, the `LowOrder` model still

provides sufficient accuracy and successfully passes verification tests such as those according to VDI 6007 (German Association of Engineers, 2012) and ASHRAE 140 (ASHRAE, 2011) and shows good agreement with measurements done by Annex 58 (Strachan et al., 2015).

The `LowOrder` model comes with a dedicated workflow automation tool and parameterization algorithms in the programming language Python, called TEASER. This tool integrates the `LowOrder` model into high-level Urban Energy Modelling (UEM) tools at our institute as well as provides interfaces to information models such as CityGML as well as application programming interfaces (API). Similar to AixLib, TEASER will be released as an open-source project at www.github.com/RWTH-EBC/TEASER.

Using TEASER and AixLib, we set up one model per building with seven zones each (divided by the usage, e.g. office, laboratory, floor, etc.). Each building model is customized by its net floor area, year of construction, building height and building type. These properties influence the wall constructions, material properties, geometric dimensions and boundary conditions (internal gains). Internal gains and weather conditions are given in hourly time steps to allow dynamic investigations. The building models calculate indoor air temperatures and heat loads using several models from the HVAC part of AixLib, including a mode based Air Handling Unit (AHU) model and ideal heater and cooler models. With a workstation (12 cores, 2.9 GHz, 32 GB RAM, Dymola 2016 FD 01), the one-year simulations for all 200 buildings with an hourly output time step took less than 8 hours.

The investigated research campus operates extensive measurements what allows a detailed comparison of simulation results and measurement on campus scale. Figure 6 shows daily values of heat load for simulation and measurement for the entire building stock. The simulation shows good agreement with the measurement even in times of high variations. The trend, mean values and variances (based on hourly values) of both curves are similar with some overestimation of the heat loads in the simulation for summer times. This is mainly related to dehumidification in the AHU's to condition laboratory zones. The visual impression of high agreement is verified by a coefficient of determination of $R^2=0.91$.

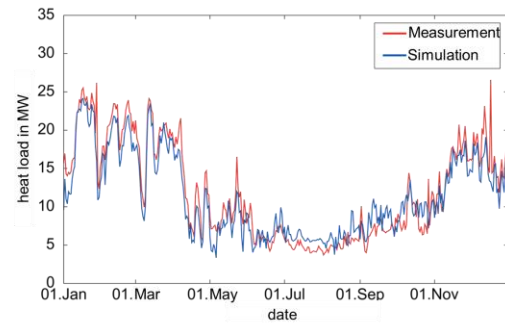


Figure 6: Comparison of simulation results and measurement

To predict heat loads in 2020 to 2050 with the given renovation rate, we used a functionality in TEASER to automatically retrofit buildings to a given renovation standard. Depending on the simulated year, a corresponding number of buildings are considered as retrofitted in the simulation. In this way, we determined heat load duration curves for pre-defined reference years (2020, 2030, 2040 and 2050). Figure 7 shows the annual load duration curves in hourly time steps as well as the energy savings within the decades. Comparing 2020 and 2050, 47% of heat demand could be saved with the given renovation rate. Even more important, the duration curves tend to flatten over the decades, leading to a higher relative share of base load. The shape of duration curves influences the dimensioning of heating systems as Combined Heat and Power units (CHP) that work efficiently and economic in base load without start-ups and shut-downs or part load operation.

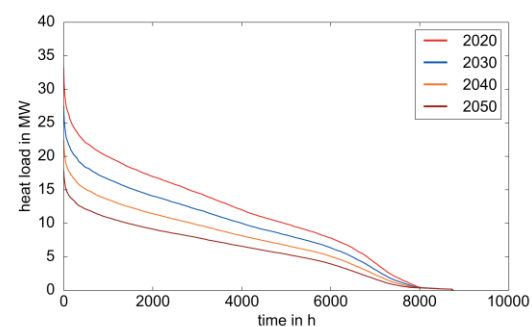


Figure 7: Annual load duration curves

CONCLUSIONS AND FURTHER APPLICATIONS

The presented use cases gave an overview of some of the capabilities and possible applications for AixLib as a model library for building performance simulation on scales from a single building to urban districts. While the first use case showed, how the

more detailed building model can be used to investigate control strategies like Demand Side Management in a building, the second use case demonstrated the applicability of AixLib's low order model for scenario analyses regarding the dynamic heat demand of a district.

In addition to the presented use cases, AixLib is continuously used in different research projects, resulting in new models and functionalities being added to the library. Currently, some key areas of development include improved methods to automatically generate models for urban energy systems, the addition of further component models, the modeling of exergy losses as well as the modeling and evaluation of new control strategies for building and district energy systems.

In combination with TEASER, we plan to further integrate our urban energy and building stock models into the Urban Energy Modelling research field and extend our approaches for statistic parameter estimation. This goes hand in hand with the activities within the Annex 60 regarding the development of adaptive `ReducedOrder` models with a flexible number of wall elements and variable spatial discretization of these wall elements. These new models will extend the existing `LowOrder` calculation core in AixLib and allow smooth variations of the model's order.

In addition to TEASER, further workflow automation tools for urban energy systems modeling are planned for upcoming open-source releases. This includes the Python packages `uesgraphs` and `uesmodels`. While `uesgraphs` aims at providing an open graph model framework to describe different network contexts within an urban energy system, `uesmodels` contains methods to automatically create Modelica models for district heating and cooling networks based on AixLib components. In combination with building models from TEASER output, this approach allows for creating dynamic system models of urban energy systems with significantly reduced manual effort.

Also, as presented by Stinner et al., 2015, we currently work on alternative implementations of thermal energy system models using a newly developed connector. These implementations focus on energy flows instead of mass flows and feature high user friendliness ("plug-and-play"). The aim is to use the same calculation cores for the actual energy system components while extending either standard fluid connectors in one variant or the developed plug-and-play connector in the other variant.

ACKNOWLEDGEMENT

We gratefully acknowledge the financial support by BMWi (German Federal Ministry of Economic

Affairs and Energy), promotional reference 03ET1177A.

This work emerged from the Annex 60 project, an international project conducted under the umbrella of the International Energy Agency (IEA) within the Energy in Buildings and Communities (EBC) Programme. Annex 60 will develop and demonstrate new generation computational tools for building and community energy systems based on Modelica, Functional Mockup Interface and BIM standards.

REFERENCES

- ASHRAE. 2011. Standard method of test for the evaluation of building energy analysis computer programs: ASHRAE Standard 140.
- Baetens, R., De Coninck, R., Van Roy, J., Verbruggen, B., Driesen, J., Helsen, L., and Saelens, D. 2012. Assessing electrical bottlenecks at feeder level for residential net zero-energy buildings by integrated system simulation. *Applied Energy*, 96:74–83.
- Constantin, A., Streblov, R., Müller, D. 2014. The modelica housemodels library: Presentation and evaluation of a room model with the ashrae standard 140. 10th International Modelica Conference, pp. 293–299.
- Fuchs, M., Constantin, A., Lauster, M., Remmen, P., Streblov, R., Müller, D., 2015. Structuring the Building Performance Modelica Library AixLib for Open Collaborative Development. Building Simulation 2015 Conference, Hyderabad, India.
- German Association of Engineers 2012. VDI guideline 6007-1: Calculation of transient thermal response of rooms and buildings - modelling of rooms. Beuth Verlag GmbH.
- Lauster, M., Constantin, A., Fuchs, M., Streblov, R., Müller, D. 2013. Comparison of two standard simplified thermal building models. Proceedings of CISBAT 2013: 4-6 September 2013, EPFL, Lausanne, Switzerland.
- Lauster, M., Teichmann, J., Fuchs, M., Streblov, R., Mueller, D. 2014. Low order thermal network models for dynamic simulations of buildings on city district scale. *Building and Environment*, 73:223–231.
- Nytsch-Geusen, C., Huber, J., Ljubijankic, M., and Rädler, J. 2013. Modelica BuildingSystems eine Modellbibliothek zur Simulation komplexer energietechnischer Gebäudesysteme. *Bauphysik*, 35(1):21–29.
- Stinner, S., Schumacher, M., Finkbeiner, K., Streblov, S., Müller, D. 2015. FastHVAC – A library for fast composition and simulation of

building energy systems. 11th International Modelica Conference, pp. 921–927.

Strachan, P., Hand, J., Svela, K., Heusler, I., Kersken, M.. 2015. A full-scale empirical validation study applied to thermal simulation programs. Building Simulation 2015 Conference, Hyderabad, India.

Wetter, M., Zuo, W., Nouidui, T. S., and Pang, X. 2014. Modelica Buildings library. Journal of Building Performance Simulation, 7(4):253–270.

Wetter, M., Fuchs, M., Grozman, P., Helsen, L., Jorissen, F., Lauster, M., Müller, D., Nytsch-Geussen, C., Picard, D., Sahlin, P., Thorade, M., 2015. IEA EBC Annex 60 Library – An International Collaboration to Develop a Free Open-Source Model Library for Buildings and Community Energy Systems. Building Simulation 2015 Conference, Hyderabad, India.

ENERGY⁺-SETTLEMENTS AND -QUARTERS - DEFINITION, PLANNING, OPERATION, MONITORING AND CERTIFICATION

Dr.-Ing. Volker Stockinger

Competence Center – Energy Efficient Buildings and Settlements, University of Applied Sciences Munich, Munich, Germany

ABSTRACT

The transition of the German energy-system (German: Energiewende) is a big challenge for both energy-efficient construction and the existing energetic infrastructure. Buildings change from “consumer” to “*prosumer*” (prosumer means consumer and producer at once). This results in new tasks for all social disciplines. To take into account this development, new findings and solutions for energy- and building-concepts for the future have been worked out on one of the first real built Plus-Energy Settlements in Germany. The extension of the observations from single buildings to settlements and districts plays an important role. Moreover the interdisciplinary research results show clearly that the transition of the German energy-system with technology alone is not feasible. The users play a crucial role and must at all times be taken into consideration.

INTRODUCTION

The energy-efficient construction of buildings in Germany since the 1970s has been a continuous development, which is reflected both in the tightening of legal requirements as well as new building standard definitions. The year 2002 was a milestone for energy-efficient construction in Germany and Europe. The building directive "Energy Performance of Buildings" (EPBD) of the European Union and the Council drew massive changes in the approach to buildings. The introduction of the German Energy Saving Ordinance (EnEV 2002), which was called for in the EPBD from 2002, represented an important step towards the holistic view of buildings. Until then, the building and the technique for providing the necessary heat supply were seen separately. Due to EnEV, the interaction of construction and the energy-system; energy efficiency was placed in the focus for the first time.

In the current version of the EPBD of July 08, 2010, the mandatory requirement for “nearly zero energy buildings” (NZEB) for all new buildings from January 01, 2021 was firmly anchored. The European Union determined that the buildings must have a very high energy performance and nearly zero energy needs which are covered if possible exclusively from renewable energy sources and best locally. The demand for the NZEB is the next logical step. While the combination of buildings and technical equipment was completed by the first version of the EPBD, the holistic view of building- and supply-concept are addressed in the current EPBD. This includes on the consumer side, in addition to the energy use for heat supply, all electrical needs. Moreover, in addition to reducing the energy demand by passive measures is also the self-supply with the on-site recovered renewable energy.

The next logical step is to increase the overall energy efficiency with the use of synergies in the combine of buildings in settlements and districts. For example, shifts of production- and consumption-peaks can be done locally. In this way, the energy use and production behaviors are "smoothed" and the surrounding supply structure relieved by the reduction or even complete avoidance of feed- or demand-peaks.

The building sector took an elementary change with the introduction of energy-efficient construction. Now, the energy-efficient construction of buildings is itself at a crossroads of major changes .

MOTIVATION

“Securing a reliable, economically viable and environmentally sound energy supply is one of the great challenges of the 21st century.” (BMWi 2010) In order to create the desired "Energiewende" in Germany until 2050, the “Energy Concept for an

Environmentally Sound, Reliable and Affordable Energy Supply" was launched in 2010. (BMWi 2010)

The building sector is an important part of the "Energy Transition" because buildings are responsible for nearly 40 percent of the whole of energy consumption. (EPBD 2010) The demand for the NZEB poses additional challenges for the building sector .

Currently, the view of building focuses mainly on the thermal energy demand. Exploiting the passive ways of reducing energy consumption (passive house) making new paths necessary to improve the energy performance of buildings. There is active power generation equipment for use, provided by available locally renewable energy sources, electrical and thermal energy. The self-generation requires a whole new way of looking at energy supply concepts for buildings. Why reduce the energy demand with passive measures to the extreme when enough renewable energy for self-supply are at the location? Rather, it is useful to coordinate the active and passive measures with each other to strive for the energetic optimum over the entire life cycle. In addition, the sinking thermal energy demand and the requirement for a very high overall energy efficiency of buildings engages the electrical energy demand for the operation of the building in the focus. A separate analysis of electrical and thermal energy will no longer be effective in the future.

The change of buildings away from the "pure consumer" to the "prosumer" both internally and externally, predicts an exciting future for the energy-efficient construction. The goal seems dictated by the statutory provisions. But the road is varied due to the new technical possibilities. The model homes from (Voss et al 2011, Fisch et al 2012, Hegger 2013) demonstrate that it is technically possible to construct buildings that in the course of a year produce more energy than they consume. This development has not yet arrived in the everyday construction process and makes the viewing of buildings in connection with the entire infrastructure necessary. The surpluses represent for the supply networks an additional challenge, since these are not designed for the decentralized supply of variable energy flows from renewable energy sources. For this purpose, efficient facility and building concepts act as a "battery" and ensure the balance between production and

consumption peaks. (Synwoldt 2013, Taphorn 2013, Herkel et al 2014) Settlement- and district-concepts for this case are of particular importance. (Erhorn-Kluttig et al 2011)

Another important aspect is the involvement of the user in the energy contemplation of buildings . The better the energy standard of a building, the more important is the user behavior. (Richter et al 2003) The building and the technical equipment therein can achieve ambitious energy targets only if the user accepts a certain amount of "heteronomy" by used measurement and control technology (German: Mess-, Steuer- und Regelungstechnik (MSR)) and the engineering systems are understood and used in the right way. However, this is only possible if the user is aware of his own behavior. Therefore the use of information and communication tools is an almost indispensable element of modern buildings.

The planning, construction and the energy-efficient operation of settlements and neighborhoods is in increasingly higher needs for all involved in construction. Width-ready planning and valuating tools are currently not able to take into consideration all relevant factors for future buildings. However, this will be necessary to allow for the planning reliable forecasts about the energy behaviour in the use phase. (Van Treeck et al 2014) The comparison of targeted values with the measured energy consumption figures provides important options for the future. For this purpose, in addition to the development of appropriate calculation tools a method is required that enables entire and adequate accounting of settlements and districts throughout the whole life cycle. To ensure energy-efficient operation of the technical equipment in use, operation optimization plays an important role. (Plesser et al 2010)

GOALS

The current changes in the environment and the new challenges for energy-efficient construction make completely new approaches in the development of sustainable energy supply concepts for buildings necessary . Therefore the following research question for the work presented asked:

What do energy supply concepts for settlements and districts of the future look like and what factors must be taken into consideration so that they are able to contribute to the "Energiewende" and thus to achieve

the objectives of the energy concept of the federal government?

The goal is to answer this question and to develop an independent standard definition in the general principles for energy supply concepts of settlements and districts. Here all the current building standard definitions and the European Union (EU) requirements for the NZEB standard are respected and these increases the view from the individual building to settlements and districts.

In order to support the multiplication of modern supply concepts for settlements and districts, we need solutions that allow the prompt implementation in practice. The development of such implementation approaches represents a fundamental objective of this work. In addition to the planning process, the subsequent operation and possibilities to optimize the energy result will also be addressed.

The potential of the electrical and thermal self-generation and the various uses of the provided energy make a completely new way of looking at future supply concepts necessary. Which energy flows must be given special consideration and the context in which they relate to each other were also developed as the impact of the changed conditions on the overall energy system of the settlements and districts.

The better the energy standard of buildings, the greater the influence of the user on the energy result. (Richter et al 2003) For this reason, special attention should be paid to the user awareness.

With current accounting methods, it is impossible to evaluate supply concepts for settlements and districts. The comparison of planning and measurements is currently neither possible nor planned. Self generated energy can be credited only to the extent of its own energy needs. The achievement of a valuate energy surplus is not envisaged in the EnEV. However, all these points are necessary to accounting settlements and districts in terms of energy comprehensively. To account for the above-mentioned aspects in this work, an accounting procedure was developed which makes a comparison of the calculated values and measurements of settlements and districts possible. They take place almost entirely in accordance with established procedures, but surpass the quality of previous processes in their combination. Electrical

and thermal energy supply systems should also be given attention, such as the ability to achieve a accounting energy surplus. Another objective is the comparison of implementation variants.

RESULTS

The results of the presented work were derived largely from the knowledge gained from the research project "Plusenergiesiedlung Ludmilla-Wohnpark in Landshut", which was one of the first Plus Energy Settlements created in Germany from 2009 to 2010 and scientifically studied from 2010 for four years.

The energy-efficient construction stands by the requirement of NZEB-standards is one of the biggest challenges. Buildings are currently primarily seen as a thermal energy consumer. The sinking thermal energy demands make it inevitable to consider the electrical energy needs in the future. Electric and thermal energy can no longer be considered separately. However not only the energy needs, but also the supply of energy from renewable sources pose challenges. Buildings converted from "consumer" to "prosumer" places new challenges on the surrounding energy infrastructure. The building can not be considered alone, but must in conjunction with the infrastructure. Thus, settlement and district concepts must get special definitions in the future, because they allow the use of the potentials in the energy network of producers and consumers and at the same time relieve the energy infrastructure.

The current development of energy-efficient building away from "consumer" to "prosumer" makes it necessary to adopt new approaches. To meet this process, the term "Energy[⊕]" was introduced and defined in this work. Energy[⊕] does not claim to be a new building standard! Rather Energy[⊕] aims to unite all current building standards and to link the relevant social and technical areas of building together. The view is extended from settlements and districts to single buildings. All electrical and thermal energy flows including their own generation and the necessary fuel use need attention. All supply systems that provide heat and/or electricity from renewable energy sources, with the exception of heating and power plants, are Energy[⊕] concepts. Here, Energy[⊕] is not limited to the construction of new residential buildings. The implementation of renovations and non-residential buildings as Energy[⊕] are possible and

recommended. The self-production enables completely new solutions for supply concepts. Alternatively or in addition to the pure thermal demand reduction through passive measures the efficiency of the overall system could be increased by active measures. For Energy⁺ there are no limitations in the choice of fuels used. Furthermore Energy⁺ demands do not go beyond the EnEV insulation standard. By integrating the embodied energy and electric mobility, buildings are more than energy consumers in everyday use. Importantly this is a first step in establishing a holistic approach and offers opportunities for the use of synergies.

There are various possibilities for implementing Energy⁺ supply concepts. Thus, the reduction of the heating energy demand by passive measures is important but not the only alternative for Energy⁺ supply concepts. Rather, the self-generation and exported surpluses allows a more diverse perspective. A higher energy need for the building operation and the associated savings in embodied energy can be useful if the necessary energy is covered from renewable sources themselves or they accounted by exported surpluses. The energy provision of heat and electricity makes the consideration of all relevant areas necessary. This includes the energy production as well as the heat-distribution and the use of storages beyond the required auxiliary energy. Factors like the location, the building physics and above all the user behaviour must be given attention. While the combined production of heat and electricity with co-generation heat and power generator (CHP) offers an interesting possibility, especially the hot drinking water (DHW) distribution network which needs special attention because of the high operating temperatures and the associated heat losses. Electrical and thermal energy storage systems become an important role in Energy⁺ supply concepts both from an energy and economic point of view. Supply and need, especially in the use of renewable energy sources, often do not match. Through the use of storages the shift of energy flows are possible and thus enables high own-use and own-coverage levels.

But only with the right operating characteristics, complex supply concepts reach their full efficiency. Therefore, optimizing operations represents an almost indispensable tool. The savings potential are enormous. This fact is underlined by the results from

the optimization operation on the district heating network of the Ludmilla-Wohnpark in Landshut (LWP) which reached energy savings of 20 percent for heat supply and 50 percent on auxiliary energy.

In Energy⁺ objects have various options to satisfy both need coverage and energy use. The coverage of energy demands may be completely or partly from its own generation. The technical realization of the energy demand coverage for the thermal and electrical energy can be very variable for different concepts. The same applies to the use of self-generated energy. It can be even used completely or partially or be used to account balance for the supply out of public supply networks. However, the self-use should always take precedence over the export. The highest possible own-use and own-coverage levels should be the aim to reduce the energy import to a minimum level. Storage have a positive influence on this.

Through the export of electric and thermal surpluses a accounting compensation of the energy supply is possible. The complete compensation of the electric energy needs is not required, but should be pursued under the existing technical and economic aspects.

User behavior has a enormous influence on the overall energy balance of settlements. But the energy behavior of people is as varied as the people themselves. The investigated metrics from the LWP clearly show, that deviations in the energy user behaviour of ± 100 percent and in extreme cases even +150 percent or more from the average value are possible. The influence of the user increases with the improvement of the building quality. In addition, as the influence of extreme energy consumers rises, the less flats the supply concept includes. Thus, a reliable prediction of the real energy consumption in the planning phase is not possible. In order to make statements under statistical probabilities on the energy demand, generic user classes must be developed. Energy-efficient buildings and systems can use their full potential only when they are used correctly. To facilitate a positive influence on user behavior, the basic understanding and the expectations as well as the attitudes of users towards energy efficient buildings have been developed by social science studies. Occupants of energy efficient buildings should be well aware of their influence on here own energy consumption. However this is

greatly underestimated. Potential is seen primarily in electric and less in thermal energy consumption. Comfort is more important than energy saving. The monetary aspects are the focus, less than the energy savings itself. This fact is especially for Energy[⊕] objects of special importance, because the own power supply significantly reduces the cost of energy purchases and additional money can be earned through the export of energy surpluses. Through energy-conscious behavior, saving of 5-25 percent is possible. To take full advantage of these savings, user awareness is of particular importance. It is possible to use different tools. Very important is the initial instruction of users on the existing building, supported by information events, user guides and manuals.

However, the influence of the behavior is only comprehensible to a user, if he understands the consequences of his behavior change. This is possible through the use of visualization tools such as the realized "online visualization of energy consumption" (O-ViVE) developed by the author as part of the research activity. O-ViVE allows not only the assessment of their own behavior but beyond to the comparison with the average of all users. By forming an average value for a settlement the data protection can be ensured. Furthermore it is possible to compare one's own consumption with a benchmark. By coloring after traffic light principle, the comprehensibility is guaranteed. The explorations out of the work studies show, depending on the user, that savings of 15-25 percent can be realized by consumption visualization with large-scale use.

Regarding the energy-efficient building itself, the building energy accounting and valuation is facing serious challenges. In the process, according to EnEV, only single buildings are addressed. Also achieving a negative energy balance is currently not possible. The accounting and valuation of settlement- and district-concepts with the aim of an energy-surplus is currently not feasible. The developed process for Energy[⊕] objects makes in three consecutive steps; the consideration of building operation, the comparison of energy consumption and energy output for the entire system. It is also possible to compare different implementation variants for Energy[⊕]-concepts by using the "Energy-Certificate[⊕] for Energy[⊕]-settlements and -districts" in the

planning and operation. In addition to the energy balance the electric own use and own coverage as well as the embodied energy will be considered for the overall system. More accounting options were examined on their current and future usefulness. One year has been set as the accounting period and as the system boundary the surrounding plot of the settlement or the district are defined. The assessment is carried out for both final and primary energy. "Energy[⊕] Efficiency Classes" and the "Efficiency House[⊕]" were introduced as well as the "Efficiency Class Diagram" to compare implementation variants. To guide the user to influence his positive behavior and to encourage the planners adopting realistic planning values, the comparison of planning- and measurement-values as a kind of "building-TÜV" must be obligatory. The users are encouraged to sustainable use. In this way rebound-effects will counteracted.

CONCLUSION

The findings in this study allow for the statement that Energy[⊕]-settlements and -districts can make a big contribution to the future energy supply in Germany and beyond. Beginning in 2021 all new buildings must meet the NZEB. Therefore, the implementation of new construction projects such as Energy[⊕] concepts must already be the declared goal.

However, the overall energy situation in Germany and Europe should never be disregarded. Normally the produced electric surpluses are from solar radiation. The export is very uneven as a result of seasonal and daily fluctuations. Furthermore, the conformity of consumption and production is rarely identical.

Thus current conventional power plants are operated to regulate times with low energy supply out of renewable. Times when the renewable electricity significantly exceeds the current energy consumption also create problems. Currently, the surpluses are reduced among other countries by exporting to the networks of European neighbors. This is in the long run, however, no solution, especially in terms of future growth of renewable energy. Expanding the distribution and building of more storages will create the infrastructural opportunities to adjust the regenerative power to the power consumption. However, the users can play their part, by adapting

their energy demand for the supply of the renewable energy sources.

In areas where there are already high fluctuations in the network, the problem is enlarged by surpluses from Energy⁺-settlements and -districts. For this case Energy⁺ concepts offer a possible solution with the possibility of partial or even complete power self-sufficiency, through the use of storage and variable power generation systems such as CHP. Through the intelligent use of the available storages, the regenerative production peaks can be reduced or maybe completely prevented. Theoretically, a purchase from the public network would be possible at peak times. This could even be an economic model, because a negative price arises at peak times. Thus, it might be sensible not to operate their own power generation and instead utilize external energy. Furthermore, an agreement with the public network operator could be made that agrees to separate the settlement or the district from the mains in times of high demand. For this purpose, the settlement or district must be able to guarantee an autonomous energy supply for this time. Energy⁺-settlements and -districts could provide balancing energy as an energy storage, thus helping to equalize production and consumption peaks. A settlement or district alone can not fulfill this function. However, if in the future, all new and renovated buildings will implement the Energy⁺ concepts and the communication with each other is made possible (smart grid), this approach may be a fundamental part of the German energy transition. The cost of balancing production and consumption would be distributed on many shoulders in this way.

If Energy⁺ concepts are to represent the standard of technology for the supply of settlements and districts in the future, they must be technically mature, operate on the energetic optimum and be architecturally appealing. To be successful integrated planning must not only be an empty word, but a living reality. In addition to the technical and economic aspects, in particular the social aspects need to be considered. The energy transition can only be achieved if it is accepted and supported by the people.

ACKNOWLEDGEMENT

We thank the Federal Ministry for Economic Affairs and Energy and the Project Management Jülich for

the approval of the projects "+Eins" and "+EQ-Net" and the resulting trust placed and the anytime excellent technical and organizational support.

REFERENCES

- Directive 2002/91/EG of the European Parliament and of the Council of December 16, 2002 on the energy performance of buildings
- Directive 2010/31/EU of the European Parliament and of the Council of May 19, 2010 on the energy performance of buildings
- Erhorn-Kluttig, H. et al. 2011. Energetische Quartiersplanung – Methoden – Technologien – Praxisbeispiele. Fraunhofer IRB Verlag, Stuttgart, Germany.
- Federal Ministry of Economics and Technology (BMWi). 2010. Energy Concept for an Environmentally Sound, Reliable and Affordable Energy Supply. BMWi, Berlin Germany.
- Fisch, M.N.; Wilken, T.; Stähr, C. 2012. EnergiePLUS – Gebäude und Quartiere als erneuerbare Energiequellen. Fisch, 1. Auflage, Leonberg, Germany.
- Hegger, M. et al. 2013. Aktivhaus – Das Grundlagenwerk – Vom Passivhaus zum Energieplushaus. Callwey Verlag, Munich, Germany.
- Herkel, S. et al. 2014. Netzreaktive Gebäude im Kontext der Energiewende. In: Energieinnovationen in Neubau und Sanierung, EnOB-Symposium 2014. Essen, March 20-21, 2014. PtJ, Jülich, Germany. p. 93-98.
- Plesser, S., Fisch, M.N. 2010. Gebäude energieeffizient betreiben – Den Anspruch der Planung einlösen. BINE Informationsdienst, Karlsruhe, Germany.
- Richter, W. et al. 2003. Einfluss des Nutzerverhaltens auf den Energieverbrauch in Niedrigenergie- und Passivhäusern. Bauforschung für die Praxis, Band 63, Fraunhofer IRB Verlag, Stuttgart, Germany.
- Synwoldt, C. 2013. Netzentlastung durch Speicher und Photovoltaik. Vortrag im Rahmen der 1. Speichertagung Rheinland-Pfalz, IfaS, Birkenfeld, Germany, February 27-28, 2013.
- Taphorn, N. 2013. Solarstrom verheizen – Effiziente Nutzung von Solarstrom durch Batterie- und Wärmespeicher in der Quartierssiedlung Weinsberg. Vortrag im Rahmen der 1. Speichertagung Rheinland-Pfalz, IfaS, Birkenfeld, Germany, February 27-28, 2013.

Van Treeck, C. et al. 2014. EnOB-geförderte internationale Forschungsaktivitäten und Software-Tools. In: Energieinnovationen in Neubau und Sanierung, EnOB-Symposium 2014. Essen, March 20-21, 2014. PtJ, Jülich, Germany. p. 17-23.

Verordnung über energiesparenden Wärmeschutz und energiesparende Anlagentechnik bei Gebäuden (Energieeinsparverordnung – EnEV) vom 16. November 2001.

Voss, K.; Musall, E. 2011. Nullenergie Gebäude – Internationale Projekte zum klimaneutralen Wohnen und Arbeiten. Detail Verlag, 1. Auflage, Munich, Germany.

Zweite Verordnung zur Änderung der Energieeinsparverordnung vom 18. November 2013.

MAKING THE PERFORMANCE GAP SMALLER AND PREDICTABLE

S. Moosberger
EQUA Solutions AG, Zug, Switzerland

ABSTRACT

The effective energy consumption of buildings in operation often differs a lot from the predicted energy performance. This phenomenon is pervasive enough that it meanwhile has its proper name: the “Performance Gap”. The reasons for it are numerous and well known: Assumptions that do not correspond to reality, applied models that are not adequate or measurements that are not accurate enough. But this does in no way mean that overcoming the performance gap is not possible or not payable. The remaining challenge is rather not to further develop the available methods and tools, but to use the existing technologies adequately and to effect the necessary paradigm change from standard based to monitoring based energy performance certification. Cases from today’s practise show that – with payable effort – it is possible to create whole building models matching perfectly with measured reality. Nonessential details are simplified, but all essential dynamic interactions and states of the investigated systems are considered. Such cases are no singularities any more, but represent the mainstream in state of the art of building planning practice, that absolutely goes in the right direction.

CONFERENCE PAPERS

DESIGN RULES FOR FLOOR HEATING SYSTEM USING NEW ANALYTICAL FORMULAS

C-E. Hagentoft, P. Roots

Building Technology, Chalmers University of Technology, Gothenburg, Sweden

ABSTRACT

New analytic expressions have been developed to determine the thermal resistance between the heat pipes and the interior air. The expression accounts for the distance between the pipes, the depth and the surface resistance (including inner cladding). Comparisons with numerical calculations are presented. Combined with analytical expressions for the ground heat losses of buildings without floor heating (Hagentoft 1988, Claesson et. al. 1991), (ISO EN 13370), handy formulas for the performance can be presented.

INTRODUCTION

In recent years the demand of floor heating systems have increased in Sweden. This is caused by the fact that floor heating is potentially giving a good indoor comfort. Another reason for the increasing demand is that some of the suppliers of the systems claim that the systems are energy saving, although under the condition that the indoor air temperature is reduced.

A slab on grade with floor heating do give higher heat loss to the ground in comparison with a slab without floor heating. The reason for this is that the slab with floor heating has higher temperature and this increases the heat loss.

In earlier studies (Roots, Hagentoft,2000,2001,2002), a global performance factor has been introduced in order to calculate the fraction of heat released to the interior, the beneficial part. The performance factor gives the opportunity to evaluate how the energy use in a building is affected by a floor heating system. The global performance factor is based on the relationship between the thermal resistance above and below the heat source.

In the Swedish floor heating practice, it is quite common to use wooden flooring (parquet flooring) on top of the concrete, which together with the surface resistance gives a substantial total surface resistance.

When calculating the feed forward temperature in a floor heating system the heat flow density is required for the building. The EN-1264 standard is based on the fact that the released heat to the indoor air in a concrete slab on grade can only be calculated by simulating the foundation in a program that solve the general heat equation. In the simulation, it is also assumed that the extra heat loss to the soil beneath the slab is 10 %. In Sweden this is not accurate anymore for new buildings. The foundation insulation thickness is normally 0,3 m or more.

In this paper, an alternative analytic calculation method for the feed forward temperature in a floor heating system is presented. The method is based on that the thermal resistance between the heating pipe and the indoor air is constant. The result shows that there is a possible to use an analytic expression for the calculating of the feed forward temperature in a floor heating system in the stationary case. The case represents the average condition, which according to (Karlsson, 2010) is sufficient in order to control well-insulated buildings.

HEAT FLOW TO THE INTERIOR FROM THE PIPES

A slab on grade with floor heating has been numerically simulated with different numbers of heat pipes with same temperature, se Figure 1. The pipes are positioned in the middle of the concrete layer.

The calculations are done in accordance with ISO EN 13370. The simulations are done starting with one pipe to the left, at the edge beam, and adding more pipes to the right, with a given fix distance. The result in Figure 2 shows that the heat flow to the interior is increasing linearly with increasing number of heat pipes. It can be shown that same results is also approximately correct if the insulation was replaced with soil, i.e. corresponding to a concrete slab directly on the soil.

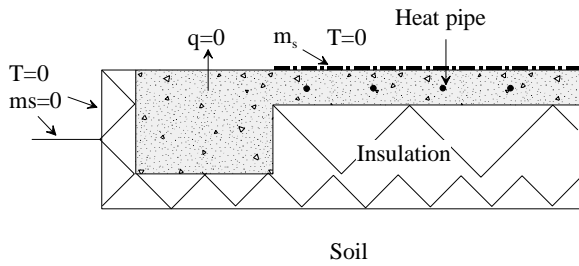


Figure 1. Slab on grade with floor heating and different numbers of heat pipes. The thermal surface resistance is m_s (m^2K/W) and the interior temperature is $0^\circ C$. At the edge, where the wall stands on the slab, the surface is adiabatic ($q=0$).

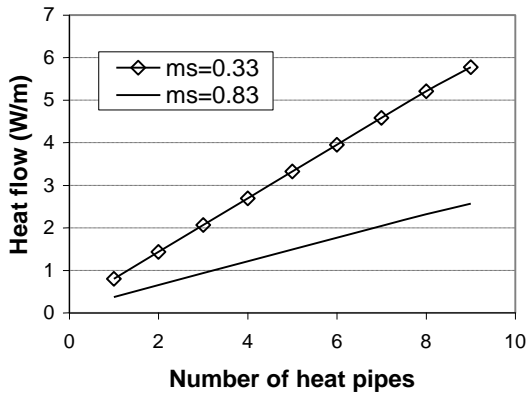


Figure 2. Total heat flow to the interior from the pipes. The surface thermal resistance between the slab surface and the interior is m_s (m^2K/W). The number of heat pipes is varying between 1 and 9.

Why do we have this behavior? Each new pipe seems to add the same amount of heat flow to the interior. The far most pipe to the left, at the edge beam, and the one far most to the right are exposed a bit differently to the surroundings, while the pipes in between face the same conditions. So when adding one more pipe we get a constant addition to the heat flow. Figure 3 shows the numerically calculated isotherms around the heat pipes, which are very similar for all pipes, except for those at the perimeters.

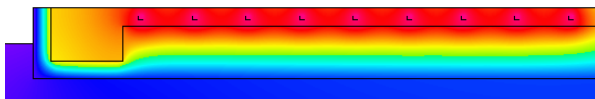


Figure 3. Simulated isotherms for the foundation presented in Figure 1.

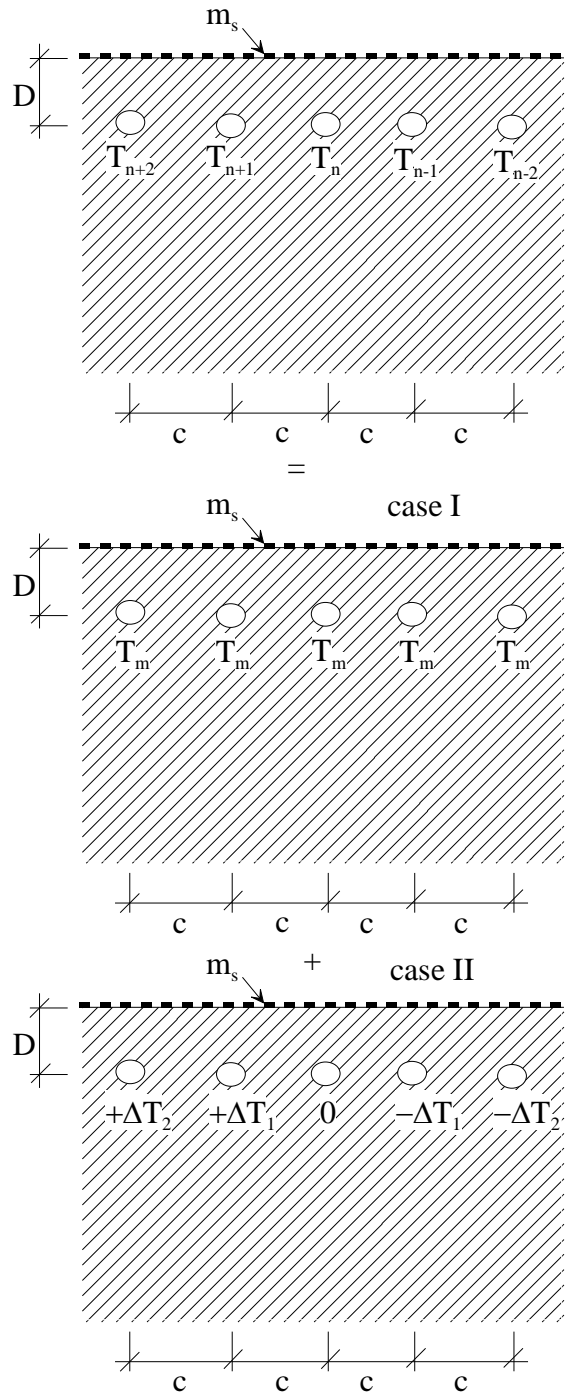


Figure 4. Pipes in a semi-infinity domain divided into two cases by using the principle of superposition. The temperature in the pipes in case I is T_m . In case II the temperature in each pipe is equal to the temperature difference, ΔT_i , from the mean temperature in case one.

The thermal resistance between a pipe and the interior is basically independent on the thermal resistance below the pipes. The simulated released heat to the interior, for the case shown in Figure 3, is 4.7705 W/m when the material below the concrete slab consists of thermal insulation with the thermal conductivity of 0.04 W/mK, and thickness 0.3 m. When instead the material below the slab only consists of soil with the thermal conductivity of 2 W/mK, the released heat to the interior is 4.7044 W/m. The difference between the cases is small (~1.4 %). The same results are achieved for other similar cases. This means that the thermal resistance between the heat pipes and the interior is basically only depending on the material that embeds the heat pipes and the slab surface conditions.

THERMAL RESISTANCE BETWEEN PIPES IN AN ARRAY AND THE INTERIOR

In order to determine the thermal resistance, a theoretical model for pipes in a semi-infinite domain is used. By using the principle of superposition the thermal process can be divided into two cases, see Figure 4. The pipe has the distance D from the surface of the soil to the center of the pipe. The distance between the pipes is c (m). The surface thermal resistance is m_s (m²K/W).

In case II in Figure 4 the temperature deviation from the mean temperature is illustrated for a linear drop of temperature along the whole pipe. This gives a net heat flow to the interior equal to zero. Even for a nonlinear temperature drop along the pipe, the analysis of the case with the average pipe temperature is sufficient.

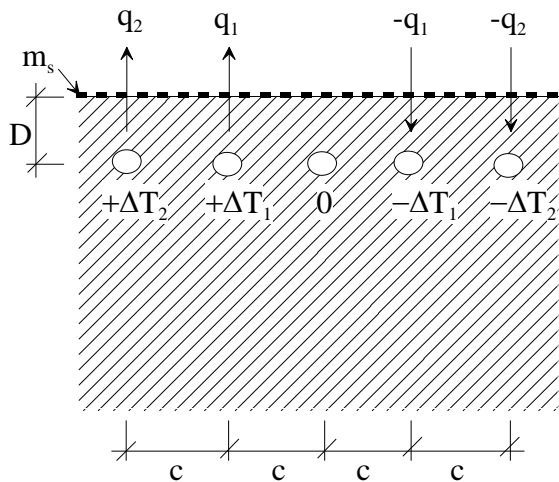


Figure 5. The heat flow, q_i , from the pipes to the interior air caused by the temperature difference ΔT_i .

THERMAL RESISTANCE FOR A SINGLE PIPE

For a single pipe in a semi-infinite heat flow domain (x -horizontal, z -vertical downwards) the temperature becomes (Claesson et al 1983):

$$T^0(x, z) = \frac{q}{2\pi\lambda} \left(\ln \left(\frac{\sqrt{(x^2 + (z+D)^2)}}{\sqrt{(x^2 + (z-D)^2)}} \right) + 2 \cdot \text{Re} \left(e^v \cdot E_1(v) \right) \right)$$

$$v = \frac{D + z + i \cdot x}{d} \quad d = m_s \cdot \lambda \quad E_1(v) = \int_v^\infty \frac{1}{s} e^{-s} ds$$
(1)

The heat flow from the pipe is q (W/m). The thermal conductivity in the domain is denoted by λ (W/mK). Re represents the real value and i the imaginary unit.

The temperature at the circumference of the heat pipe, with the exterior radius equal to R (m), in a semi-infinite homogeneous material layer, shown in Figure 6, can be calculated from the following expression:

$$T^0(R) = \frac{q}{2\pi\lambda} \left(\ln \left(\frac{2D}{R} \right) + 2 \cdot e^{2D/d} \cdot E_1(2D/d) \right)$$
(2)

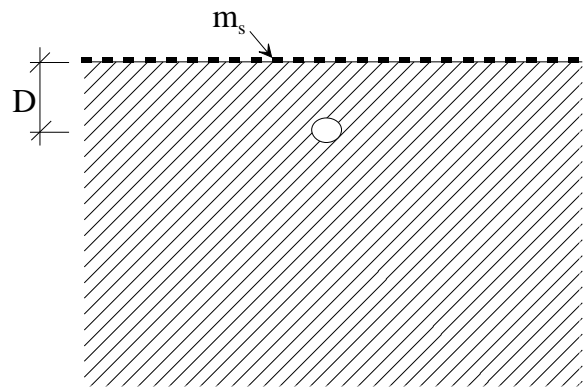


Figure 6. A heat pipe in a semi-infinite domain.

The thermal resistance, m , between the pipe and the surface is then:

$$m = m_0 + \Delta m$$

$$m_0 = \frac{1}{2\pi\lambda} \ln \left(\frac{2D}{R} \right)$$

$$\Delta m = 2 \cdot e^{2D/d} \cdot E_1(2D/d)$$
(3)

The first term m_0 in (3) represents the case with no surface resistance.

THERMAL RESISTANCE FOR A SINGLE PIPE IN AN INFINITE ARRAY OF PIPES

According to the results in Figure 2, each pipe contributes equally to the heat flow to the interior. The situation can be theoretically modeled using strip domains with adiabatic surfaces and with a single pipe in the middle, see Figure 7.

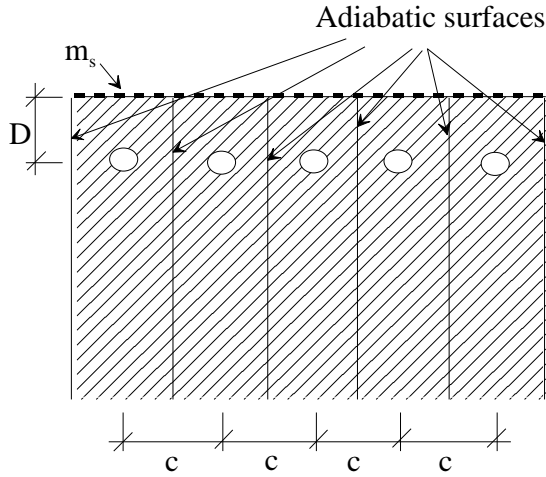


Figure 7. The theoretical model is based on that the domain is divided into strips with equal width and with adiabatic surfaces at the strip boundaries.

The temperature of the pipe in the middle is affected by all the others pipes (or it can be interpreted as heat reflections at the strip boundaries). The temperature in Equation (2) will therefore be corrected by taking into account the influence of the other pipes:

$$T(R) = T^0(R) + \Delta T_p \quad (4)$$

The last factor on the right hand side represents the influence that the other pipes have on the pipe in the middle. By summing up all these disturbances from the surrounding pipes we get:

$$\Delta T_p = \frac{q}{\pi \cdot \lambda} \sum_{n=1}^{\infty} \left(\ln \left(\frac{\sqrt{(n \cdot c)^2 + 4D^2}}{n \cdot c} \right) + 2 \cdot \text{Re} \left(e^{\nu} \cdot E_1(\nu) \right) \right) \quad (5)$$

$$\nu = \frac{2D + i \cdot nc}{d}$$

The thermal resistance becomes:

$$m = m_o^* + \Delta m^* \quad (6)$$

Using the formula for an infinite array of heat sources without surface resistance (Claesson 1983), i.e. the summation of logarithms, we get:

$$m_o^* = \frac{1}{2\pi \cdot \lambda} \ln \left(\frac{c}{\pi \cdot R} \sinh \left(\frac{2\pi D}{c} \right) \right)$$

$$\Delta m = \frac{2}{\pi \cdot \lambda} \text{Re} \left(\sum_{n=1}^N e^{\nu} \cdot E_1(\nu) \right) + \frac{1}{\pi \cdot \lambda} e^{2D/d} E_1(2D/d)$$

$$\nu = \frac{2D + i \cdot nc}{d} \quad (7)$$

The first term m_o^* in (6) represents the case with no surface resistance. The formula is known from e.g. (Holman, 2010).

EXAMPLE

The analytical formulas are validated against numerical simulations using the program HEAT2 (Blomberg, 1996) on the problem defined by Figure 8.

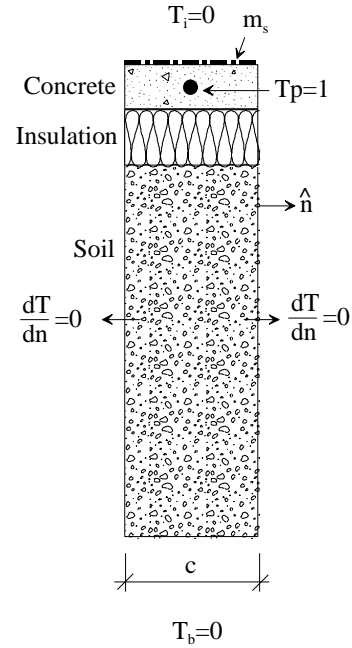


Figure 8. The theoretical model in the case with surface resistance. The interior temperature, T_i , is 0°C , the temperature at the bottom, T_b , is 0°C and the temperature in the pipe, T_p , is 1°C . All other surfaces is adiabatic. The space between the heat pipes is c .

Table 1: Input data for simulation of the thermal resistance in the program HEAT2.

	λ (W/mK)	Thickness (m)
Concrete	1.7	0.1
Insulation	0.04	0.3
Soil	2.0	~10
c (m)		0.1-0.3

The comparison, between the analytical formula and the results from the numerical simulation, shows a very small difference of maximum 2.6%. See also Figure 9.

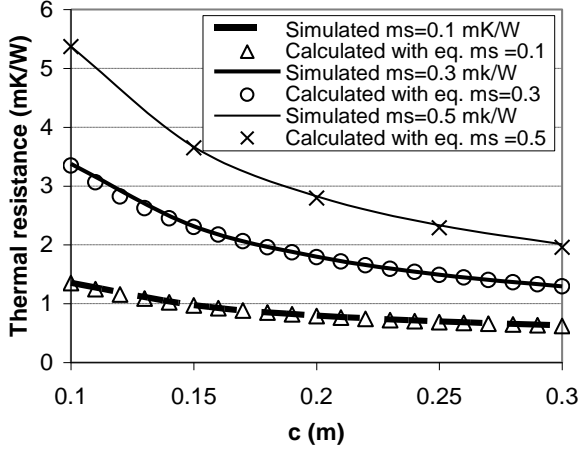


Figure 9. The thermal resistance between one of the pipe and the interior. The presented results is based on simulation (sim) with the program HEAT2 and calculated (eq) with equation (7) according to the strip case presented in Figure 8. The space, c , between the heat pipes is varying between 0.1 to 0.3 m. The thermal resistance of the surface, m_s , is varying between 0.1 to 0.5 m^2K/W .

The result is compared with a complete foundation construction as in Figure 1. The average pipe thermal resistance, with 9 heat pipes and varying space c , is shown in Figure 10.

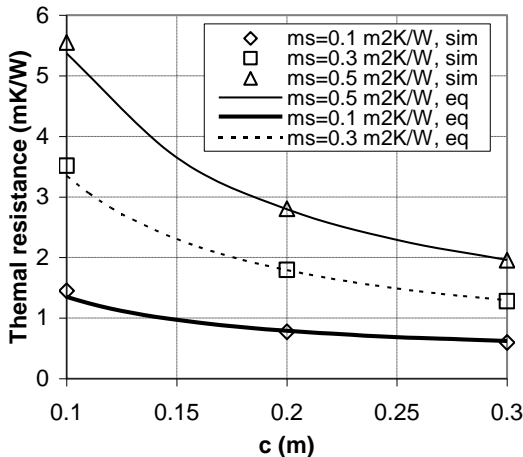


Figure 10. The thermal resistance between the heat pipe the ground calculated (equation) and simulated (with HEAT2) surface according to the case presented in Figure 1. The thermal resistance of the surface, m_s , is varying between 0.01 to 0.5 m^2K/W . The distance between the heat pipes is varying between 0.1 to 0.3 m.

The error of the pipe thermal resistance is less than 7%. The error is greatest for the case with shortest distance between the pipes and the lowest surface resistance.

The results show that the equation can be used to calculate the thermal resistance between the heat pipe and the interior air with great accuracy, at least for the analyzed cases with rather small surface resistances, representing floor covering with small thicknesses.

MAXIMUM SURFACE TEMPERATURE FOR AN INFINITE ARRAY OF PIPES

In order to keep the surface temperature controlled we need to know the maximum one. The highest increase in the surface temperature, ΔT , due to the pipes is found right over one of the pipes ($x=0, z=0$). It becomes:

$$\Delta T(0,0) = \frac{q}{\pi\lambda} \left(e^{D/d} \cdot E_1(D/d) + 2 \sum_{n=1}^N \operatorname{Re}(e^v \cdot E_1(v)) \right)$$

$$v = \frac{D + i \cdot nc}{d}$$
(8)

The first term represents the surface temperature for a single pipe in a semi-infinite domain.

DESIGN RULES

Now we can write down the general formulas for dimensioning a floor heating system.

Assume that the following building heat demand for the floor heating is equal to Q (W), and the total length of the pipe is L (m), we have:

$$q = \frac{Q}{L}$$
(9)

With a specified total, approximately linear, temperature drop along the pipe of ΔT ($=T_f - T_r$), the feed forward temperature becomes:

$$T_f = T_i + q \cdot m + \frac{\Delta T}{2}$$
(10)

This formula needs to be altered in order to cover non-linear temperature drop along the pipe.

Using the performance factor η (-) for the floor heating (Roots, Hagentoft 2005) we have total heat flow from the pipe equal to:

$$Q_{total} = \frac{Q}{\eta}$$
(11)

Where

$$\eta = 1 - U \cdot \left(m_s + \frac{D}{\lambda} \right) \quad (12)$$

Here, U ($\text{W}/\text{m}^2\text{K}$), is the U-value of the foundation (From interior to exterior). It can be found from (Hagentoft, 1988) or (ISO-EN 13370).

For the case when the floor is covered by a material layer and we need to determine the increase in the surface temperature on top of this (the surface in contact with the interior air) we get:

$$\Delta T_s = \frac{m_{si}}{m_s} \Delta T(0,0) \quad (13)$$

Here, m_{si} ($\text{m}^2\text{K}/\text{W}$) represents the surface heat transfer resistance between the interior and the floor surface.

With a fluid specific heat capacity of c_f ($\text{J}/\text{kg } ^\circ\text{C}$) and a density of ρ_f (kg/m^3) we get the following requirement for the fluid volumetric flow rate \dot{m}_f (m^3/s):

$$\dot{m}_f = \frac{Q}{c_f \rho_f \cdot (T_f - T_r) \cdot \eta} \quad (14)$$

CONCLUSION

This study has shown that simple handy design formulas, based on analytical solutions, can be used for well-insulated foundations with small floor surface resistances. The formulas can handle both the dimensioning of the maximum surfaces temperature as well as the flow rate determination.

REFERENCES

- Karlsson 2010, Thermal Modelling of Water-Based Floor Heating Systems - supply temperature optimisation and self-regulating effects. ISBN 978-91-7385-369-9, Civil and Environmental Engineering, Chalmers University of Technology, Sweden.
- Claesson, Dunand 1983, HEAT EXTRACTION FROM THE GROUND BY HORIZONTAL PIPES - A mathematical analysis. Report DI:1983. Swedish Council for Building Research.
- P. Roots, C-E. Hagentoft. Ground heat losses from a slab with floor heating *International Building Physics Conference*, TU Eindhoven, September 2000.
- Hagentoft C.-E. Roots P., *Floor heating - Problems in the Control system*. Performance of Exterior Envelopes of Whole Buildings VIII, Clear Water Beach FL, 2001.
- P. Roots, C.-E. Hagentoft. Floor Heating – Heating demand, *6th Symposium on Building Physics in the Nordic Countries, Trondheim*, June 2002.
- P. Roots, C.-E. Hagentoft. Released Heat from a Line Source in a Foundation Construction. *7th Nordic Symposium on Building Physics, Reykjavik, Iceland*, June 12-15, 2005.
- Claesson J, Hagentoft C-E. 1991. Heat loss to the ground from a building. I: General theory. *J. of Building and Environment*, Vol. 26, No.2, pp. 195-208.
- C.E. Hagentoft, Claesson J., 1991. Heat loss to the ground from a building. II: Slab on the ground. *J. of Building and Environment*, Vol. 26, No.4, pp. 395-403.
- Hagentoft C-E., 1988, Heat loss to the ground from a building. Slab on the ground and cellar, LTH/TVBH-1004, doctoral thesis. Building Physics, Lund
- Blomberg, T. (1996). *HEAT CONDUCTION IN TWO AND THREE DIMENSIONS Computer Modelling of Building Physics Applications*. Department of Building Technology, Building Physics, Lund University, Lund, Sweden.
- Roots P. and Hagentoft C.-E. (2005). Released heat from a Line Source in a Foundation Construction. *Proceedings of the 7th Symposium on Buildings Physics in the Nordic Countries*, 839-844. Reykjavík, Iceland.
- Holman J.P. (2010). Heat transfer, 10th edition, Department of Mechanical Engineering Southern Methodist University. ISBN 978-0-07-352936-3

EXPLORING FLOODING AND RISING WATER PROBLEMS RELATED TO HERITAGE; CASE STUDY ST. CATHERINE'S CHAPEL, LEMIERS, THE NETHERLANDS

H.L. Schellen¹, Z. Huijbregts¹, K.P. Ziel¹, A.W.M. v. Schijndel¹ and R.P. Kramer¹
¹Eindhoven University of Technology, The Netherlands

ABSTRACT

In a chapel wall paintings are deteriorating for years. The paintings have started to crack and peel off from their background. There were indications about expected high groundwater levels due to a nearby lying Selzer creek and its flooding. In the past two years several climate conditions in and around the chapel have been measured. The chapel has been modelled with a multi-zone model for heat and vapour flows in a building giving boundary conditions for the walls and foundation finite element model. The course of rising moisture was investigated. The results show that rising moisture nearly always takes place.

INTRODUCTION

The interior of Saint Catherine's Chapel in Lemiers was painted by the artist Hans Truijen in 1977-1978. The paintings show Truijen's interpretation of the Christian story of creation and the life of Christ. Parts of the wall paintings have been significantly deteriorated because of moisture problems in the church. The aim of this study is to provide environmental data that would help explain the deterioration of the wall paintings and to give recommendations on how the indoor climate in the church can be improved. For a period of two years continuous measurements have been performed on the outdoor and indoor climate conditions as well as the microclimate conditions close to the walls. In addition, instantaneous measurements of the moisture content of the walls have been carried out. Furthermore, hygrothermal building simulation models of the church have been created to derive heat and moisture sources in the building. With help of these models, sustainable strategies have been investigated to diminish the moisture problems in the church.

The building

History

Saint Catherine's chapel is a hall church in Romanesque style. It dates either from the second half of the 11th century or from the 12th century. Among the foundations are remains of an even older building, probably from the 8th century, the time of

Charlemagne. The choir was added in either the 13th or 14th century, possibly in 1350, when the building was consecrated to St. Catharine. Until then the chapel has belonged to the nearby situated castle.

As a whole, the building is the only complete surviving example of the earliest type of stone churches known in the Netherlands, a one-aisled building without a tower (Figure 1). Despite its later addition, the rectangular closed choir is typical for these earliest churches as well.

The building has undergone several changes: in 1648, the choir was heightened and vaulted and the small turret was added to the roof. In 1683, the small windows were enlarged. In 1893-1897, after a new church was built in the village, the chapel was closed and restored by P.J.H Cuypers, who reconstructed the small windows and closed the large ones. In addition, the entrance in the south wall, which had been closed with brick, was reopened while the entrance at the north side, which dated from the 17th century, was closed. The building was registered as a Dutch state monument in 1967. On request, the chapel can be visited by a guided tour and is occasionally used for events.



Figure 1. The exterior of the church of Lemiers
(Source: nl.wikipedia.org 2012).

Building Environment

The church is located in Lemiers, in the municipality of Vaals (Limburg), at coordinates 50.47° latitude and 5.59° longitude (Figure 2). The church was probably built on the site of a former religious

building. The surrounding buildings in the street are low-rise buildings, so these building do not form obstacles for the entering of daylight. However, trees at the north side of the church and the nearby building at the west side block the entering of sunlight during a few hours in the afternoon.



Figure 2. Map of Lemiers, The Netherlands. The location of the church is indicated by a red dot, the flooding creek by a blue dot [Source: Google maps]

Constructional analysis

The typical ground plan of a church in Romanesque style is a basilica plan with three naves and a transept. Small rural churches usually consist of a longitudinal plan, oriented from east to west, with a simple central nave and an altar at the east side.

The nave has a rectangular shape and has no side aisles (Figure 3). The ground floor in the nave consists of approximately 300mm sand, 100mm concrete and 27mm natural stone marble floor tiles. The floor of the altar has a surface uplift of 150mm with respect to the central nave floor. The floor is not thermally insulated.

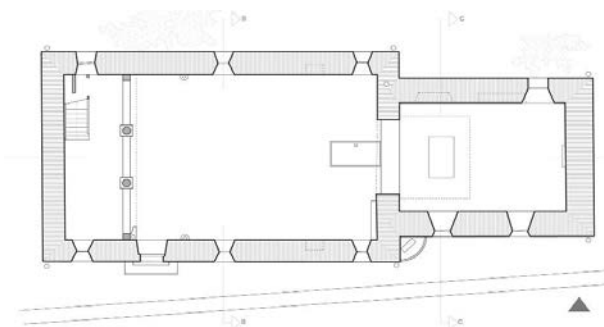


Figure 3. Ground plan of the church

From the outside, the church is accessed through a door located on the south wall of the central nave. The door is made of timber and has a thickness of 70mm.

Inside the nave, a stair brings one to the choir. The floor of the choir consists of a timber construction with a total thickness of 185mm. The central nave is wider and higher than the altar. The crypt, a domed space of rectangular-shaped where the relics of the saints were kept, is located below the altar. It has a depth of 3.10 meters and a length of 2.80 meters. The

estimated floor construction of the crypt consists of 300mm sand, 150 gravel concrete and 150mm concrete.

The central nave has a width of approximately 5.60 meters and a depth of approximately 10 meters. The altar has a width of approximately 3.70 meters and a depth of approximately 5.40 meters. The internal wall between the central nave and the altar is made of masonry, is on both sides covered with plasterwork and has a thickness of 750 mm.

The central nave has a barrel-vaulted roof construction, which replaced the original wooden roof for security purposes. The roof is composed of a series of semi-circular arches, which are reinforced by three transverse arches that divide the barrel-vaulted in four equal sections. The external walls support the roof construction. The vault of the central nave is made of wooden beams that are fixed to a wooden construction. Two fan vaults, completely constructed out of stone, cover the altar.

The vault of the central nave starts at approximately 4.1 meters above the ground floor and its highest point is located at approximately 6.2 meters above the ground floor.

The attic floor above the altar is made of plasterwork and natural stone and concrete. The vault of the altar starts at approximately 2.20 meters above the ground floor. The highest point of the vault is located at approximately 4.30 meters above the ground floor. The attic above the nave can be reached via the attic above the central nave.

The main supporting elements of the church are the stone walls. The thick masonry walls provide a high thermal mass. The outdoor walls are free of adornments, the facade is very uniform, linear and crude and the stones are unpolished; these are all characteristic elements of the simple Romanesque style.

The external walls of the nave are made of masonry with lime mortar; their thickness varies between 750 and 900mm.

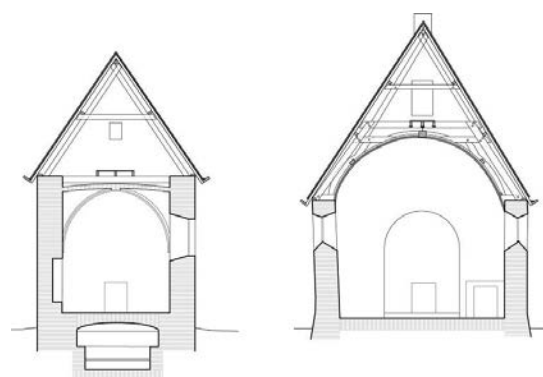


Figure 4. Cross sections of the chapel

For structural reasons, the windows had to be rather small. Moreover, the church served as a place of shelter, so there was also a need for the door and windows to be small. For this reason, the amount of daylight entering the church is very limited. The external walls of the nave contain 10 windows. All

the window panes are made of leaded glass and are divided in parts with frames made of steel. The windows contain blank single glazing. Only two windows can be opened for ventilation of the church: W2 at the south wall and W7 at the north wall. The windows of the central nave have a textile protection inside, probably to protect the painting from direct solar radiation. The furniture in the church is sober: some wooden benches and chairs are placed around the perimeter of central nave. There are several cracks present in these benches, which could be caused by unfavorable climatic circumstances at the time the church had warm air heating. A stone pulpit is located on the altar. The internal walls are covered with plasterwork, on which the famous frescoes of Hans Truijen were painted.

MEASUREMENTS

The measurements performed in this study have various objectives: one is to get a complete image of the current indoor and outdoor climate of the church and to relate these conditions to the deterioration of the wall paintings; the other objective is to provide data for the simulation model and to validate the outcome of the model. When the outcome of the model is in agreement with the measurements, the model will be used to answer a number of research questions.

The measured parameters of this research can be divided into instantaneous and continuous measurements. Instantaneous measurements have been carried out for the moisture content of the walls and the groundwater level.

Continuous measurements were taken of the following parameters:

- Outdoor and indoor air temperature
- Outdoor and indoor air relative humidity
- Indoor surface temperature
- Indoor surface relative humidity
- Heat flux of external walls
- CO₂ concentration
- Global solar radiation

Moisture content of the walls

The subsurface moisture content of the walls was measured by a digital microwave measuring tool.

For measuring the moisture content, the measuring tool takes the relative high dielectric constant of water in comparison to the dielectric properties of other materials. For example, common sand has a dielectric constant of about 4 compared to the dielectric constant of water, which is about 80. So when a value of 80 is measured one can conclude that the material is fully saturated with moisture. However, this measuring tool is limited in its accuracy, since it can only measure up to a depth of 300mm. The penetration depth is reduced further when the region near the surface of the wall is fully saturated with moisture or when water is dripping from the wall. On the other hand, the measuring device gives a clear indication of dry or wet materials at the surface.

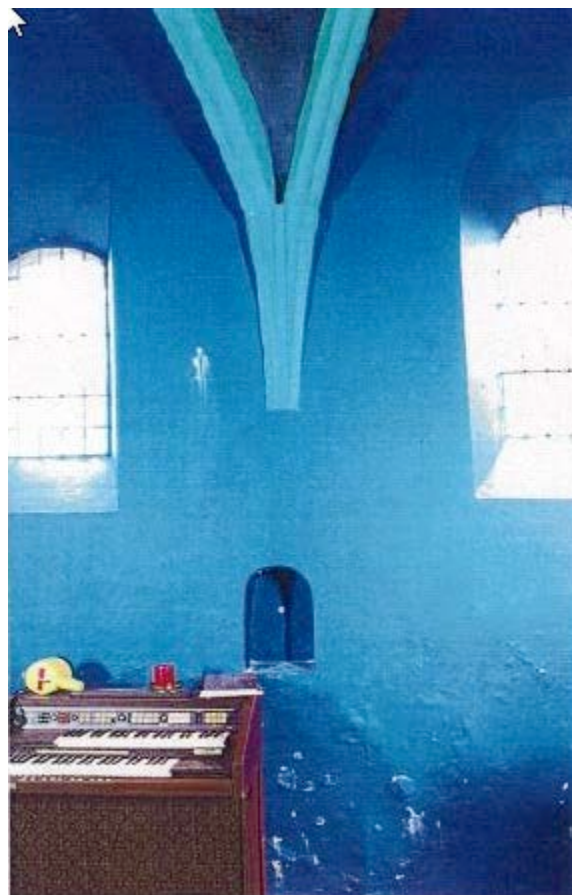


Figure 5. Damaged wall painting in the chapel up to about 1 m above floor level

Measurements of the moisture content of the walls were performed twice: on October 26th 2012 and on the 4th of March 2013 (Muñoz, C.M. et al. 2013). These measurements were performed close to the floor, so at a height of approximately 0 meters, further on at a height of 0,5m from the floor and at 1-meter height. The distance between the measuring points was approximately 1 meter. At the very first visit to the chapel, before the start of the research, the crypt was completely flooded: up to the entrance hatch. During the first measurements, the water level in the crypt was a few centimetres measured from the hatch of the crypt as can be seen in figure 6. During the second measurement campaign the crypt was dry. Figure 7 gives an indication of the average measured results.

It can be noticed that the highest dielectric values were measured closely to the floor and in the wall above the crypt between nave and altar. In these areas the loss of wall paintings has also been severe. Furthermore, the measurements indicated rising moisture caused by high ground water levels.

Groundwater level

Apart from measuring the moisture content in the walls, the ground water level has been measured. At the north side of the chapel, closely to the corner of the nave and choir, a monitoring well has been constructed. Weekly measurements indicated high ground water levels. There was a small fluctuation in

the groundwater level, up to 10 centimetres. Yearly the level is quite steady-state around 75 centimetres below ground-level.



Figure 6. Entrance of the wet crypt with a few centimetres of water at the bottom

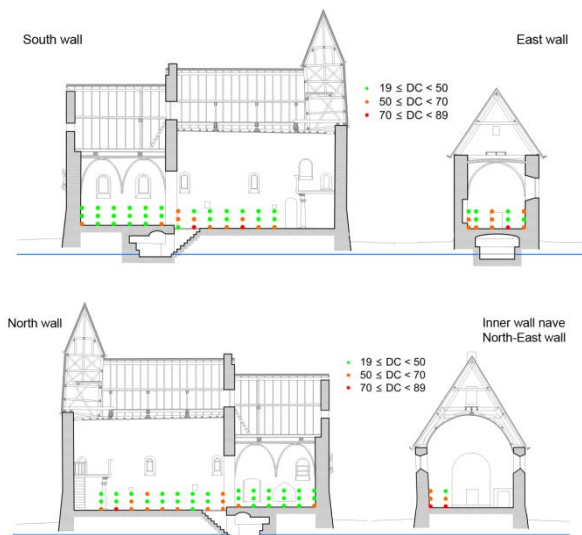


Figure 7. Indication of the averaged measured dielectric constant, representing moisture content in the chapel's walls; the blue line indicates the mean groundwater level

SIMULATION

HAMBase

The multi-zone hygrothermal building simulation model HAMBase (Wit et al. 2006) was used to calculate the indoor temperature (T_i) and relative humidity (RH_i) inside the chapel as a result of the outdoor climate conditions, the building properties, the climate control system and the building use. HAMBase characterizes the indoor climate by uniform values for radiant temperature, air temperature and RH per zone.

The HAMBase model of the church consists of three zones: the chapel, the attic and the crypt. The indoor climate conditions were first simulated for a constant ventilation rate per zone and without internal heat loads, additional vapour sources and heating plants. Secondly, the additional demands for (fictive) heating, cooling, humidification and dehumidification were calculated in HAMBase by setting the measured temperature and RH as set

points for the minimum and maximum temperature and RH in the HAMBase model.

A comparison between the measured and in this way simulated indoor temperature, RH and humidity ratio in the chapel showed that the simulated temperature was slightly lower than the measured temperature.

Inverse modelling

Besides the use of HAMBASE, which is a forward modelling approach, a multi-zone model was developed using Inverse Modelling. Inverse Modelling is also called System Identification (Kramer R.P. et al. 2013).

Inverse Modeling is the inverse of traditional modeling. In traditional modeling, the system is known and the output is unknown. By modeling the system, the output can be simulated.

In Inverse Modeling, the output is known, e.g. measured, but little is known about the system's parameters. The objective is to identify the parameter values of the model by repeatedly trying different parameter values and comparing the simulated output with the measured output.

The goal is to minimize the simulation error, formulated as an objective function, e.g. mean squared error. The process of finding the parameter set, which minimizes the objective function, is called optimization.

Lemiers' church has also been modeled using Inverse Modeling. Six models were identified: a thermal and a hygric model for the three zones: attic, chapel, crypt. Because the models are represented in State Space form, the simulations are very fast: 1 year with hourly time steps is simulated in 0.016 seconds on an ordinary computer (i5-processor). After validation of the identified models, the three thermal models were coupled resulting in one multi-zone thermal model and the three hygric models were coupled resulting in a multi-zone hygric model.

RESULTS

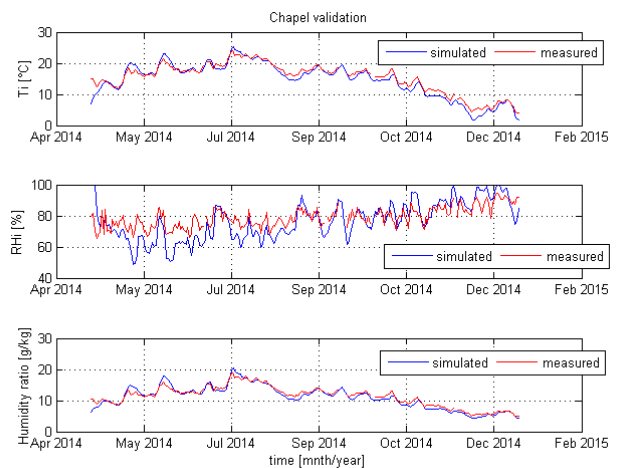


Figure 8. Chapel: comparison between the simulated and measured data

As mentioned before, the chapel was divided into three zones: chapel (nave + choir), attic and crypt. In the following sections a comparison is made between the measured data and the simulated data.

Chapel

A first comparison in the output was made for the nave and choir, defined as the zone called chapel. The differences between the original model and the optimized model are small, but noticeable as can be seen in figure 8.

Attic

The simulation results were validated with the measurements and show a near agreement with each other as can be seen in figure 9. During summer the temperature in the attic is slightly higher compared to the measurements.

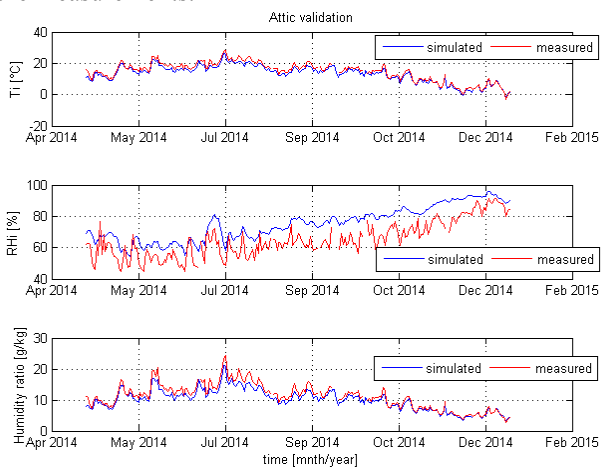


Figure 9. Attic: comparison between the simulated and measured data

Crypt

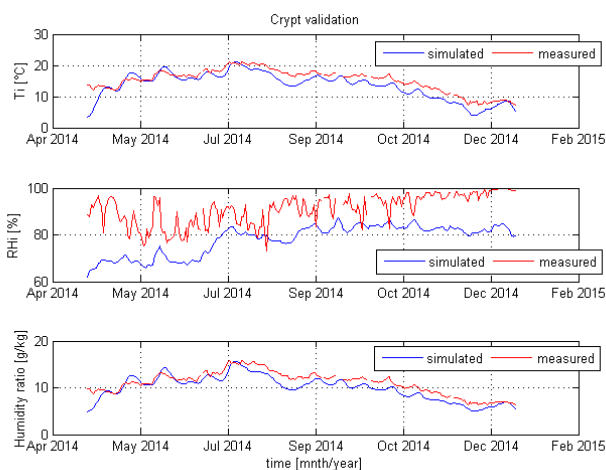


Figure 10. Crypt: comparison between the simulated and measured data

For the validation with the measurements the absolute humidity in the crypt compares well, although the relative humidity is still much higher compared to the simulation, for which most deviation occurs during winter.

No additional moisture source was modelled in the crypt, while during certain periods a layer of water appears at the bottom of the crypt which evaporates. To model the quantity of moisture inversely, the profile for the crypt was set different. The relative humidity was set equal to the measured relative humidity of the crypt. So evaporation and condensation lead to humidification and dehumidification, which was determined by inverse modelling (Kramer R.P. et al. 2013). Both humidification and dehumidification were activated in the model in order to match the relative humidity curve with the measured data.

As can be seen in figure 10, the relative humidity of the measured data is a highly fluctuating curve. This led to a demand in (artificially modelled) humidification and dehumidification in order to match this highly fluctuating curve. If an average is taken between humidification and dehumidification, the quantity of moisture is more or less in balance and smaller than it appeared at first sight. Most measured data of the relative humidity were above 80% as can be seen in figure 10 and 11. This is the range for which this kind of measuring equipment shows large deviation with the calibration.

Another cause that could have led to the large deviation in relative humidity is related to the lower air temperatures in winter for which deviation is large. Closer looking into the background of the relative humidity, a plot was made of the Mollier diagram. Figure 12 shows that for lower air temperatures the (curved) lines of the relative humidity are closer to each other.

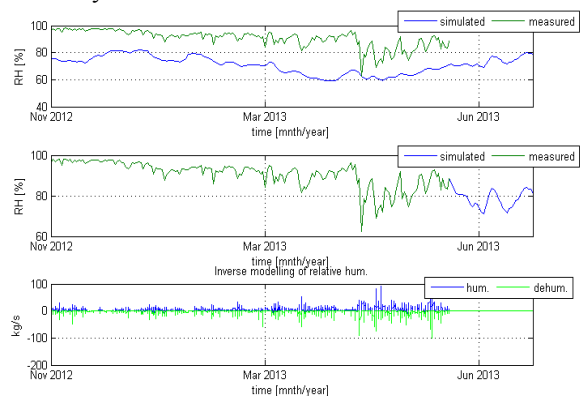


Figure 11. Inverse modeling of the relative humidity, with the activation of (artificial) humidification/dehumidification in order to match the measured data

This means that for a slight deviation (of less than one degree Celsius) in air temperature this could mean a large deviation in relative humidity (up to 10%). Together with the higher inaccuracy of the measuring equipment and not modelling an additional moisture source this can be seen as the main cause for the (at first sight) large deviation between simulated and measured results. Besides, the measuring equipment in the crypt is placed on the screen of the crypts access hatch (figure 14).

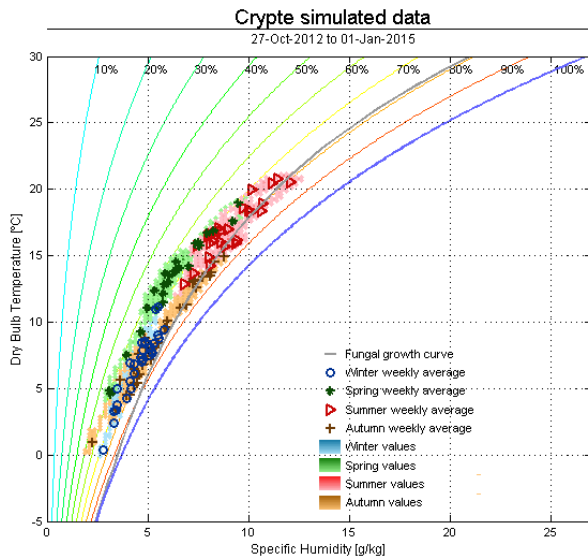


Figure 12. Mollier diagram of the simulated data

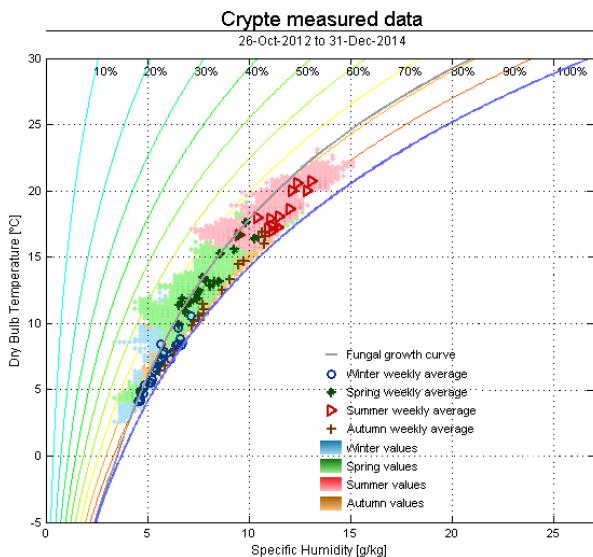


Figure 13. Mollier diagram of the measured data



Figure 14. Crypt entrance: measurement equipment is placed on the screen of the hatch between chapel (nave) and crypt

This means that the crypt is in open connection with the chapel. Therefore, the measured data of the crypt can be influenced by the chapel, but to what extent has not been considered further.

Summarized, the indoor climate conditions do not immediately indicate a relation with the damages that occur in the chapel. Surface condensation did occur as the measurements indicated, but not as frequently as the damage indicated. Validation between the simulated indoor climate and measured climate conditions corresponds quite well. The difference in the results is due to the difficulty of setting user profiles that correspond exactly with the logbook, which is too time consuming to model. Also the inaccuracy of the measuring equipment decreases for higher relative humidities. Finally, as just has been pointed out, the zone that has shown most deviation is the crypt. Here the measuring equipment is placed on the screen between crypt and chapel (nave), and an additional moisture source has not been modelled, which may have influenced the measured data.

Finite element modeling

This chapter focuses specifically on the moisture problems (2D) in the walls using a multiphysics finite element package COMSOL.

Moisture Transfer

When a wall is in contact with water, moisture will rise by capillary suction. This depends on the capillary properties of the wall (e.g. the water sorption coefficient, radius of the capillary pores), but also on the evaporation at the surface. In narrow capillaries the water rises higher than in wide ones. Although, in a vertical capillary the flow will stop eventually by gravity. Since the capillary properties of the construction are unknown, focus lays on other aspects of moisture transfer.

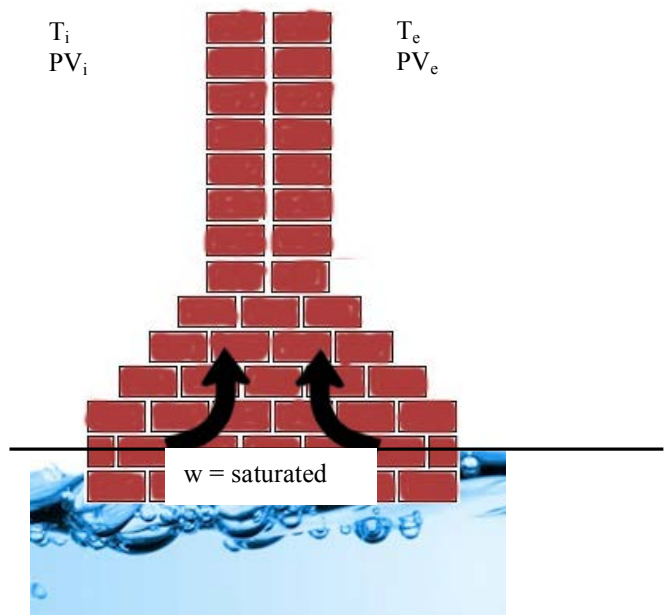


Figure 15. Visualization of the 2D moisture transfer in the chapel's wall due to a saturated foundation

The moisture transfer equation used combines two extremes: the vapour transfer equation and the liquid water transfer equation. There are three possible

moisture potentials in the moisture transfer equation that can be measured/solved, namely: relative humidity, capillary pressure and the moisture content. The moisture content is preferable above the other two, because it is the only one that can be measured in a construction.

Figure 15 visualizes the construction and its basic behaviour: wetting and drying of the walls in both directions and a constant upward force of water on the foundation. Parameters mentioned in the figure can all be implemented from the HAMBBase model. So for this specific case the moisture transfer equation for the moisture content becomes:

$$\frac{\delta w}{\delta t} = \text{div } D_w \text{ grad } w$$

For which the diffusion coefficient D_w varies with the moisture content:

$$D_w = \frac{\delta a}{\mu} p_{sat} \frac{1}{\xi} \text{ for vapour transfer}$$

$$D_w = \frac{\kappa_m}{\Xi} \text{ for liquid water transfer}$$

The moisture content is not continuous at an interface between two different materials. In this case there is only one material (the contact with the soil is modelled as zero flux boundary), that is why the moisture content is chosen as potential. Figure 16 shows an example (Wit, M.H. 2009) of the diffusion coefficient for vapour and liquid moisture transport.

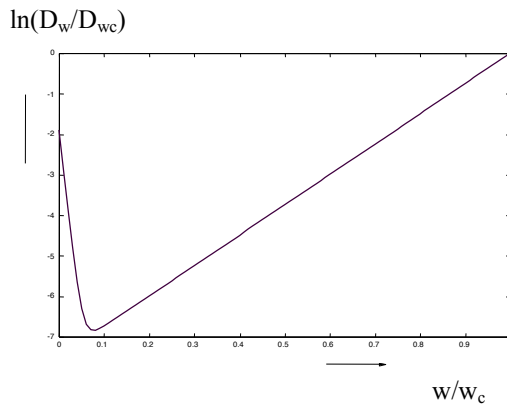


Figure 16. Function of the diffusion coefficient varying with the moisture content. Left part vapor transfer, right part liquid transfer

The moisture diffusivity in the liquid part (so the right part of the figure) is represented by an exponential function. In the vapour part (so the left part) the diffusion coefficient is a decreasing function of the moisture content, while for liquid the opposite occurs as it is increasing. The diffusion coefficient has a minimum near the critical moisture content.

PDE Comsol

The COMSOL module called 'Coefficient Form PDE Interface (c)' was used for this study in version 5.0. This tool contains the feature of a scalar coefficient form equation that is described by a balance equation (Williams Portal, N.L. 2011). The balance equation contains a single dependent variable u that is an unknown function on the computational domain Ω . For this study the single depend variable u is the moisture content w .

The partial differential equation (PDE) in COMSOL is described by the following:

$$e_a \frac{\partial^2 u}{\partial t^2} + d_a \frac{\partial u}{\partial t} + \nabla(-c\nabla u - \alpha u + \gamma) + \beta \nabla u + \alpha u = f$$

$$-n * (-c\nabla u + \alpha u - \gamma) = g - qu$$

The upper equation is the PDE that must be satisfied within the computational domain Ω . Whereas the lower equation is the Neumann boundary condition that must hold on the domain boundary Ω . Since the convective vapor transfer within the material is neglected in this study, the coefficients e_a , α , β , γ and a are equal to zero. Therefore, the equation can be simplified to:

$$d_a \frac{\partial u}{\partial t} + \nabla(-c\nabla u) = f$$

$$-n * (-c\nabla u) = g - qu$$

In the equation above n is the outward unit normal vector on $\partial\Omega$ (-). From the material properties c is the diffusion coefficient D_w that has been implemented. As mentioned before u is the dependent variable that is unknown, in this case the moisture content w . Adding a damping or mass coefficient d_a of 1 to the upper equation makes the problem transient. The lower equation defines the boundary conditions whereas g is defined as the flux/source. If no boundary absorption is assumed, then q is equal to zero.

At the top boundary of the model a so-called zero flux condition is assumed. At the bottom boundary according to figure 15 the foundation is saturated, so that the moisture content is at its capillary value. Therefore, a Dirichlet boundary condition was applied here in the model, so a boundary within the model with a fixed value w_c .

Model setup

The entered parameters for the constructed model are described in table 1. Properties for the diffusion coefficient and critical moisture content are assumed to be the same as for brick.

The graph of the moisture content w (kg/kg) as a function of relative humidity (-) is called the sorption curve and is plotted in Figure 17.

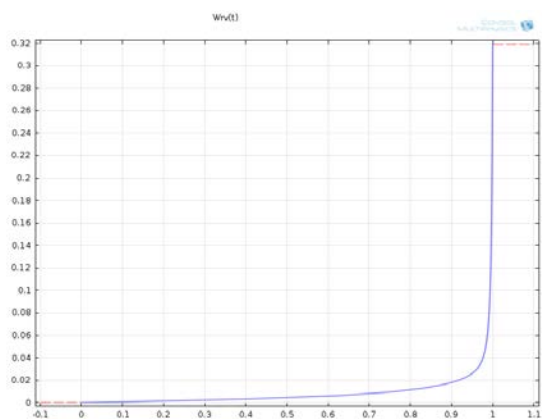


Figure 17. A plot of the sorption curve $w=f(\phi)$ (kg/kg) for brick plotted from COMSOL

Figure 18 shows the uptake of water of the wall construction of the chapel due to the continuous contact of water with the foundation. Apart from the unknown exact material properties of wall and foundation, the results clearly indicate the effect of water uptake on the surface moisture content near the floor.

Table 1:

Model parameters diffusion

Parameter	Value	Unit	Definition
D_w	$2.1 * 10^{-9} e^{0.0316 * w}$	m^2/s	Diffusion coefficient
w_c	290	kg/m^3	Capillary moisture content
w_i	15	kg/m^3	Initial moisture content
T_e	$T_e(t)$	$^{\circ}C$	External temperature
T_i	$T_i(t)$	$^{\circ}C$	Indoor temperature
h_e	25	W/m^2K	External surface coefficient of heat transfer
h_i	7.7	W/m^2K	Internal surface coefficient of heat transfer
q_e	$h_e * (T_e - T_{se})$	W/m^2	External heat flux
q_i	$h_i * (T_i - T_{si})$	W/m^2	Internal heat flux
$\phi_e(t)$	$RH_e(t)/100$	-	Outdoor relative humidity
$\phi_i(t)$	$RH_i(t)/100$	-	Indoor relative humidity
β_e	$2 * 10^{-8}$	s/m	External surface coefficient of vapour transfer
β_i	10^{-7}	s/m	Internal surface coefficient of vapour transfer
$g_e(t)$	$\beta_e * (p_e - \phi_e(w)^* p_{sat}(T_{se}))$	kg/m^2s	External moisture flux
$g_i(t)$	$\beta_i * (p_i - \phi_i(w)^* p_{sat}(T_{si}))$	kg/m^2s	Indoor moisture flux
D	0.8	m	Thickness of the wall

RESULTS AND CONCLUSIONS

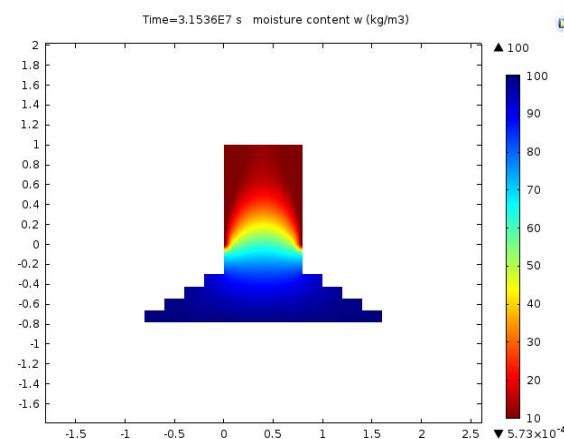


Figure 18: Moisture content $100 * w/w_c$ in the construction after one year

The evaporation of water at the bottom of the paintings, together with the transportation of salts, makes clear that the uptake of water is the main origin of the deterioration of the wall paintings in the chapel.

REFERENCES

- Kramer, R. P., Schijndel, van, A. W. M., & Schellen, H. L. , 2013. Inverse modeling of simplified hygrothermal building models to predict and characterize indoor climates. *Building and Environment*, 68, 87-99. 10.1016/j.buildenv.2013.06.001
- Muñoz, C.M; Huijbregts, Z; Kramer, R.P.; Schellen, H.L., 2013. *Saint Catharina Chapel, Lemiers*. University of Technology Eindhoven, Eindhoven.
- Schellen, H.L., 2002. *Heating monumental churches*. University of Technology Eindhoven, Eindhoven.
- Schijndel, A.W.M. van, 2007. *Integrated heat air and moisture modeling and simulation*. University of Technology Eindhoven, Eindhoven, PhD thesis.
- Williams Portal, N.L., 2011. *Evaluation of heat and moisture induced stress and strain of historic building materials and artefacts*. Chalmers University of Technology, Göteborg, Sweden.
- Wit, M.H. de, 2009. *Heat, Air and Moisture in Building Envelopes*. University of Technology Eindhoven, Eindhoven, Lecture book.
- Wit, M.H. de, 2006. HAMBBase, Heat, Air and Moisture Model for Building and Systems Evaluation, Bouwstenen 100, Eindhoven University of Technology; 2006

CALCULATING PARETO-OPTIMAL AIRTIGHTNESS LEVELS FOR RESIDENTIAL BUILDINGS

K. Maroy¹, Prof. Dr. N. Van Den Bossche² and B. Foré²

¹Faculty of engineering and architecture, Ghent University, Ghent, Belgium

² Faculty of engineering and architecture, Ghent University, Ghent, Belgium

ABSTRACT

Good airtightness results in a lower energy use, increased comfort and reduced risk for hygrothermal degradation. However, there is a lack of knowledge on the cost of airtightness measures, the relative impact of specific solutions on the overall airtightness and cost-optimal performance levels.

This paper presents a methodology to predict the performance and cost of airtightness measures and heating devices. When no airtightness level is imposed, it seems favorable to invest little in airtightness measures with respect to the fuel cost. When the passive house standard is imposed, the most cost-effective measures are concentrated in roof-wall, floor-wall and window-wall joints.

INTRODUCTION

Airtightness is one of the crucial factors in the overall thermal performance of buildings. Up to 10% of overall primary energy use is used to compensate for infiltration of cold air in buildings, built with the regulations of 2006. In addition, the impact of air leakages increases with the higher insulation levels of buildings. For an almost energy-neutral building, the percentage increases to 30% of the primary energy use for compensating airtightness (Wouters et al, 2012). Next to energy losses, air leakages cause cold draughts, surface condensation, mould growth through infiltrating air and distortions of the balance in the HVAC system. As the building codes and energy regulations only get stricter, the obliged airtightness level of buildings will only increase.

In Belgium, there is currently no general guideline for maximum air leakage rate defined for residential buildings. The effect of air leakages in the building envelope is not taken in account in energy calculations, unless a blower-door measurement is executed. Fortunately, the number of airtightness tests in new built dwellings is rising year after year. In 2009, the airtightness of only 7% of a new built dwellings was measured, in 2013 this was 55% and in 2014 almost 80% (Vlaams Energie Agentschap, 2015).

Only in cases where the passive house standard is required, the maximum leakage rate is fixed on $0,6 \text{ h}^{-1}$ (WTCB, 2012). It is likely to assume that this will become a general guideline in the future, as Europe imposes that all new built constructions should be almost energy-neutral by 2021.

In the current building practice, contractors adopt the “as good as it gets” approach, even in cases where the airtightness level of $0,6 \text{ h}^{-1}$ is imposed. The achievable performance level for a given combination of construction and installation techniques is estimated based on their experience from other cases. There is a lack of knowledge of the relative impact of specific solutions on the overall airtightness, on the cost of airtightness measures and on cost-optimal performance levels.

This paper presents a methodology to predict the airtightness of a building and cost for a given set of installation techniques. The study was conducted according to the principles of the Pareto efficiency. This method allows to evaluate a high number of combination on multiple criteria, e.g. airtightness level and costs (Fonseca, 1995)(Coello,1996). The study was conducted for three types of dwellings, alternately modelled as masonry and wood-frame construction. Optimistic, neutral and pessimistic scenarios for costs and achievable performance have been developed to get an idea on the sensitivity of the methodology. Lastly, the impact of energy use reduction was taken into account in the overall cost by means of the total present value over 30 years.

PARETO-ANALYSIS

Introduction

In previous research, the Pareto-efficiency was used to evaluate the measures for the optimization of extreme low energy dwellings (Verbeeck, 2007). The study was conducted in two phases. Firstly, measures on the building envelope were evaluated. In a second step, the changes in heating, cooling and ventilation devices were compared. According to this research, it is advised to invest first in a high performant building envelope, by means of a high insulation and airtightness level.

A second study (Van Der Veken et al, 2013), was based on the renovation of 5 types of residential dwellings. The analysis takes improvements of the airtightness level in account by replacement of windows and renovation of roofs. E.g. replacing a window could decrease the airtightness level with 1,5 m³/hm² (Van Der Veken et al, 2013). In this paper, a model is constructed to focus more in detail on the airtightness level reachable and the cost of these measures. In this paper, the Pareto-analysis was applied on the residential dwellings used in (Van Der Veken et al, 2013).

Reference buildings and n₅₀-value

Three types of residential buildings were compared: a terraced house, a semi-detached house and a detached house. The buildings were modelled alternately with a traditional construction method and a timber frame construction. Both building methods have a slightly different approach as it comes to airtightness measures. In timber frame constructions, the airtightness of the inside wall surface is created with airtight OSB-panels and airtightness tape. Whereas in the traditional method the inside surface is rendered with plaster. Consequently, no extra measures for airtightness are necessary.

Each reference building is defined by a maximum n₅₀-value, listed in table 1. The n₅₀-value is calculated by summing up the typical air leakage flow through all critical points in a building, e.g. window-wall connections, floor-wall intersections or roof-wall junctions. The values were based on own measurements or data found in literature (Relander, 2009)(SBRCURnet, 2013)(Penne et al, 2012)(Bracke et al, 2014).

Table 1: Maximum n₅₀-value [h⁻¹] of each dwelling in the Pareto-analysis

	Traditional	Timber frame
Terraced house	2,348	2,478
Semi-detached house	2,161	2,317
Detached house	1,795	1,842

In comparison with other estimations methods, these n₅₀-values seem underestimated. E.g. n₅₀-values estimated with other models from ASHRAE, SENVIVV and SBR seems to vary between 0 and 10 h⁻¹ (Van Den Bossche, 2005). Consequently, the Pareto-analysis is conducted with a range of n₅₀-values, characterized by an optimistic, neutral or pessimistic view on air leakage and cost (table 2).

Table 2: Optimistic, neutral and pessimistic view on air leakage rate (n₅₀, table 1) and cost

	Initial Leakage	Cost
Optimistic	2 · n ₅₀	cost _{avg} - σ
Neutral	n ₅₀	cost _{avg}
Pessimistic	0,8 · n ₅₀	cost _{avg} + σ

The cost includes the price of the materials and mounting cost. This was calculated by 7 building contractors and 1 architecture office, resulting in an average price (cost_{avg}) with standard deviation (σ).

Airtightness measures and cost

The initial n₅₀-value (Table 1) of the three buildings can be decreased by improving the airtightness on critical points in the building envelope.

These critical points are:

- Junctions in walls (timber frame construction)
- Junctions in the vapor barrier of a sloped roof
- Connections between floor and wall
- Intersections of the floor, wall and vapor barrier of a sloped roof
- Connections between wall and flat roof (only in terraced house)
- Corners of walls
- Connections between the side edge of the saddle roof and the wall
- Roof-ridge of the sloped roof
- Electric cables through the wall
- Electric cables through the vapor barrier
- Penetrations of ventilation ducts
- Connections between windows/doors and the wall

For each critical point, a number of measures are formulated. The propositions differ in material use and cost. E.g. for the window – wall connection, there are 6 possible measures. These vary from doing no effort (0 €/m), adding foils locally (13,82 €/m), additional reinforcing of the corners in the foils (15,09 €/m) to installing a foil to connect the window frame with the airtight layer (Fig. 1) or the usage of a prefabricated frame around the window filled with polyurethane foam (Fig. 2) or additionally, a combination of a frame and a connection foil (Fig. 3).

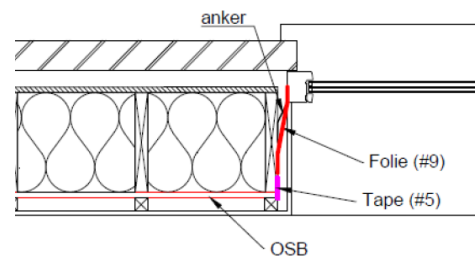


Figure 1: Proposition 4: Airtight foil (folie) to connect the window frame to the airtight layer (OSB). (14,32 €/m)

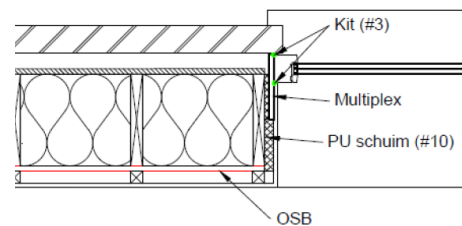


Figure 2: Proposition 5: Prefabricated multiplex frame with PUR insulation (11,52 €/m)

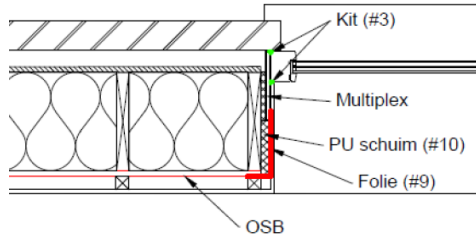


Figure 3: Proposition 6: Prefabricated multiplex frame wit PUR insulation and additional airtight foil to connect the frame to the airtight layer (OSB). (21,43 €/m)

The first step of the Pareto-analysis was thus to find the best combinations of measures on all critical points listed above, in order to find the perfect balance between airtightness level and cost.

Energy cost

In order to select the best Pareto-combination, the Total Present Value was calculated over 30 years for the airtightness investment and compared with the actualized energy use to compensate the heat loss by infiltrating air. This was calculated by estimating the total energy use over one year due to air leakages (Equation 1).

$$\frac{3190,6 \text{ deg reedays}}{\text{year}} \cdot \frac{24 \text{ h}}{\text{day}} \cdot \frac{918,03 \text{ J}}{\text{m}^3 \cdot \text{K}} \cdot \dot{V}_{\text{inf}} = \frac{\text{EnergyUse}}{\text{Year}} \quad (1)$$

In equation 1, the number of degree days is based on data from 2013 (Weerstation Beerse, 2013), while 918,03 J/m³K is the specific heat capacity of air. V_{inf} (m³/h) is calculated from the n₅₀-value [m³/h.m²] with equation 2 and 3. The n₅₀-value was estimated for each building (Table 1).

$$\dot{V}_{50} = \frac{\dot{V}_{50}}{A} \quad [\text{m}^3/\text{h} \cdot \text{m}^2] \quad (2)$$

$$n_{\text{inf}} \approx \frac{n_{50}}{2} \left(\frac{\Delta P}{50}\right)^n \approx \frac{n_{50}}{15} \quad [\text{h}^{-1}] \quad (3)$$

Lastly, the energy cost is also depending on the heating device and fuel used (Table 3). The energy cost is composed of the increase in price (R_e) and the present value factor (F_{pv}). The latter was calculated for a period of 30 years, taken in account an average inflation of 2,85% and an interest of 4% (Statistiek en Economische informatie, 2012). The cost of the heating device itself was not included.

Table 3: Energy cost

	Price (€/kwh)	R _e	F _{pv} (30 years)
Natural gas (>5000 kWh)	0,055	70,5 %	31,89
Oil fuel	0,071	95%	32,28
Wood pellets	0,052	85%	32,13

Results n₅₀ – investment cost

Figure 4 shows the result of the investment cost against the achieved n₅₀-value, for a terraced house with a traditional construction method. The estimations are based on a neutral view (Table 2). With a investment of €5281, the n₅₀-value can be decreased from 2,348 h⁻¹ to 0,306 h⁻¹. An investment of minimum € 3242 is sufficient to reach the passive house level (n₅₀ < 0.6 h⁻¹).

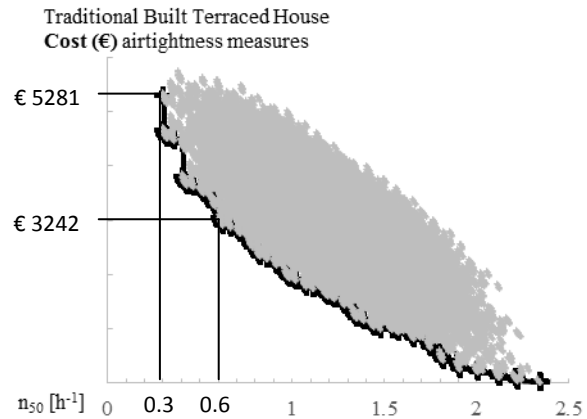


Figure 4: Pareto-Optimum (black line) for a traditional built terrace house, neutral perspective.

When calculating with an optimistic view, the results show a lower investment cost against a higher impact on the n₅₀-value. Whereas executing the Pareto-analysis with a pessimistic view, the cost is much higher against a lower impact on the reached n₅₀-value.

Table 4: Investment cost for minimal n₅₀-values according to the Pareto analysis for a terraced house with traditional construction method.

	Maximum decrease in n ₅₀	Cost
Optimistic	4,696 h ⁻¹ → 0,612 h ⁻¹	€ 3289
Neutral	2,348 h ⁻¹ → 0,306 h ⁻¹	€ 5281
Pessimistic	1,878 h ⁻¹ → 0,245 h ⁻¹	€ 7272

Table 5 compares the investment cost to reach the passive house airtightness level (n₅₀ < 0,6 h⁻¹), viewed from an optimistic, neutral and pessimistic perspective. In general, the investment costs to reach the passive house level do not differ much comparing the three types of houses. The investment cost in a timber frame construction is also slightly more expensive than in a traditional method, except in the case of a terraced house. In the section ‘Discussion’, the advised airtightness measures will be analyzed further.

Table 5: Minimum price to reach $n_{50} < 0,6 \text{ h}^{-1}$ for the three dwellings. *for the traditionally built terraced house, the minimum n_{50} reached was $0,612 \text{ h}^{-1}$

Optimistic	Terraced	Semi-detached	Detached
Traditional	€ 3289*	€ 2901	€ 3167
Timber Frame	€ 2520	€ 3019	€ 3381
Neutral	Terraced	Semi-detached	Detached
Traditional	€ 3242	€ 3244	€ 3611
Timber Frame	€ 2978	€ 3384	€ 3651
Pessimistic	Terraced	Semi-detached	Detached
Traditional	€ 3824	€ 3707	€ 3830
Timber Frame	€ 3800	€ 3919	€ 4509

Results investment cost airtightness – Energy cost

When looking at the total present value (fuel cost + airtightness investment) for a traditional built terraced house, the optimal investment cost for airtightness measures lies between €253 (wood pellets, oil fuel HR-boiler and condensing boiler) and €1921 (Gas boiler) (Figure 5). This investment cost results in a n_{50} -value of $1,915 \text{ h}^{-1}$ and $0,990 \text{ h}^{-1}$ respectively and is calculated from the neutral perspective (Figure 5).

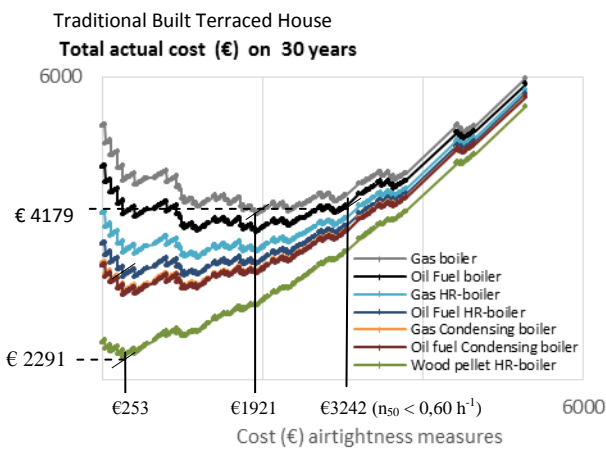


Figure 5: Total present value over 30 year, composed with the fuel cost and total investment cost for airtightness measure. Calculation for a traditional built terrace house, neutral perspective.

At first sight, it seems favorable to invest a low amount in airtightness measures if there is no clear airtightness level imposed. When looking at the larger investment costs for airtightness measures, the total present value rises with the airtightness investment. However, the share of fuel cost decreases in the total cost. E.g. comparing the airtightness investment cost to reach $0,6 \text{ h}^{-1}$ (€ 3242) with the total present value using a gas boiler (€ 4179), the fuel costs over 30 years is € 937. Whereas investing only €1921 in airtightness measures results in a fuel

cost of € 2258 over 30 years (+141%!) to compensate for air leakages only.

DISCUSSION

Which measures are most cost-effective to reach $n_{50} < 0.60 \text{ h}^{-1}$?

Tables A.1 and A.2 in annex give an overview of the most cost-effective measures for a traditional and timber frame construction to reach $n_{50} < 0,6 \text{ h}^{-1}$, for the three types of dwellings. The results are generated with a neutral perspective.

In all cases, the most cost-effective measures (neutral) to reach an n_{50} -level below $0,60 \text{ h}^{-1}$ are (Table A.1 and A.2):

- Saddle roof: Seal the joints of the vapor barrier.
- Wall-Floor-Wall: Airtight foil in the joint and connection with airtightness tape to the plaster rendering/ airtight OSB panels.
- Saddle roof: connect the vapor barrier of the roof surface with a connection foil on the wall.
- Saddle roof: connect the vapor barrier of the roof surface with the roof-ridge, with airtightness tape.
- Ventilation ducts: close openings with poly-urethane foam or a kit.
- Window-wall: Use a multiplex framework around the window and close the gap between frame and wall with poly-urethane foam (Figure 2).

When only considering the total present value over 30 years (fuel cost + investment airtightness measures), the most important measure is closing the penetrations of ventilation ducts through the vapor sealing with PUR-foam. In the case of a traditional built terraced house and the use of gas boiler (Figure 5), the wall-floor connection should be secured with a foil in the joint and the window-wall connection should be executed with a multiplex frame (according to Figure 2). This results in an airtightness level of $n_{50} = 0,990 \text{ h}^{-1}$ at a cost of € 1921.

Price difference in timber frame and traditional terraced houses?

When comparing timber frame constructions with traditional building methods (Table 5), the price differences are very limited. However, there are some differences in airtightness measures. In traditional buildings, there are no measures necessary to close junctions in the wall surface, the penetrations of electrical cables through a wall or an airtight seal. In the model, it is presumed that all traditional buildings have a plaster rendering at the inside surface. Hence, the airtightness layer is automatically created. However, it is not necessary to add reinforcements in the corners of plaster renderings or extra foils in the connection with flat roofs to reach the passive house standard ($n_{50} < 0.60 \text{ h}^{-1}$).

When looking closer at timber frame constructions, it is remarkable that it is not necessary to seal the vertical joints between airtight OSB-panels, nor to use additional foil in the connection between first floor and wall. However, it is advised to reinforce the vertical joints in corners.

Different measures for different housing types?

At first sight, there are small differences in advised measures when comparing the three building types. However, the results in table A.1 and A.2 should be put in perspective. E.g. from table A.2, one can think that a terraced house needs more measures at the floor-wall-roof connection and the connection of the flat roof with the wall, in contrast with the semi-detached and detached house. However, when looking to other combinations in the Pareto-front of the terraced house, it seems possible to reach a n_{50} of 0.637 h^2 when neglecting the wall-floor-roof connection in the terraced house, for a slightly lower investment cost of €2947.

Impact of optimistic and pessimistic view on advised measures?

Table A.3 lists the measures to reach an $n_{50} < 0,60 \text{ h}^{-1}$ for a timber frame constructed terraced house, resulted from a Pareto-analysis with an optimistic, neutral and pessimistic view. As stated before, in the optimistic view the material and mounting cost is lower while the initial n_{50} value was higher, while in a pessimistic view, the investment cost is higher and the initial n_{50} -value is lower. In the optimistic view, there is thus more improvement with less investments possible.

In all three perspectives (Table A.3), for a timber frame terraced house, the most-cost effective measures are:

- Wall-Floor-Wall: Airtightness foil before installing the floor slabs. After installation attach the to the airtight OSB-panels with airtightness tape.
- Wall-Floor-Roof: Airtightness foil before installing the floor slabs. After installation attach the foil to the airtight OSB-panels and vapor barrier of the roof surface with airtightness tape.
- Reinforce the corners of wall panels with airtightness tape.
- Saddle roof: connect the edge of the vapor barrier on the roof surface with the wall surface.
- Saddle roof: connect the vapor barrier with the roof-ridge.
- Ventilation ducts: close openings with polyurethane (PUR) foam or airtight gasket.
- Window-wall: Use a multiplex framework around the window and close the gap between frame and wall with poly-urethane foam (Figure 2).

These are nonetheless the same recommendations as found when comparing all housing and construction types on a neutral basis (table A.1 and A.2).

SUMMARY

This paper presented a methodology to predict the total present value and airtightness level reachable, according to the investment cost for airtightness measurements. Concerning the current guidelines in Belgium for passive house buildings ($n_{50} < 0,60 \text{ h}^{-1}$), the investment cost varies between €2978 for a timber frame terraced house to €3651 for a timber frame detached house, calculated with a neutral perspective.

With equation 1, it is possible to compare the total present value for energy use with the investment cost on airtightness measures. When no specific airtightness level is required, the optimal investment cost for airtightness levels lies between € 253 (wood-pellets, Oil fuel HR-boiler and condensing boiler) and € 1921 (gas boilers), for a traditional build terraced house.

Considering all building types, methods and calculation perspectives, the most cost-effective measures to improve the airtightness to $n_{50} < 0,6 \text{ h}^{-1}$ are concentrated in the connections of the roof and wall, floor and wall and window-wall.

ACKNOWLEDGEMENTS

The authors would like to acknowledge ir.arch. Bert Foré, for the execution of the Pareto Analysis for his master dissertation.

REFERENCES

- Bracke W., Van Den Bossche N., Janssens A. 2014. Airtightness of building penetrations: air sealing solutions, durability effects and measurement uncertainty. 35th AIVC Conference: Ventilation and airtightness in transforming the building stock to high performance. Poznan.Poland
- Coello C.A. 1996. An empirical study of evolutionary techniques for multiobjective optimization in engineering design. PhD Dissertation. Tulane University, New Orleans, LA, USA.
- Fonseca C.M. 1995. An overview of evolutionary algorithms in multiobjective optimisation. In: Evolutionary Computation, No1, pp 1-16.
- Penne A., Vandeweerd R. 2012. Luchtdichtheid van raamaansluitingen in houtskeletbouw. Master Dissertation. KAHO Sint-Lieven. Ghent
- Relander T.O.2009. Paper 1: Air Tightness and Air Leakages of Norwegian Wood-Frame Houses in Airtightness of wood-frame houses. PhD

dissertation. Norwegian University of Science and Technology, Norway.

SBRCURnet.2013.Luchtdicht bouwen. Theorie-Ontwerp-Praktijk.Rotterdam.The Netherlands.

Statistiek en Economische informatie.2013. Inflatie. Algemene Directie Statistiek en Economische Informatie. Brussels. Belgium.

Van Den Bossche N. 2005. Luchtdichtheid: Experimenteel onderzoek naar schattingsmethodes bij woningen. Master Dissertation, Ghent University. Ghent.

Van der Veken J., Creylman J. Lenaerts T. 2013. Studie naar kostenoptimale niveaus van de minimumeisen inzake energieprestaties van gerenoveerde bestaande residentiële gebouwen. Kenniscentrum Energie. Geel. Belgium

Verbeeck G. 2007. Optimisation of extremely low energy residential buildings. PhD dissertation. KU Leuven, Belgium.

Vlaams Energie Agentschap. 2011. EPB-cijfers en statistiek voor EPB-aangiften ingediend t.e.m. 31/12/2015, Vlaams Energieagentschap, Brussels, Belgium.

Weerstation Beerse. 2014. Dagelijke Graaddagen 2013.

Wouters P., Loncour X., Vandaele L., Janssens A., De Paepe M., Roels S., Honoré R. and Carrié R. 2012. Onderzoek naar een draagvlak voor het invoeren van minimale luchtdichtheidseisen: Eindverslag [in dutch]. No.December, pp. 1-57.

WTCB.2012.Luchtdichtheid van gebouwen: een grote uitdaging voor alle bouwberoepen.WTCB contact. Nr. 33, 9de jaargang. Brussels. Belgium

ANNEX

Table A.1:

Most cost-effective measures to reach $n_{50} < 0,6 \text{ h}^{-1}$ for the three dwelling with a traditional constructions method.

NEUTRAL - TRADITIONAL	TERRACED HOUSE	SEMI-DETACHED	DETACHED HOUSE
n_{50}	0,591 h⁻¹	0,597 h⁻¹	0,599 h⁻¹
Cost	€ 3242	€ 3244	€ 3611
Wall surface (plaster rendering)	No measures	No measures	No measures
Roof surface	Sealing joints of the vapor barrier	Vapor barrier without sealing	Sealing joints of the vapor barrier
Bottom Floor-Wall	Airtight foil in the joint and connection with airtightness tape to the plaster rendering	Airtight foil in the joint and connection with airtightness tape to the plaster rendering	No measures
Wall-Floor-Wall	Airtightness foil before installing the floor slabs. After installation attach the foil to the plaster rendering with airtightness tape.	Airtightness foil before installing the floor slabs. After installation attach the foil to the plaster rendering with airtightness tape.	Combination of airtightness foil (top surface floor) and joint strip (bottom surface floor)
Wall-Floor-Roof	Combination of airtightness foil (top surface floor) and joint strip (bottom surface floor)	Combination of airtightness foil (top surface floor) and joint strip (bottom surface floor)	No measures
Vertical joint-corner	No measures	No measures	No measures
Flat roof	No measures		
Saddle roof: side edge of roof surface –wall surface	Connecting airtightness foil of the roof surface with a connection foil on the wall	Connecting airtightness foil of the roof surface with a connection foil on the wall	Connecting airtightness foil of the roof surface with a connection foil on the wall
Saddle roof: roof-ridge and surface	Airtightness foil is connected to the roof-	Airtightness foil is connected to the roof-	Airtightness foil is connected to the roof-

	ridge with airtightness tape	ridge with airtightness tape	ridge with airtightness tape
Electric cables	No measures	No measures	No measures
Electric cables through airtight seal	No measures	Airtight gasket	No measures
Ventilation ducts	Closing with kit or PUR foam	Airtight gasket	Closing with kit or PUR foam
Window-Wall	Multiplex framework and closing with PUR-foam (Figure 2)	Multiplex framework and closing with PUR-foam (Figure 2)	Multiplex framework and closing with PUR-foam (Figure 2)

Table A.2:
Most cost-effective measures to reach $n_{50} < 0,6 h^{-1}$ for the three dwelling with a timber frame constructions method.

NEUTRAL - TIMBER FRAME	TERRACED HOUSE	SEMI-DETACHED	DETACHED HOUSE
n_{50}	0,598 h⁻¹	0,595 h⁻¹	0,594 h⁻¹
Cost	€ 2978	€ 3384	€ 3651
Wall surface	OSB joints untaped	OSB joints untaped	OSB joints untaped
Roof surface	Sealing joints of the vapor barrier	Sealing joints of the vapor barrier	Sealing joints of the vapor barrier
Bottom Floor-Wall	No measures	No measures	No measures
Wall-Floor-Wall	Airtightness foil before installing the floor slabs. After installation attach the foil to the airtight OSB-panels with airtightness tape.	Airtightness foil before installing the floor slabs, after installation attach the foil to the airtight OSB-panels with airtightness tape.	Airtightness foil before installing the floor slabs, after installation attach the foil to the airtight OSB-panels with airtightness tape.
Wall-Floor-Roof	Airtightness foil before installing the floor slabs. After installation attach the foil to airtight OSB-panels and vapor barrier of the roof surface with airtightness tape	No measures	No measures
Vertical joint-corner	Airtightness tape (Hg2)	Airtightness tape (Hg2)	Airtightness tape (Hg2)
Flat roof	Airtightness foil attached on the wall before installing the roof frame. After installation, folding the foil around the roof frame and tape to the vapor barrier on the roof surface		
Saddle roof: edge of roof surface –wall surface	Airtightness tape to connect the vapor barrier of the roof surface with the airtight OSB-panels of the wall	Airtightness tape to connect the vapor barrier of the roof surface with the airtight OSB-panels of the wall	Airtightness tape to connect the vapor barrier of the roof surface with the airtight OSB-panels of the wall
Saddle roof: roof-ridge and surface	Airtightness foil is connected to the roof-ridge with airtightness tape	Airtightness foil is connected to the roof-ridge with airtightness tape	Airtightness foil is connected to the roof-ridge with airtightness tape
Electric cables through wall	No measures	Closing with kit or PUR foam	No measures
Ventilation ducts	Closing with kit or PUR foam	Closing with kit or PUR foam	Closing with kit or PUR foam

Window-Wall	Multiplex framework and closing with PUR-foam (Figure 2)	Multiplex framework and closing with PUR-foam (Figure 2)	Multiplex framework and closing with PUR-foam (Figure 2)
-------------	--	--	--

Table A.3:

Most cost-effective measures to reach $n_{50} < 0,6 h^{-1}$ for the terraced house with a timber frame construction, view from the optimistic, neutral and pessimistic perspective.

TERRACED HOUSE-TIMBER FRAME	OPTIMISTIC € 2520	NEUTRAL € 2978	PESSIMISTIC € 3800
Wall surface	Taped OSB joints	OSB joints untaped	OSB joints untaped
Roof surface	Sealing joints of the vapor barrier	Sealing joints of the vapor barrier	Sealing joints of the vapor barrier
Bottom Floor-Wall	Airtight foil in the joint and connection with airtightness tape to the airtight OSB-panel	No measures	No measures
Wall-Floor-Wall	Airtightness foil before installing the floor slabs. After installation attach the to the airtight OSB-panels with airtightness tape.	Airtightness foil before installing the floor slabs, After installation attach the foil to the airtight OSB-panels with airtightness tape.	Airtightness foil before installing the floor slabs. After installation attach the foil to the airtight OSB-panels with airtightness tape.
Wall-Floor-Roof	Airtightness foil before installing the floor slabs. After installation attach the foil to the airtight OSB-panels and vapor barrier of the roof surface with airtightness tape.	Airtightness foil before installing the floor slabs. After installation attach the foil to the airtight OSB-panels and vapor barrier of the roof surface with airtightness tape.	Airtightness foil before installing the floor slabs. After installation attach the foil to the airtight OSB-panels and vapor barrier of the roof surface with airtightness tape.
Vertical joint-corner	Airtightness tape	Airtightness tape	Airtightness tape
Flat roof	Airtightness foil attached on the wall before installing the roof frame. After installation, folding the foil around the roof frame and tape to the vapor barrier on the roof surface.	Airtightness foil attached on the wall before installing the roof frame. After installation, folding the foil around the roof frame and tape to the vapor barrier on the roof surface	No measures
Saddle roof: edge of roof surface –wall surface	Airtightness tape to connect the vapor barrier of the roof surface with the airtight panels of the wall.	Airtightness tape to connect the vapor barrier of the roof surface with the airtight panels of the wall.	Airtightness tape to connect the vapor barrier of the roof surface with the airtight panels of the wall.
Saddle roof: roof-ridge and surface	Airtightness foil is connected to the roof-ridge with airtightness tape.	Airtightness foil is connected to the roof-ridge with airtightness tape.	Airtightness foil is connected to the roof-ridge with airtightness tape.
Electric cables through wall	Closing with kit or PUR foam	No measures	No measures
Ventilation ducts	Airtight gasket (difference with PUR is very small)	Closing with kit or PUR foam	Airtight gasket
Window-Wall	Multiplex framework and closing with PUR-foam (Figure 2)	Multiplex framework and closing with PUR-foam (Figure 2)	Multiplex framework and closing with PUR-foam (Figure 2)

Salt damage of the stone Buddha carved into the cliff

N. Takatori¹, D. Ogura¹, S. Wakiya², M. Abuku³, K. Kiriya⁴, Y. Kohdzuma²

¹ Department of Architecture and Architectural Engineering, Kyoto University, Kyoto, Japan

² National Institutes for Cultural Heritage Nara National Research Institute for Cultural Properties, Nara, Japan

³ Faculty of Architecture, Kindai University, Osaka, Japan

⁴ Graduate School of Advanced Integrated Studies in Human Survivability, Kyoto University, Kyoto, Japan

ABSTRACT

Motomachi Sekibutsu is the stone Buddha carved into the cliff in Oita city, Japan. It is difficult for Motomachi Sekibutsu to prevent heat and moisture transfer through the cliff behind the statue. Therefore, various degradations have been in progress. In this paper, we focus on the salt damage which is one of the biggest problems in Motomachi Sekibutsu. Assuming that salt damage by Na_2SO_4 can be estimated by the temperature and humidity in and around the Buddha statue, we investigate the influence of the current surrounding environment on the salt damage in Motomachi Sekibutsu by numerical analysis of heat and moisture transfer.

1. INTRODUCTION

Motomachi Sekibutsu is the stone Buddha carved into the cliff in Oita city, Japan in the 11th–12th century, and has been designated as a national historic site in 1934. Motomachi Sekibutsu is always affected by the heat and moisture transfer through a cliff because it cannot be separated from the cliff. Therefore, at Motomachi Sekibutsu, various preservation measures have been taken: main measures are constructing a shelter to intercept wind and rain and boring a tunnel behind Motomachi Sekibutsu to reduce the ground water level. However, the main factor of degradation, salt damage, has still not been prevented [1].

Our ultimate aim is to suppress degradation from salt damage by rebuilding the shelter covering the Buddha statue and controlling the room environment. In this paper, we focus on the Buddha of healing, which is located at the center of Motomachi Sekibutsu and has been affected by salt damage, and we investigate the heat and moisture behavior and clarify the mechanism of the progress of salt damage of each part of the Buddha statue by numerical analysis of the heat and moisture transfer.

2. SALT DAMAGE

2.1 Mechanism

Salt damage is considered to be due to salt precipitated in the porous material and salt destroys the porous body when the salt is exposed to a thermal expansion and hydration [2]. Salt that has been



Figure 1: The Buddha of healing



Figure 2: The exterior of the shelter

observed at Motomachi Sekibutsu is primarily sodium sulfate (Na_2SO_4) and calcium sulfate (CaSO_4) [3]. Among them, it is believed that Na_2SO_4 is a particularly destructive salt, and the destruction mechanism of the porous material with Na_2SO_4 is considered to be caused by the the pressure when the

state of Na_2SO_4 changes from anhydrate (thenardite) to decahydrate (mirabilite) [4].

2.2 Relationship of salt damage and temperature and humidity

It is believed that salt damage caused by Na_2SO_4 occurs under the process of Na_2SO_4 changing from thenardite to mirabilite. In this paper, assuming that the state of Na_2SO_4 is determined by the temperature and humidity at each regions of the Buddha statue in which Na_2SO_4 accumulates [5], we can estimate whether salt damage occurs by analyzing the temperature and humidity in the Buddha statue. In this paper, we examine the influence of heat and moisture transfer on salt damage, although salt is assumed to present uniformly in the material. Using this approach, we plot the annual calculated temperature and humidity variations on the phase diagram of Na_2SO_4 . And then, we investigate the progress of salt damage.

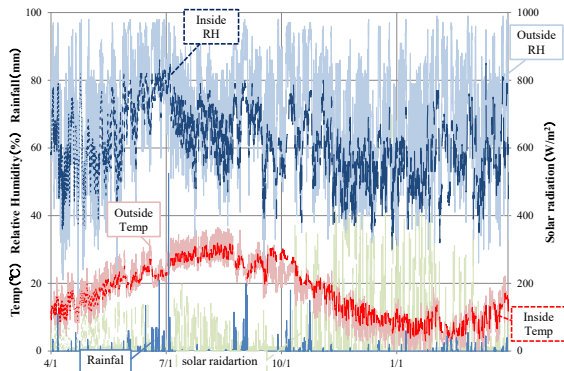


Figure 3: Outdoor and indoor climate from April 2013 to March 2014

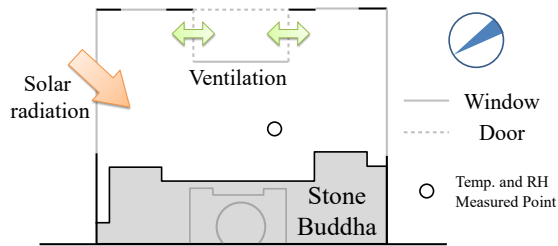


Figure 4: Plan of Motomachi Sekibutsu

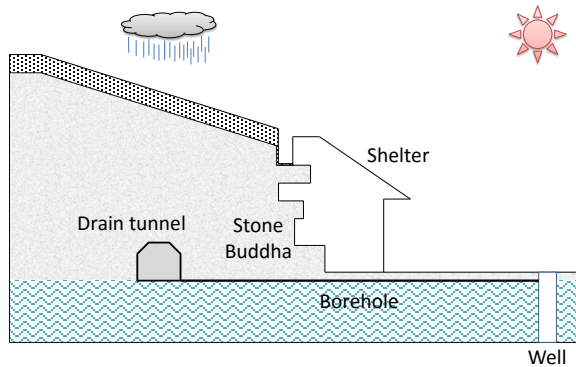


Figure 5: Section of Motomachi Sekibutsu

3. SURROUNDING ENVIRONMENT

Even after Motomachi Sekibutsu had been covered with a wooden shelter: about 7m wide, 5m long, and 3.5m high, the statue has been suffering from the influence of the surrounding environment, including heat transmission by the roof and walls, ventilation into the front door, solar radiation transmission into windows, and rainfall penetration into the cliff behind the statue.

Fig.3 shows the measured outside and inside temperature and humidity for one year from April 2013. It demonstrates the effect of the shelter that the fluctuations of the indoor temperature and humidity are smaller than those of the outdoor throughout the year. In addition, solar radiation through the windows of the shelter is incident on the stone Buddha from time to time. It varies by time and the season depending on the shape and location of the windows (Fig.4). Further, the shelter of Motomachi Sekibutsu has two doors at the front entrance. Ventilation could occur by opening those doors.

The cliff where Motomachi Sekibutsu is carved consists of two layers, tuff and soil. The soil deposits on the tuff layer and the cliff top is covered with trees. In turn, The drain tunnel behind Motomachi Sekibutsu and slightly-sloped holes were bored in 1998 to 1990 in order to drain ground water below the ground as shown in Fig. 5. This is considered to have an effect of reducing the ground water level to approximately 1 m below the ground level.

4. NUMERICAL ANALYSIS

4.1 Methodology

We show the method for a numerical analysis to solve the heat and moisture behavior in the stone Buddha including a cliff. The heat and moisture balance equations for porous materials are respectively written by [6]

$$c\rho \frac{\partial T}{\partial t} = \nabla \cdot \{(\lambda + r\lambda'_{Tg})\nabla T\} + \nabla \cdot (r\lambda'_{\mu g}\nabla \mu) \quad (1)$$

$$\rho_w \left(\frac{\partial \psi}{\partial \mu}\right) \frac{\partial \mu}{\partial t} = \nabla \cdot [\lambda'_{\mu}(\nabla \mu - n_x g)] + \nabla \cdot (\lambda'_T \nabla T) \quad (2)$$

where the relation between the chemical potential of water μ and the relative humidity h is given by

$$\mu = R_v T \ln h. \quad (3)$$

The boundary conditions for heat and moisture are:

$$\alpha(T_0 - T_i) + r\alpha'_m(p_0 - p_i) + q_s = -(\lambda + r\lambda'_{Tg}) \frac{\partial T}{\partial n} - r\lambda'_{\mu g} \frac{\partial \mu}{\partial n} \quad (4)$$

$$\alpha'_m(p_0 - p_i) + J_p = -\lambda'_{\mu} \left(\frac{\partial \mu}{\partial n} - n_x g\right) - \lambda'_T \frac{\partial T}{\partial n} \quad (5)$$

Table 1 Calculation condition

	Indoor temp. and R.H. of the shelter	Outside temp. and R.H. of the shelter	Amount of solar radiation	Amount of rainfall
Case1	Constant ⁽¹⁾	Constant ⁽¹⁾	0	0
Case2	Measured value(inside) ⁽²⁾	Measured value(outside) ⁽²⁾	Estimated value ⁽³⁾	Measured value ⁽²⁾
Case3	Measured value(outside) ⁽²⁾	Measured value(outside) ⁽²⁾	Estimated value ⁽³⁾	Measured value ⁽²⁾

4.2 Conditions

In this study, we analyze the two-dimensional vertical section of the cliff. The analysis model is the cliff containing the stone Buddha shown in Fig. 6. Heat and moisture physical properties of the soil is decided in reference to the paper of Li et al. [7], and the properties of the tuff are estimated by referring to the literature data [7][8][9]. Fig.8,9,10,11 show the moisture retention curve of the soil and tuff, thermal conductivity of those, moisture conductivity of the tuff, and moisture conductivity of the soil, respectively. The coefficient of heat transfer is used as 9.3 W/m²K for the inside of the shelter and 23.3 W/m²K for the outside and the coefficient of moisture transfer is calculated by using the Lewis relationship. In this analysis, we use the explicit finite-difference method for numerical analysis.

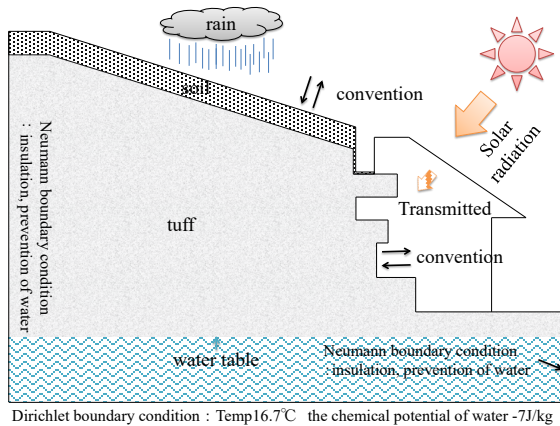


Figure 6: Schematic diagram of the analysis model

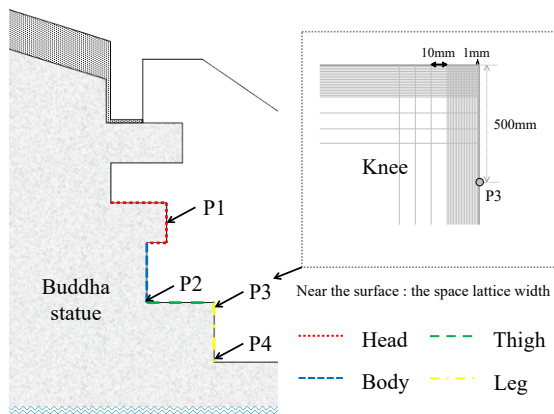


Figure 7: Analysis position

Table 1 shows the room conditions used in the analysis. First, we compare the measured and the calculated temperature at the surface of the stone Buddha. Next, we conducted a steady state analysis, namely Case 1, in order to clarify the influence of the heat and moisture behavior in the stone Buddha given by the shape of the statue and the ground water. In Case 1, we figure out the average heat and moisture behavior by using the annual average room temperature and humidity from April, 2013 to March, 2014. Then, we performed a periodic steady state analysis considering the annual fluctuation of the inside and outside conditions, including the solar radiation and rainfall so as to clarify the effects of the seasonal transition of the boundary condition on the heat and moisture behavior. In Case 3, we suppose the situation that the ventilation rate is so large as the room temperature and humidity match to the values of the outside.

Three other important conditions for the analysis are described below.

(1) In Case 1, the inside and outside temperature and relative humidity are the constant values which are the annual average value of the room condition: temperature (temp.) is 17.7°C relative humidity (R.H.) is 69%

(2) In Case 2 and Case 3, the inside temperature and relative humidity measured in the shelter [10] and the outside temperature, relative humidity and horizontal rainfall intensity measured by Japan Meteorological Agency in Oita city [11] are used for April 2013 to March 2014. Half of the measured horizontal rainfall intensity is imposed on the top of cliff, taken into account blocking effects by trees.

(3) The radiation is calculated by converting the measured global solar radiation into the direct solar and diffuse radiation considering the shape of the roof, the transmittance of the windows and the solar azimuth and the altitude. The solar radiation at the exterior surface of the roof is take at 0 as trees cover the shelter.

Fig.12 shows the intensity of solar radiation which is incident on various parts of the Buddha statue [12]. The Dirichlet boundary condition is applied to the bottom of the ground: the temperature is 16.7 °C at 12.2 m below the ground level and the chemical potential of water is - 7 J/kg with the ground water level of 1.1 m below the ground level. The Neumann boundary condition is applied to the vertical

boundaries in the ground: no heat and moisture flux is taken into account.

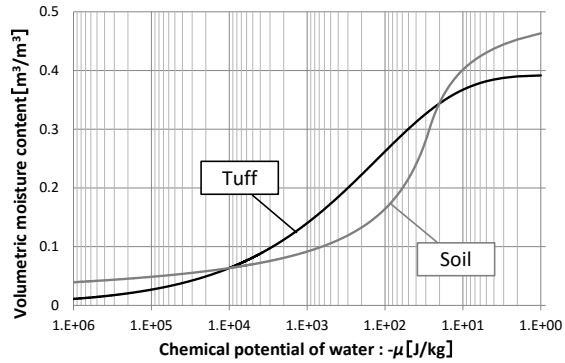


Figure 8: Moisture retention curve

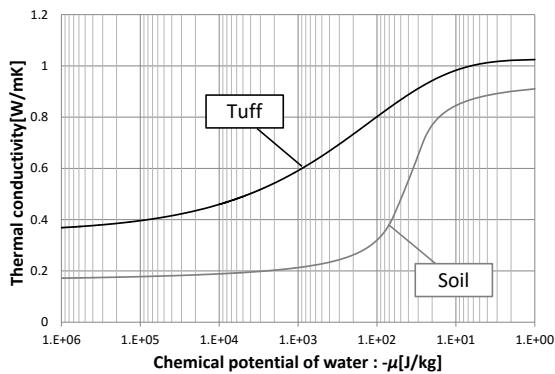


Figure 9: Thermal conductivity

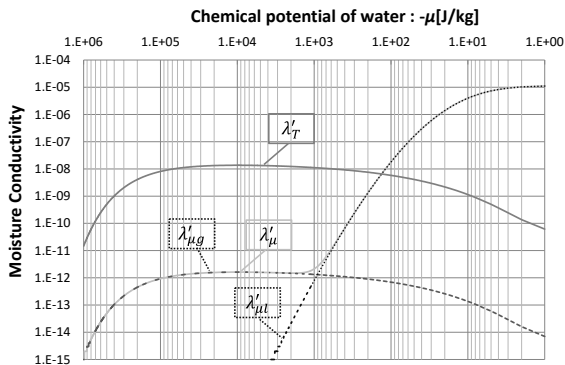


Figure 10: Moisture conductivity of the tuff

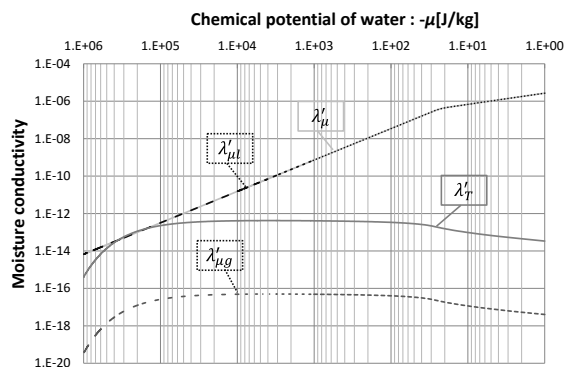


Figure 11: Moisture conductivity of the soil

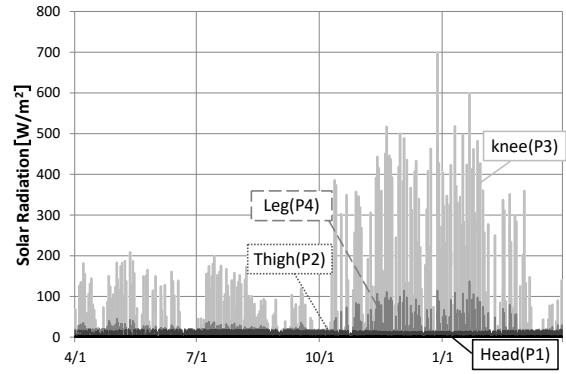


Figure 12: Annual variation of the solar radiation incident on each part of the Buddha statue

5. RESULTS AND DISCUSSION

5.1 Comparison of the measured value and analyzed value

Fig. 13 shows the comparison of the measured and analyzed values of the temperature and relative humidity at the surface for Case 2. The daily fluctuations of the analyzed values sometimes do not correspond to those of the measurement. However, the annual variations of the analyzed values are correspondent with those of the measurement. This error is considered to be mainly attributable to the reproducibility of the intensity of solar radiation in the analysis.

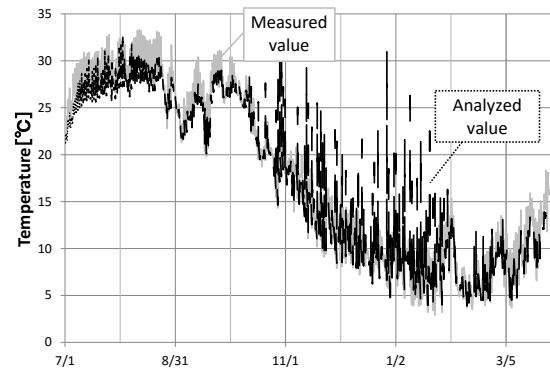


Figure 13: The simulated and measured temperatures

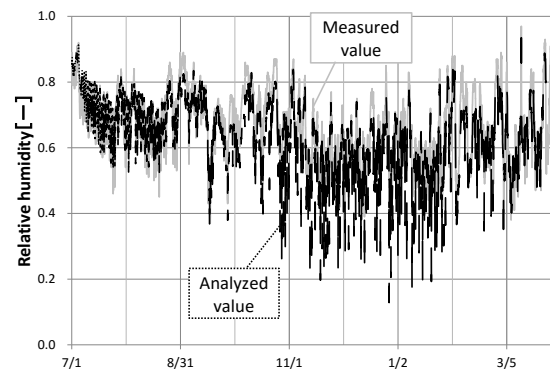


Figure 14: The simulated and measured relative humidities

5.2 The influence of the ground water and the shape of the statue

Motomachi Sekibutsu is strongly affected by the ground water because the distance from the ground water level to the ground level is very close (about 1 m). Also, heat and moisture behavior would depend on the complicated geometry of the Buddha statue. In this section, we examine the effect of heat and moisture behavior in the Buddha statue by using the results of the steady state analysis, e.g. Case 1.

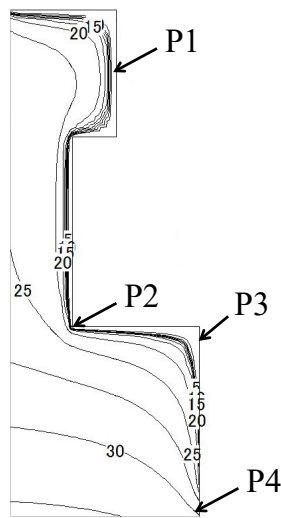


Figure 15: Moisture content distribution in the Buddha statue

Fig. 15 shows the moisture content distribution in the Buddha statue. It can be seen that due to the influence of the ground water, the moisture content is high in the deep area and reduces near the surface of the statue. It is also seen that the moisture content depends on locations due to the geometry effect. The moisture content of the head and knee which are convex to the air is low not only near the surface but also in the deep area. On the other hand, that of the abdomen which is at the corner of the body is low near the surface although it is still high in the deep area.

Fig. 16 shows the temperature, moisture content and the amount of evaporation at the surface of the statue for Case1. The position corresponding to Fig. 16 is shown in Fig. 7. Similar to the results in Fig. 15, the water content near the surface is low from the head to the leg except for the foot (P4). In the field survey, bryophytes were observed below the knee and/or at the recessed site of the body, so it is considered that the moisture content is high at these locations.

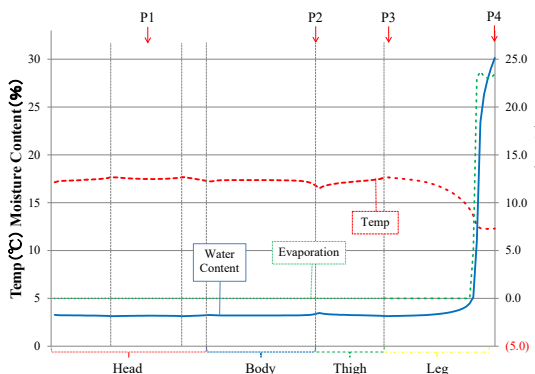


Figure 16: Temperature and moisture content profile on the surface of Buddha statue

5.3 The annual fluctuation of the water content

In the following, we will examine the influence on the heat and moisture behavior in the Buddha statue of the annual fluctuation of the room temperature and humidity, the solar radiation, and the ventilation. Fig. 17 shows the annual fluctuation of the moisture content at each regions of the statue. It tends to be low water content on the all regions throughout the year except for P4 as well as in Section 5.2.

In Fig. 17, it can be seen that the moisture content at the each part becomes higher from June to early July when the relative humidity in the room becomes high. In particular, at P2 and P4, the moisture content increases from June to July and reduces from October to December significantly.

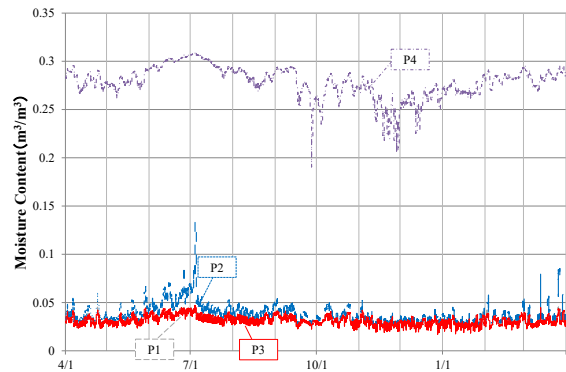


Figure 17: Annual distribution of water content on the respective parts

5.4 Effect of heat and moisture fluctuations on potential Na₂SO₄ phase changes

In the saturated salt concentration, the sodium sulfate (Na₂SO₄) would take three states depending on the temperature and humidity: solute, decahydrate (mirabilite) or anhydrous hydrate (thenardite). In this section, assuming that the salt concentration of the solution in the material is saturated, we check the phase of salt based on the fluctuation of the temperature and humidity. In the following, we focus on the knee, i.e. position P3, where salt damage is in progress, and examine the phase-change process of Na₂SO₄. Figs. 18 and 19 show the results obtained by superimposing the calculated annual temperature and relative humidity values on the phase diagram of Na₂SO₄ at the surface of the knee and at the depth of 3 mm from P3 in the horizontal direction, respectively. First, we explain the relationship the state of Na₂SO₄ and the temperature and humidity. Na₂SO₄ changes from thenardite to mirabilite as the relative humidity rises. When the humidity increases further, Na₂SO₄ deliquesces. The salt tends to become mirabilite at a lower temperature and thenardite at a higher temperature.

In Fig. 17, at P3, the relative humidity is low throughout the year and Na₂SO₄ remains to be thenardite because the water content is low as shown in Fig. 18. However, when the relative humidity rises,

thenardite sometimes changes to mirabilite. On the other hand, the relative humidity is higher at the depth of 3 mm from P3 than the surface of P3 as seen in Fig. 19, and thenardite changes to mirabilite more frequently. In particular, the relative humidity rises from winter to spring, so that salt damage is likely to occur during this period.

Fig. 20 shows the results obtained by superimposing the calculated annual temperature and relative humidity on the phase diagram of Na_2SO_4 for Case 3. Compared to Case 2, the fluctuation of temperature and humidity is larger and changes from thenardite to mirabilite occurs more frequently. Based on the above-mentioned discussion, it is suggested that ventilation should be reduced to mitigate the currently observed salt damage.

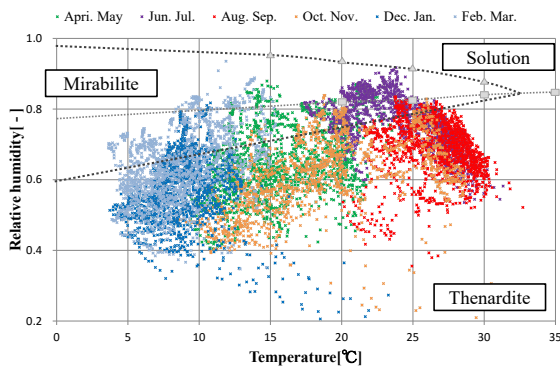


Figure 18: The temperature and relative humidity on the phase diagram at P3

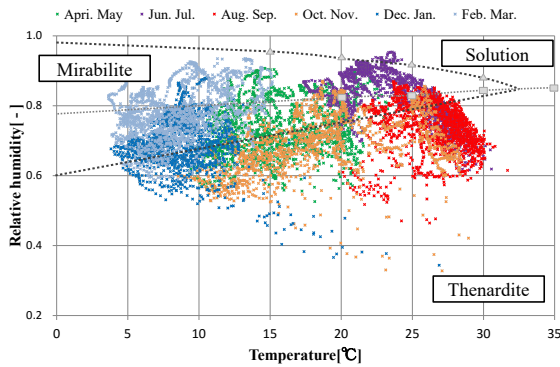


Figure 19: The temperature and relative humidity on the phase diagram at the depth of 3mm from P3

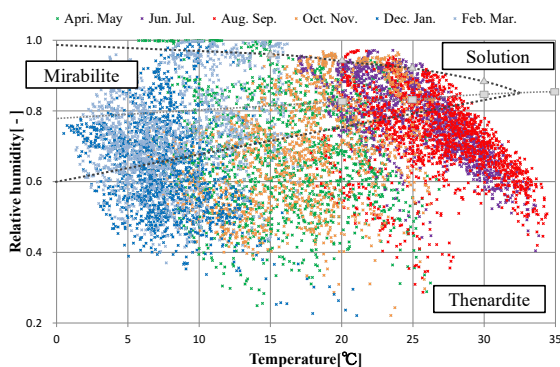


Figure 20: The temperature and relative humidity on the phase diagram at P3 (Case 3)

6. CONCLUSION

In this paper, we focus on Motomachi Sekibutsu, which is the stone Buddha carved into the cliff in Oita city, Japan, and developed a two-dimensional model for coupled heat and moisture transfer and calculated the heat and moisture behavior in and around the Buddha statue of healing. Assuming that the salt concentration of the solution in the pores is saturated and the state of Na_2SO_4 is determined by the temperature and humidity, we evaluate the progress of salt damage by the fluctuation of the temperature and humidity and the change of the state of Na_2SO_4 . Main results are as follows.

- 1) In Motomachi Sekibutsu, the ground water is so high that the water content is high in the depth of the statue, but can decrease near the surface of some locations. In particular, the moisture content is lower in the external corner than in the internal corner.
- 2) Thenardite changes to mirabilite more frequently in the depth of 3mm from the surface than at the surface.
- 3) More serious salt damage caused by the phase change of Na_2SO_4 would occur when the ventilation rate of the shelter is increased.

ACKNOWLEDGEMENT

We are grateful to the Oita city board of education including Shiro Kawano for providing the various measurement data and other records. This work was supported by the PRESERVATION RESEARCH GROUP OF STONE HERITAGE and the JSPS KAKENHI Grant Number 26709043.

APPENDIX A

In this analysis, the evaporation is calculated by the water content and the liquid water flux at each point.

The amount of evaporation:

$$W = -\left(\frac{\partial \rho_w \phi}{\partial t} + \nabla J_{2w}\right) \quad (6)$$

The liquid water flux:

$$J_{2w} = -\lambda'_{ul} \left(\frac{\partial \mu}{\partial n} - n_x g\right) - \lambda'_{Tl} \frac{\partial T}{\partial n} \quad (7)$$

APPENDIX B

The solar radiation incident on the Buddha of healing is estimated in the following manner. We calculate the temporal period in which solar radiation is incident to the Buddha statue, taking into account the position of the sun, the shape of the eaves and the opening of the roof. The direct solar and diffuse radiation are derived from the global solar radiation measured at Oita city weather stations by using both Bouguer's and Berlage's formulae and the atmospheric transmittance [14]. By taking into

account the transmission rate of the glass and the orientation of the statue, we calculate the solar radiation incident on the statue. In this paper, the transmittance rate is taken at 0.75 for the front entrance and 0.4 for the side window. Fig. 22 compares the estimated value with the measured value for November 7, 2014. The estimated value is sufficiently accurate.

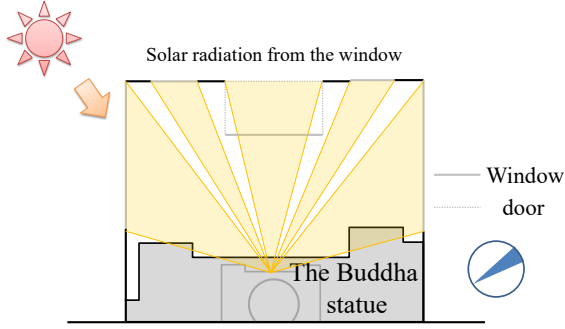


Figure 21 Solar radiation

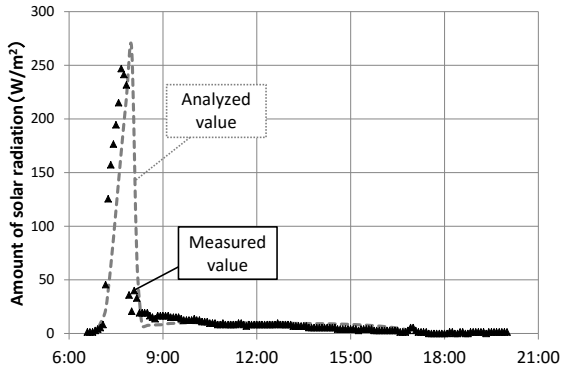


Figure 22 The measured and analyzed radiation incident on the statue

APPENDIX C

The equilibrium moisture content of tuff is determined by the following formula based on [8].

$$\psi(\mu) = \psi_{Max} - (\psi_{Max} - \psi_{Min}) \left(A^{B \log_{10} -\mu} \right) \quad (8)$$

where $\psi_{Max} = 0.392$, $\psi_{Min} = 0$, $A=0.001$, and $B=0.4$. Also, the water conductivity of tuff is referred to the literature values [7] which is summarized and expressed using the following formulae.

$$\lambda'_{ul} = K_{sat} \left(\frac{\rho_w}{g} \right) \left(\frac{\psi}{\psi_{sat}} \right)^n \quad (9)$$

$$\lambda'_{ug} = \lambda'_p \left(\frac{\partial p}{\partial \mu} \right) \times \frac{\psi_{max} - \psi + 0.001}{\psi_{max}} \quad (10)$$

where K_{sat} is $1.10 \times 10^{-7} [m/s]$ by referring to the experiments with specimens taken from the boring survey [9], λ'_p is 1.2×10^{-10} , and n is 15.

SYMBOLS

c : specific heat [J/kgK]

ρ : density [kg/m^3]

ρ_w : density of liquid water [kg/m^3]

g : gravitational acceleration [m/s^2]

t : time [s]

T : temperature [K]

p : water vapor pressure [Pa]

ψ : volumetric moisture content [m^3/m^3]

μ : chemical potential of water [J/kg]

h : relative humidity [-]

r : heat of phase change from vapor to liquid water [J/kg]

α : overall heat transfer coefficient [$W/(m^2 \cdot K)$]

α'_m : water vapor transfer coefficient [$kg/(m^2 \cdot s \cdot Pa)$]

λ : thermal conductivity [$W/(m \cdot K)$]

λ'_T : moisture conductivity related to temperature [$kg/(m \cdot s \cdot K)$]

λ'_{Tg} : vapor conductivity related to the temperature [$kg/(m \cdot s \cdot K)$]

λ'_μ : moisture conductivity related to the chemical potential gradient of water [$kg/(m \cdot s \cdot (J/kg))$]

$\lambda'_{\mu g}$: vapor conductivity related to the chemical potential gradient of water [$kg/(m \cdot s \cdot (J/kg))$]

$\lambda'_{\mu l}$: liquid conductivity related to the chemical potential gradient of water [$kg/(m \cdot s \cdot (J/kg))$]

n_x : unit vector vertically downward [-]. The vector is 1 for the vertically downward direction and 0 for the horizontal direction.

W : evaporation rate per unit volume [$kg/(m^3 \cdot s)$]

q_s : absorbed amount of solar radiation [W/m^2]

J_p : rainfall intensity [$kg/(m^2 \cdot s)$]

J_{2w} : liquid water flux [$kg/(m^2 \cdot s)$]

K_{sat} : saturated permeability [m/s]

REFERENCES

- [1] Oita city board of education. 1996. Kunishiteishiseki Oita Motomachi Sekibutsu Hozonsyurijigyo Hokokusho (in Japanese), Oita, Sohrinsha, 71p.
- [2] Y. Matsukura. 2008. Chikei Henka No Kagaku (in Japanese), Asakura Publishing, pp.19-23
- [3] K. Kiriya, S. Wakiya, N. Takatori, D. Ogura, M. Abuku, Y. Kohzuma. 2015. The Current State the Factors of Salt Deterioration at Buddha Statue Carved into a Cliff at Motomachi, in: Proceedings of the 32th annual meeting of Japan Society for Scientific Studies on Cultural Properties, p.81
- [4] A.S. Goudie, H.A. Viles. 1997. Salt weathering hazards, Wiley, pp.106-107
- [5] R. J. Flatt. 2002. Salt damage in porous materials: how high supersaturations are generated, Journal of Crystal Growth, pp.435-454

- [6] M. Matsumoto. 1984. Shin Kenchikugaku Taikei, 10, Kankyo Butsuri (in Japanese), Shokokusya, pp.105-134
- [7] Y. Li, D. Ogura, S. Hokoi, T. Ishizaki. 2010. Effects of excavation and emergency preservation measures after excavation on hygrothermal behavior in stone chamber of Takamatsuzuka tumulus, Journal of Environmental Engineering, 658, pp.1041-1050
- [8] M. Khalil, T. Ishizaki. 2008. Moisture characteristic curves of tuff breccia stone, Science for Conservation, 47, pp.11-19
- [9] Oita city board of education, 1986, Oita Motomachi Sekibutsu Chisitsu Chousa Itaku Hokokusho (in Japanese), 26p.
- [10] Oita city board of education. 2014. Oita Motomachi Sekibutsu Heisei 25 nendo Chosa Gyomu Itaku Hokokusho (in Japanese), 137p.
- [11] Japan Meteorological Agency. 2014. <<http://www.jma.go.jp/jma/index.html>> [Accessed at November 27, 2014]
- [12] N. Takatori, D. Ogura, S. Wakiya, M. Abuku, K. Kiriya. 2015. Study on preservation of a carved Buddhist at Motomachi – Investigation of the influence of salt damage with the environment in covered roof -, in: Proceedings of the 55th annual meeting of the Kinki Branch of Architectural Institute of Japan, pp.133-137 (in Japanese)

COMPARISON OF FROST DAMAGE INDEXES FOR TWO DIFFERENT WEATHER YEARS IN THE CZECH REPUBLIC

J. Kočí, J. Maděra, R. Černý

Department of Materials Engineering and Chemistry, Faculty of Civil Engineering, Czech Technical University in Prague, Thákurova 7, Prague, Czech Republic

ABSTRACT

This paper follows up a previous work aimed at generation of a critical weather year for hygrothermal simulations using partial weather data sets. Since only the demonstration of the method without the verification was provided in the original research paper, the objective of this work is to complete the research by providing a complex verification of the novel method. The verification is done on the basis of direct comparison of hygrothermal performances of several chosen constructions loaded by both Test Reference Year (TRY) and critical weather year. For that purpose, two damage functions are adopted, in order to evaluate the severity of both TRY and critical weather year. Based on the outputs of applied damage functions it can be concluded that the critical weather year is able to induce more severe stress to the studied constructions than TRY. Therefore, the verification of the original method is considered as successful.

INTRODUCTION

Boundary conditions are considered as one of the most important factors having direct influence on the results of hygrothermal simulations. Since the complexity of new and refurbished building envelopes and structures is growing, the hygrothermal design of both building envelopes and construction details (Langmans and Roels 2014; Kočí et al. 2012; Kočí et al., 2013; Künzler and Zirkelbach 2013) is gaining more and more importance, which is logically followed by the increased demands for the boundary conditions.

The contemporary simulation tools, e.g., Lengersfeld and Holm (2007), Grunewald (2000) or Kruijs et al. (2010), use dynamic boundary conditions as hourly values of weather data. The data is implemented mostly in the form of Test Reference Years (TRY) or Typical Meteorological Years (TMY). Some examples of generation of TRY were given by Bilbao et al. (2004), Kalamees and Kurnitski (2006) or Lee and Yoo (2010). Generation of TMY for various locations were presented by Chan et al. (2006), Oko and Ogoloma (2011) or Zang et al. (2012). The TRY and TMY are constructed based on long-term average of weather data spanning a period of more than 20 years. Therefore, the numerical simulations with

TRY/TMY boundary conditions are suitable for long-term assessment of building performance from a certain point of view. However, in hygrothermal design the boundary conditions should impose as much severe stress as possible for given locations and therefore TRY/TMY is not always suitable for these purposes. Since the moisture induced damage is caused by sudden or rapid changes of the environment, the reference or typical years must be replaced by more severe environmental loads, but still these loads must be realistic for given locations. The ideal solution may be found in the form of a critical weather year which can be defined as one particular weather year from the weather history typical for studied location that imposed most severe stress to the construction.

Estimation of induced stress to the construction may be done in several ways regarding the nature of studied damage. In the literature there are described several damage functions that quantify the damage. For example RHT – Index (Mukopadhyaya, 2006) and Time-of-Wetness (Corvo et al., 2008; Van den Bulcke et al., 2009; McCabe et al., 2013) belong to the most popular damage functions describing the moisture induced damage. Kočí et al. (2014a) introduced Winter Index damage function that is suitable for regions with sub-zero temperatures where frost damage of building structures takes place. Some other damage functions were described by Salonvaara et al. (2010).

Having the appropriate damage function for studied type of damage, the selection of a critical weather year should be quite simple. The only thing that is required is to perform a series of year-long simulations for each weather year from the weather data history for given location and then quantify the damage by respective damage function. In such a scenario, the worst weather year from the history (i.e. the year with worst output of damage function) is chosen and declared as a critical weather year. Unfortunately, the ideal solution described above is applicable only for such location where the complete weather data history is available in the digital form. As required by the modern simulation tools, the weather data must contain information about temperature, relative humidity, wind characterization, rainfall and solar radiation. However, there exist only few countries and locations all over the world, where

the weather data are complete both qualitatively and quantitatively and may be used in the above mentioned scenario for determination of the critical weather year. Very good weather data coverage is for example in Germany or USA, but most countries have to deal with the issue of selecting of a critical weather year based on incomplete weather data sets.

The solution to this problem was proposed by Kočí et al. (2014a) who introduced the method for selection of the critical weather year using partial weather data sets. The method is based on creation of an artificial weather data history of studied location using reference years from several different places having similar climate to the investigated location. Then, the severity of each weather year was ranked by the Winter Index damage function and inverse analysis was applied in order to find the mathematical formulas linking the weather data and damage function outputs. Finally, the derived mathematical formulas were used for selection of the critical weather year using the monthly averages of partial weather data for the given location, which makes the approach cost effective, affordable and applicable in various locations on the Earth. The practical demonstration of the method was done on the example of Prague, Czech Republic, where the year 1996 was pointed as one of the most severe in past 30 years. Kočí et al. (2014a) introduced the methodology and its demonstration only, however, they did not provide any verification of their method.

This paper can be considered as a follow-up of the work presented by Kočí et al. (2014a) providing a complex verification of the method for selection of the critical weather year. The objective is to investigate the severity of 1996 weather year in comparison with TRY and to conclude whether the 1996 is more severe than TRY or not. In case the 1996 is more severe than TRY, such conclusion would support the previous research work. The verification is done by comparing the hygrothermal response of several contemporary building envelopes loaded by TRY and critical weather year. The hygrothermal response of the constructions is investigated by the mean of the frost damage. However, contrary to the original research another frost damage functions were added to the damage function portfolio to make the verification process as thorough as possible.

VERIFICATION OF THE CRITICAL WEATHER YEAR

Weather data

The verification of the method for selection of the critical weather year was done on the basis of comparison of hygrothermal responses of the studied constructions exposed to two different sets of boundary conditions. The verification process follows

the demonstration of the method for selection of the critical weather year presented in the original paper (Kočí et al., 2014a). Since the authors demonstrated the applicability of the method for the climatic conditions of Prague, Czech Republic, the verification is done for the same location. The first set of boundary conditions was represented by the Test Reference Year for Prague, Czech Republic. The second set was represented by the weather year 1996 for the same location. All the weather data were obtained from the Czech Hydrometeorological Institute (CHMI), which is the official authority for meteorology, climatology, hydrology and air quality protection in the Czech Republic. The summary of temperature, relative humidity and precipitation of both involved weather years is given in Table 1. The data for the year 1996 were custom-prepared and its completion took several months. In Table 1, Temp is average monthly temperature, RH is average monthly relative humidity and PP is monthly amount of precipitation.

Table 1: Summary of chosen weather characteristics of involved weather years

	Temp [°C]		RH [%]		PP [l/m ² month]	
	TRY	1996	TRY	1996	TRY	1996
Jan	-1.13	-4.75	78.71	89.56	25.80	7.20
Feb	0.00	-4.33	78.89	82.59	20.00	11.10
Mar	4.51	-0.42	68.70	83.35	26.70	13.00
Apr	7.84	7.77	70.13	66.18	34.70	11.30
May	13.43	11.45	68.25	82.87	64.40	98.90
Jun	15.81	16.02	72.86	75.34	70.20	81.52
Jul	18.25	15.23	67.73	77.80	80.70	115.78
Aug	17.87	16.59	69.14	79.42	73.20	61.80
Sep	13.47	9.94	77.43	83.79	46.70	40.00
Oct	8.78	9.30	78.89	84.82	28.80	30.40
Nov	3.39	4.27	83.43	85.68	28.80	24.70
Dec	1.12	-4.69	76.21	88.18	21.50	17.60

Although only temperature, relative humidity and precipitation are shown in Table 1, the other weather data such as wind direction, wind velocity, diffuse and direct short wave radiation, sky long wave emission radiation and long wave emission radiation were used in the numerical simulations as well. The temperature and relative humidity as a function of time are shown in Figures 1 and 2.

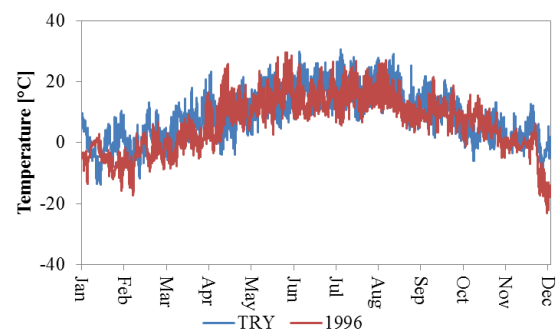


Figure 1: Temperature development during the year

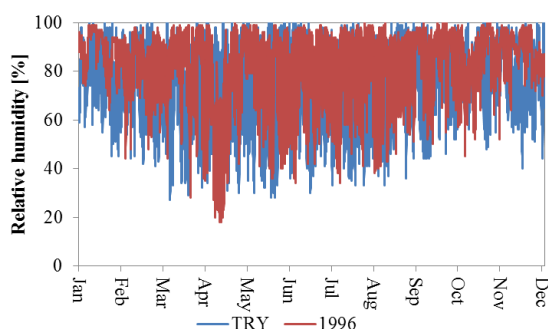


Figure 2: Relative humidity development during the year

Studied building envelopes and computational simulation of their hygrothermal performance

The verification of the critical weather year was done on several different types of heavy building enclosures having both contemporary and historical composition in order to make the verification as extensive as possible. All of the studied materials were used in the Czech Republic in the past or are being used nowadays. The load-bearing materials were represented by autoclaved aerated concrete (AAC), concrete, ceramic brick, advanced hollow clay brick filled with expanded polystyrene and sandstone. The contemporary building envelopes were provided with different types of thermal insulation layers, including polystyrene and mineral wool. The historical masonry was considered without any thermal insulation. The exterior plasters were chosen with respect to the material composition of the envelopes. On the interior side of all studied structures 10 mm thick lime-cement plaster was assumed. The detailed list of studied building envelopes used in the verification process is given in Table 2. Following abbreviations are used in the table: AAC – autoclaved aerated concrete, AHCB – advanced hollow clay brick, EPS – expanded polystyrene, MW – mineral wool, LCP – lime-cement plaster, LPP – lime-pozzolan plaster, RPHM – renovation plaster for historical masonry,

Table 2: List of studied constructions

No.	Load-bearing material	Thermal insulation	Plaster
1	AAC (375 mm)	EPS (100 mm)	LCP (10 mm)
2	AAC (375 mm)	MW (100 mm)	LCP (10 mm)
3	Ceramic brick (450 mm)	N/A	LCP (10 mm)
4	Ceramic brick (450 mm)	EPS (100 mm)	LCP (10 mm)
5	Ceramic brick (450 mm)	MW (100 mm)	LCP (10 mm)
6	Concrete (300 mm)	EPS (100 mm)	LCP (10 mm)
7	Concrete (300 mm)	MW (100 mm)	LCP (10 mm)

8	AHCB (500 mm)	N/A	LPP (10 mm)
9	AHCB (500 mm)	EPS (100 mm)	LPP (10 mm)
10	Sandstone (800 mm)	N/A	N/A
11	Sandstone (800 mm)	N/A	RPHM (10 mm)

For each building envelope listed in Table 2, computer simulation of hygrothermal performance for 5 consecutive years was conducted. Each simulation was carried out with both TRY and critical weather year as the boundary conditions in order to allow the direct comparison of the hygrothermal performance. The computational simulations were accomplished using HEMOT simulation tool (HEat and MOisture Transport) (Kočí et al., 2010) which is based on the general finite element package SIFEL (SIMple Finite Elements) (Kruis et al., 2010) and uses implementation of Künzels mathematical model of coupled heat and moisture transport (Künzel, 1995). However, the Künzels mathematical model was further modified in this case in order to distinguish more precisely between liquid and gaseous phase of moisture transport and in this way to bring higher accuracy to the calculations (Đurana et al., 2015; Maděra et al., 2015a, Maděra et al., 2015b). HEMOT allows the simulation of transport phenomena in constructive building details for 1D and 2D problems, whereas the basic variables characterizing the hygrothermal state of building constructions (temperature, moisture content, relative humidity) can be obtained as functions of space and time. The HEMOT code allows an investigation of variants concerning different constructions, different materials, and different climatic loads. HEMOT uses a material database as data source, which simplifies computations and allows obtaining more complex results. The hygric, thermal and basic physical properties of building materials which were used in the simulations as input parameters were taken from the following sources: ceramic brick (Čáchová et al., 2014), autoclaved aerated concrete (Jerman et al., 2010, Jerman et al., 2013), advanced hollow clay brick (Korecký et al., 2013a, Korecký et al., 2013b), concrete (Vejmelková et al., 2010), sandstone (Kočí et al., 2014b), mineral wool and expanded polystyrene (Jerman and Černý, 2012, Jiříčková and Černý, 2006), lime-pozzolan plaster (Maděra et al., 2015b) and renovation plaster for historical masonry (Vejmelková et al., 2012).

Applied damage functions

For the assessment of severity of TRY and critical weather year, several damage functions were used. All of the damage functions were designed to quantify the severity in terms of frost induced damage. However, since they are designed to be

applied directly on the results of hygrothermal simulations only, their application is thus limited to relative comparison of different weather years or relative comparison of different constructions under the same environmental load. Therefore, these damage functions are not intended to quantify or describe any kind of particular damage.

The dominating damage function was the Winter Index approach, which the original method presented by Kočí et al. (2014a) was based on. The Winter Index function was extended by another damage function called Time-of-Frost in order to provide complex verification of the selected critical weather year. Both damage functions work on the basis of hourly values of temperature and relative humidity from 365 consecutive days (8760 hours) and their definitions are given below.

The Winter Index (WI) is the damage function proposed in the original research paper by Kočí et al. (2014a). WI calculates the level of severity as

$$WI = \sum_{i=1}^{8760} (T_i - T_0)(RH_i - RH_0), \quad (1)$$

where T_0 and RH_0 are reference values of temperature and relative humidity and T_i and RH_i are hourly values of temperature and relative humidity. The reference values T_0 and RH_0 were set as 0 °C and 95 %, respectively. The WI is calculated only when both $T_i < T_0$ and $RH_i > RH_0$.

The Time-of-Frost (TOF) is newly introduced damage function inspired by traditional Time-of-Wetness damage function (Corvo et al., 2008; Van den Bulcke et al., 2009; McCabe et al., 2013). TOF calculates the number of hours during the year when the conditions in the investigated point of the structure are favourable for ice formation, i.e., the temperature is below the reference temperature while the relative humidity is above the reference value. The reference values are the same as in WI function. The TOF ranges between 0 and 8760, alternatively it can be expressed in %.

Alternatively, both damage functions can work with temperature and moisture content values as well. In this case, the critical amount of moisture content usually corresponds to the hygroscopic moisture of the material.

RESULTS AND DISCUSSION

The building envelopes listed in Table 2 were subjected to the computer simulations with two different sets of boundary conditions. For the investigation of their hygrothermal performance damage functions described in previous section were used. The points of investigation were placed 5 mm under the exterior surface of each building envelope

(i.e., in the exterior plaster) and 2 mm in the load-bearing material of each envelope. In case of building envelope made of plain sandstone where the exterior plaster was omitted (building envelope #10), only the point located 5 mm under the exterior surface was investigated. The choice of investigation points were done just for monitoring of the hygrothermal processes that occur in the material and to describe material deterioration from the hygrothermal point of view. Another important point should be placed at the interface of the load-bearing material and plaster in order to describe mechanical aspects of ice damage. However, in this case an advanced mechanical model would be needed in order to quantify the detachment process. The hygrothermal performance was analyzed in the 5th year of the computational simulations in order to avoid the results being affected by initial conditions. The results of applied damage functions are summarized in Tables 3 and 4. The graphical summary of damage function outputs is given in Figs. 3 and 4.

Table 3: Comparison of the hygrothermal performance of the building envelopes investigated 5 mm under the exterior surface

BE #	WI [-]		TOF[h]	
	TRY	1996	TRY	1996
1	-243.1	-539.6	87	263
2	-177.7	-362.3	78	213
3	-116.0	-238.2	53	155
4	-234.8	-554.8	85	259
5	-225.8	-518.9	83	258
6	-227.0	-497.6	84	246
7	-183.8	-401.7	75	222
8	-605.3	-641.6	132	272
9	-680.5	-730.1	139	289
10	-150.3	-76.3	49	82
11	-170.1	-107.1	57	104

Table 4: Comparison of the hygrothermal performance of the building envelopes investigated 2 mm under the load-bearing material

BE #	WI [-]		TOF [h]	
	TRY	1996	TRY	1996
1	0	0	0	0
2	0	0	0	0
3	-3.8	-197.5	16	145
4	0	0	0	0
5	0	0	0	0
6	0	0	0	0
7	0	0	0	0
8	-143.7	-340.7	72	206
9	0	0	0	0
11	-53.2	-70.5	30	90

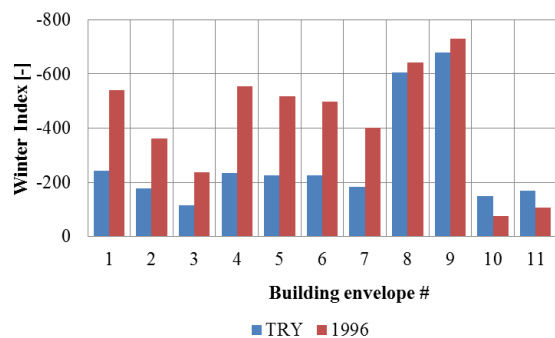


Figure 3: Comparison of Winter Index values of studied building envelopes in 5 mm under the exterior surface

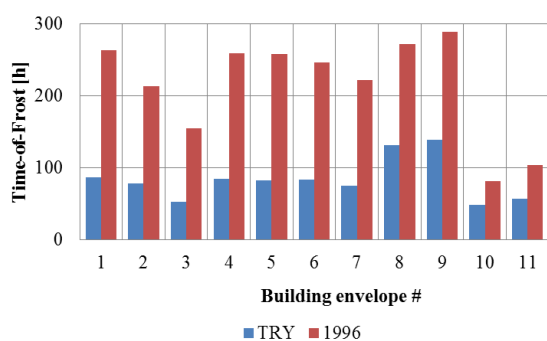


Figure 4: Comparison of number of Indicative Freeze/thaw Cycles in studied building envelopes in 5 mm under the exterior surface

The results presented in the paper clearly show that the critical weather year for Prague, Czech Republic, which was defined as the weather year 1996, can induce more favourable conditions for ice-forming process in the studied construction than TRY constructed for the same location. As the method for definition of the critical weather year presented by Kočí et al. (2014a) includes some uncertainties due to involving partial weather data, i.e., monthly averages of temperature, relative humidity and precipitation only, certain level of uncertainty was brought to the verification process. More to that, Kočí et al. (2014a) suggested the weather year 1996 to be most critical for most of the studied constructions, but not all of them. Therefore, there appeared several exceptions in the verification process, where the critical weather year did not prove the higher severity in all studied aspects. The exception can be found in sandstone masonry, both plain and plaster-provided (building envelopes 10 and 11). In these cases, Winter Index damage function returns lower (i.e., more severe) values for the construction loaded by TRY. However, the difference between hygrothermal performance of TRY- and critical weather year-loaded building envelope is not significant. The other applied damage function, Time-of-Frost, speaks in favour of the critical weather year. The explanation of this

phenomenon can be easily given by high porosity and high moisture diffusivity of sandstone allowing the moisture to be retained in the masonry. Even if the masonry loaded by TRY is exposed to the favourable ice forming conditions for significantly shorter period than loaded by critical weather year (see TOF values in Table 2), the high level of moisture accumulation in the masonry caused rapid increase of the Winter Index value. Therefore, in order to stay on the safe side of the calculations it can be concluded that the weather year 1996 in the Czech Republic can be considered as the critical weather year for most types of the building envelopes except for building stones having high water absorption properties. In such case the declaration of 1996 weather year as the critical weather year is at least questionable.

CONCLUSIONS

The main objective of the paper was to verify the method for generation of the critical weather year for the geographical areas with an alternation of freezing and thawing periods. Since the method for the generation of the critical weather year includes some simplifications in the form of using partial weather data of several environmental variables only, the complex verification was needed to make the approach usable in real applications.

In this paper a complex verification was provided following up the demonstration of the novel method proposed by Kočí et al. (2014a). It was done aimed at different building envelopes of both historical and contemporary material compositions. The verification was based on the direct comparison of hygrothermal performance of the studied building envelopes loaded by Test Reference Year and critical weather year. For the quantification of the severity of both weather years, two damage functions were adopted.

Based on the presented results it can be concluded that 1996 weather year is more severe than TRY, which supports the conclusions from previous work. Therefore, the 1996 weather year should be used as the critical weather year when assessing a frost induced damage in Prague, Czech Republic. However, some nuances have been discovered in the case of sandstone masonry and therefore in the applications of the critical weather year for such kind of envelopes one should proceed with caution.

ACKNOWLEDGEMENTS

This research has been supported by the Czech Science Foundation, under project No P105/12/G059.

REFERENCES

- Bilbao, J., Miguel, A., Franco, J.A., Ayuso, A. 2004. Test reference year generation and evaluation

- methods in the continental Mediterranean area. *Journal of Applied Meteorology*, 43, 390-400.
- Čáchová, M., Koňáková, D., Vejmelková, E., Keppert, M., Polozhiy, K., Černý, R. 2014. Pore Structure and Thermal Characteristics of Clay Bricks. *Advanced Materials Research*, 982, 104-107.
- Chan, A.L.S., Chow, T.T., Fong, S.K.F, Lin, J.Z. 2006. Generation of a typical meteorological year for Hong Kong. *Energy Conversion and Management*, 83, 87-96.
- Corvo, F., Perez, T., Martin, Y., Reyes, J., Dzib, L.R., González-Sánchez, J., et al. 2008. Time of wetness in tropical climate: considerations on the estimation of TOW according to ISO 9223 standard. *Corrosion Science*, 50 (1), 206-219.
- Đurana, K., Kočí, J., Maděra, J., Pokorný, J., Černý, R. 2015. Modification of the Computational Model of Coupled Heat and Moisture Transport: The Transition between the Liquid and Gaseous Phases of Water. In: *AIP Conference Proceedings*, 1648, p. 41004-1-41004-4.
- Grunewald, J. 2000. DELPHIN 4.1 - Documentation, theoretical fundamentals, Dresden: TU Dresden.
- Jerman, M., Kočí, V., Maděra, J., Výborný, J., Černý, R. 2010. Water and heat transport parameters of materials involved in AAC-based building envelopes. In: *1st Central European Symposium on Building Physics*. Lodz: Technical University of Lodz, 39-45.
- Jerman, M., Černý, R. 2012. Effect of moisture content on heat and moisture transport and storage properties of thermal insulation materials. *Energy and Buildings*, 53, 39-46.
- Jerman, M., Keppert, M., Výborný, J., Černý, R. 2013. Hygric, thermal and durability properties of autoclaved aerated concrete. *Construction and Building Materials*, 41, 352-359.
- Jiříčková, M., Černý, R. 2006. Effect of hydrophilic admixtures on moisture and heat transport and storage parameters of mineral wool. *Construction and Building Materials*, 20, 425-434.
- Kalamees, T., Kurnitski, J. 2006. Estonian test reference year for energy calculations, *Proceedings of the Estonian Academy of Sciences. Engineering*, 12, 40-58.
- Kočí, V., Kočí, J., Maděra, J., Černý, R. 2010. Computer code HEMOT for hygrothermal assessment of thermal insulation systems. In: *Thermophysics 2010*. Brno: Brno University of Technology, 133-140.
- Kočí, V., Maděra, J., Černý, R. 2012. Exterior thermal insulation systems for AAC building envelopes: Computational analysis aimed at increasing service life. *Energy and Buildings*, 47, 84-90.
- Kočí, V., Maděra, J., Černý, R. 2013. Computer aided design of interior thermal insulation system suitable for autoclaved aerated concrete structures. *Applied Thermal Engineering*, 58, 165-172.
- Kočí, J., Maděra, J., Černý, R. 2014a. Generation of a critical weather year for hygrothermal simulations using partial weather data sets. *Building and Environment*, 76, 54-61.
- Kočí, V., Maděra, J., Fořt, J., Žumár, J., Pavlíková, M., Pavlík, Z., Černý, R. 2014b. Service Life Assessment of Historical Building Envelopes Constructed Using Different Types of Sandstone: A computational Analysis Based on Experimental Input Data. *The Scientific World Journal*, Volume 2014, Article ID 802509, 12 p.
- Korecký, T., Jerman, M., Vejmelková, E., Černý, R. 2013a. Homogenisation of Physical Parameters of Filled Hollow Brick Block. *Stavební obzor [online]*, 22 (2), 44-47.
- Korecký, T., Jerman, M., Vejmelková, E., Černý, R. 2013a. Determination of Physical Properties of Filled Hollow Brick. *Stavební obzor [online]*, 22 (10), 254-257.
- Kruis, J., Koudelka, T., and Krejčí, T. 2010. Efficient computer implementation of coupled hydro-thermo-mechanical analysis. *Mathematics and Computers in Simulations*, 80, 1578-1588.
- Künzel, H.M., Zirkelbach, D. 2013. Advances in hygrothermal building component simulation: modelling moisture sources likely to occur due to rainwater leakage. *Journal of Building Performance Simulation*, 6 (5), 346-353.
- Künzel, H. 1995. Simultaneous Heat and Moisture Transport in Building Components: One- and Two-dimensional Calculation Using Simple Parameters, IRB Verlag, Stuttgart.
- Langmans, J., Roels, S. 2014. What are the hygrothermal consequences of applying exterior air barriers in timber frame construction in Europe? *Journal of Building Performance Simulation*, 8 (3), 191-204.
- Lee, K., Yoo, H., Levermore, G.J. 2010. Generation of typical weather data using the ISO Test Reference Year (TRY) method for major cities of South Korea. *Building and Environment*, 45, 956-963.

- Lengsfeld, K., Holm, A. 2007. Development and validation of the hygrothermal indoor climate simulation software WUFI(R)-Plus. *Bauphysik*, 29, 178-186.
- Maděra, J., Kočí, J., Černý, R. 2015a. Effect of different climatic conditions on the degradation of historical masonry in the Czech Republic. *WIT Transactions on The Built Environment*, 153, 681-692.
- Maděra, J., Kočí, J., Vejmelková, E., Čáchová, M., Jerman, M., Černý, R. 2015b. Service life assessment of exterior lime-pozzolan renders containing ceramic powder. *WIT Transactions on Modelling and Simulation*, 59, 59-70.
- McCabe, S., Brimblecombe, P., Smith, B., McAllister, D., Srinivasan, S., and Basheer, M. 2013. The use and meanings of 'time of wetness' in understanding building stone decay. *Quarterly Journal of Engineering Geology & Hydrogeology*, 46 (4), 469-476.
- Mukhopadhyaya, P., Kumaran, K., Tariku, F., Van Reenen, D. 2006. Application of hygrothermal modeling tool to assess moisture response of exterior walls. *Journal of Architectural Engineering*, 12, 178-186.
- Oko, C.O.C., Ogoloma, O.B. 2011. Generation of a typical meteorological year for Port Harcourt zone. *Journal of Engineering Science and Technology*, 6, 204-214.
- Salonvaara, M., Sedlbauer, K., Holm, A., Pazera, M. 2010. Effect of selected weather year for hygrothermal analyses. In: *Buildings XI, thermal performance of the exterior envelopes of whole buildings XI*, CD-ROM proceedings, Clearwater Beach, Florida, Atlanta: ASHRAE.
- Van den Bulcke, J., Van Acker, J., De Smet, J. 2009. An experimental set-up for real-time continuous moisture measurements of plywood exposed to outdoor climate. *Building and Environment*, 44 (12), 2368-2377.
- Vejmelková, E., Pavlíková, M., Keppert, M., Keršner, Z., Rovnaníková, P., Ondráček, M., Sedlmajer, M., Černý, R. 2010. High performance concrete with Czech metakaolin: Experimental analysis of strength, toughness and durability characteristics. *Construction and Building Materials*, 24, 1404-1411.
- Vejmelková, E., Keppert, M., Keršner, Z., Rovnaníková, P., Černý, R. 2012. Mechanical, fracture-mechanical, hydric, thermal, and durability properties of lime-metakaolin plasters for renovation of historical buildings. *Construction and Building Materials*, 31, 22-28.
- Zang, H., Xu, Q., Du, P., Ichiyanagi, K. 2012. A modified method to generate typical meteorological years from the long-term weather database. *International Journal of Photoenergy*, 2012, Article ID 538279, 9 pp.

EFFECT OF SALTS AND ABSORPTION CYCLES IN THE CAPILLARY COEFFICIENT OF BUILDING MATERIALS WITH DIFFERENT JOINTS

A.S. Guimarães¹, J.M.P.Q. Delgado¹ and V.P. de Freitas¹
(anasofia@fe.up.pt; jdelgado@fe.up.pt; vpfreita@fe.up.pt)

¹CONSTRUCT-LFC, Civil Engineering Department, Faculty of Engineering – University of Porto, Rua Dr. Roberto Frias, s/n, 4200-465 Porto, PORTUGAL Fax: +351 225081440

ABSTRACT

Rising damp can reduce building's aesthetical value, comfort and health mark, when combined with the existence of soluble salts in the building components and in the ground water can even lead to material decomposition and compromise its structural performance.

This research work intended to study the effect of different absorption cycles of two saturated solutions of sodium sulphate and potassium chloride in the capillary absorption curves obtained through the partial immersion of red brick samples without and with different joints. The results revealed significant differences in the capillary coefficients obtained when samples were tested with salt solutions.

INTRODUCTION

Rising damp is one of construction's major problems especially in old, ancient and historical buildings associated porous materials used in this industry. The phenomenon is caused by the migration of the salt ions dissolved in water into the porous network of the building's walls. This is where they remain and crystalize after the water evaporates creating great pressure against the pore walls and eventually resulting in their fracture after many cycles of crystallization/dissolution (Guimarães et al., 2013, 2012). This mechanism has a massive influence on the degradation of historical buildings since they were built in a time when construction technologies made no effort to prevent this kind of pathologies.

The construction industry uses materials with porous characteristics that favour the moisture fixation through mechanisms such as capillary, higrscopicity and condensation (Hens, 2007; Delgado et al., 2006; Hall and Hoff, 2002; Hall, 1989 and Gummerson et al., 1981). Rising damp, one of the moisture propagation mechanisms that accelerates the deterioration in buildings, may be explained by the capillary water migration from the the soil through the porous network of the materials in the building elements. In old buildings, mostly constructed in masonry, the effects of rising damp assume a greater expression, due to the porous materials typically used such as ceramic bricks, mortars and stones (Guimarães et al., 2013, 2012).

The presence of dissolved salts in the water, which up rises through the porous network of building elements, constitutes an annoying factor for its degradation (Young, 2008 and Pei, 2003). The salts follow the water during its rise in liquid phase, however the same doesn't occur when the water evaporates. The salts remain in the pores of the building materials, eventually crystallizing after the solution has reached its super-saturation state. The salt crystallization can occur on the surface of the materials, developing efflorescence that disturb the aesthetical appearance of the building, or inside the porous network, dealing great pressures in the pore walls that can fragment them when exceeds its mechanical resistance (Azevedo, 2013 and Gonçalves, 2007). The hygrothermal variations of the surrounding environment may promote cycles of crystallization/dissolution and develop breaking tensions in the pores for each cycle.

The elements and components in the constructive systems, specially the masonry, hinge their functional efficiency on the combination of different materials and characteristics, which adds to the complexity of the moisture transfer analysis. This heterogeneity require knowledge about the individual characteristics of the materials as well as the continuity conditions of the interface that separates the different materials, bidding the crucial importance of the study of the joints influence in the transport phenomenon (Guimarães et al., 2015; Derluyn et al., 2011 and Freitas, 1992).

This paper intends to report the experimental work carried out with brick specimens, aiming to evaluate the effect of salt solutions in the capillary absorption of monolithic brick specimens in comparison with water. Sodium sulphate and potassium chloride were the chosen salts to perform the experiments. The first is one of the salts that impose more degradation to buildings, the second was chosen for being very commonly found in building materials, especially the ion chloride.

MATERIALS AND METHODS

The test specimens used were nine red brick monolithic samples with the dimensions 5x5x10 cm³ (three for each solution including water). All the specimens were sealed in the lateral faces with an epoxy coating to avoid the evaporation through these

sides and assure the unidirectional moisture flow from the bottom to the specimens' top surface. Tests were performed only for pure water and two saturated salt solutions (KCl and Na₂SO₄).

The capillary absorption tests followed the procedure n° II.6 "Water Absorption Coefficient (Capillary)" of RILEM (1980). The tests were preceded by the drying of the specimens in an oven at about 60°C until obtained constant mass, in order to calculate the dry mass of the specimens. After this step, specimens were stored in the test room for some days, until they reach the hygrothermal equilibrium.

Mukhopadhyaya et al. (2002) confirmed the temperature influence on capillary absorption coefficient of brick specimens in his study with different porous materials. In order to minimize the effect of temperature on our results, tests were performed in a room with controlled temperature. The values of temperature and relative humidity (RH) of the air were measured every ten minutes for 33 days using a sequential data recording device. The mean values obtained were 22.8 °C for the temperature and 52.7 % for the RH.

Tests began with the partial immersion of the specimens 5mm deep. After the immersion, weightings were performed periodically in order to determine the amount of water absorbed during the test. On the first day, weightings were performed on all samples at minute 1, 3, 5, 10, 15, 30, 60, and afterwards at least once an hour. In general, weightings were attempted every two hours on the second day, every three hours on the third day and once a day for the remaining days of testing. This timing had yet to suffer some adjustments for some combinations tested. For instance, for the specimens with air space between layers, after the wet front have reached the interface the time between weightings were extended since the moisture transport at the interface took place in the vapour phase and was therefore much slower.

The second cycle was done, several days after the first cycle. The specimens were dried and the all the procedure used in the first cycle repeated.

The amount of absorbed water per unit area at time t_i assay $M_{w,i}$ (kg/m²) is calculated using Eq. (1), where M_0 (kg) is the dry mass of the sample, M_i (kg) of the mass of sample at time t_i and A (m²) is the area of the base of the specimen.

$$M_{w,i} = \frac{M_i - M_0}{A} \quad (1)$$

Once determined the amount of water absorbed over the time until the saturation of the porous media, it was then possible to calculate the capillary absorption coefficient and the maximum moisture flow through the interface. The capillary absorption coefficient

corresponds to the slope of the first linear portion of the absorption curve, that expresses the amount of water absorbed per unit area (kg/m²) as a function of the root of time (s^{1/2}). The maximum moisture flow through the interface corresponds to the slope of the linear approximation of the absorption curve that expresses the amount of water absorbed per unit area (kg/m²) as a function of time (s) once reached the interface.

The results of capillary absorption are given by the sorptivity S (m/s^{0.5}). This property, which depends on both the material and the liquid, expresses the tendency of a building material to absorb and transmit a liquid by capillarity (Hall and Hoff, 2002), as shown by Eq. (2):

$$S = \left(\frac{\sigma}{\eta} \right)^{1/2} \dot{S} \quad (2)$$

where σ is the surface tension of the liquid, η is the viscosity of the liquid and \dot{S} is the intrinsic sorptivity of the material.

RESULTS AND DISCUSSION

Figure 1 sketch a representation of the monolithic specimen, hydraulic continuity interface with a cementitious mortar with 7 mm thickness, perfect contact interface (the contact couldn't be absolutely perfect but both contact faces were sanded) and air space interface where, to guarantee 3 mm of air between the parts, metal plates were applied in each face (of the 4 lateral faces) to connect the parts.

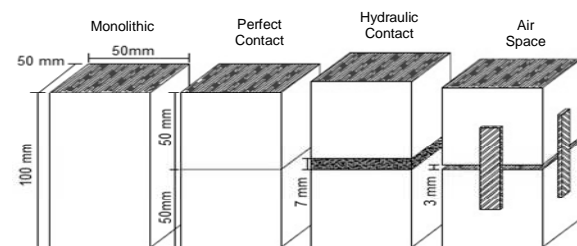


Figure 1: Virtual representation of the different types of specimen tested.

The capillary absorption curves obtained for those specimens, in the second cycle of absorption, for each one of the three solutions tested are represented in the Figure 4. The capillary absorption coefficients determined from these curves are represented in Table 1.

The results support the theory that wetting kinetics of the porous materials, at least for brick materials as it was the material used in this study, is affected by the presence of soluble salts dissolved in water.



Figure 2: Illustration of some samples before the beginning of the 2° cycle tests: (a) monolithic specimens, (b) hydraulic continuity interface and (c) air space interface.

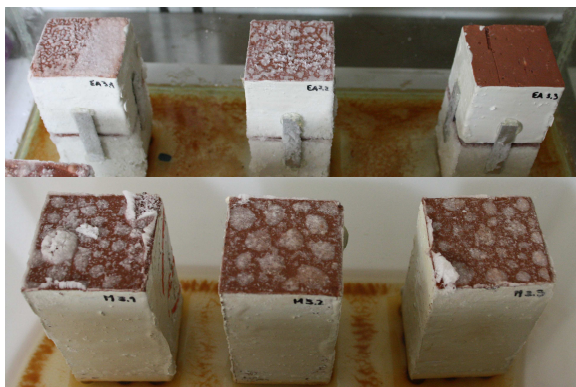


Figure 3: Illustration of some samples after several weeks of the 2° cycle tests: (a) air space interface and (b) monolithic specimens.

The capillary absorption coefficient illustrates that the presence of sodium sulphate induces a decrease in this coefficient in comparison with the reference test (pure water). On the contrary, the coefficient determined for the specimens immersed in saturated solution of potassium chloride was significantly higher than the one obtained for the reference solution. The difference between the reference absorption coefficient and the saturated solution is higher in the potassium chloride case than it is in the sodium sulphate. Our results are in line with that

observed by Azevedo (2013) who concluded that salts with potassium ion (K^+) lead to the increase of the capillary absorption coefficient when compared with pure water, while salts with sodium ion (Na^+) induce a decrease in the capillary absorption coefficient.

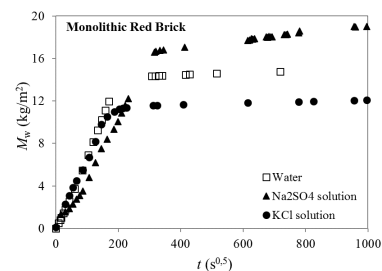
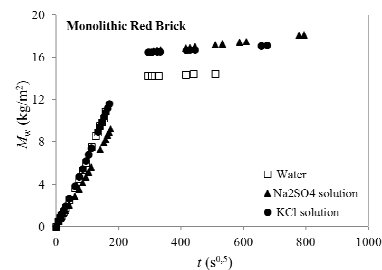
The capillary absorption curve of Red Brick samples as a function of the root of time, after 1 and 2 cycles, with the three different solutions for each joint type, is represented in the Figure 4.

A more detailed analysis was done in Figure 5, and the results obtained show that comparing the 1st and 2nd absorption cycles, it is possible to conclude that the specimens immersed in water practically absorbed the same amount of water, but when the samples are immersed in salt solutions (Na_2SO_4 and KCl) the mass gain in the absorption process is lesser in the 2nd cycle than in the 1st cycle.

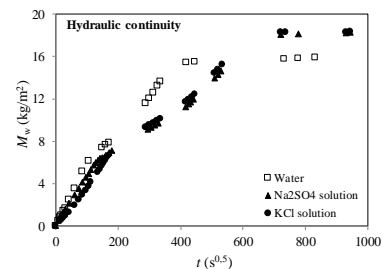
Table 1.

Capillary absorption coefficient of monolithic red brick specimens partially immersed in pure water and saturated solutions of KCl and Na_2SO_4 .

Solution	Capillary absorption coefficient [$kg/(m^2 \cdot s^{1/2})$]		
	Mean	Standard deviation	Variation Coeff (%)
Water	0.0675	0.0035	5.2%
Water+ Na_2SO_4	0.0551	0.0025	4.5%
Water+ KCl	0.0660	0.0025	10.6%



(a)



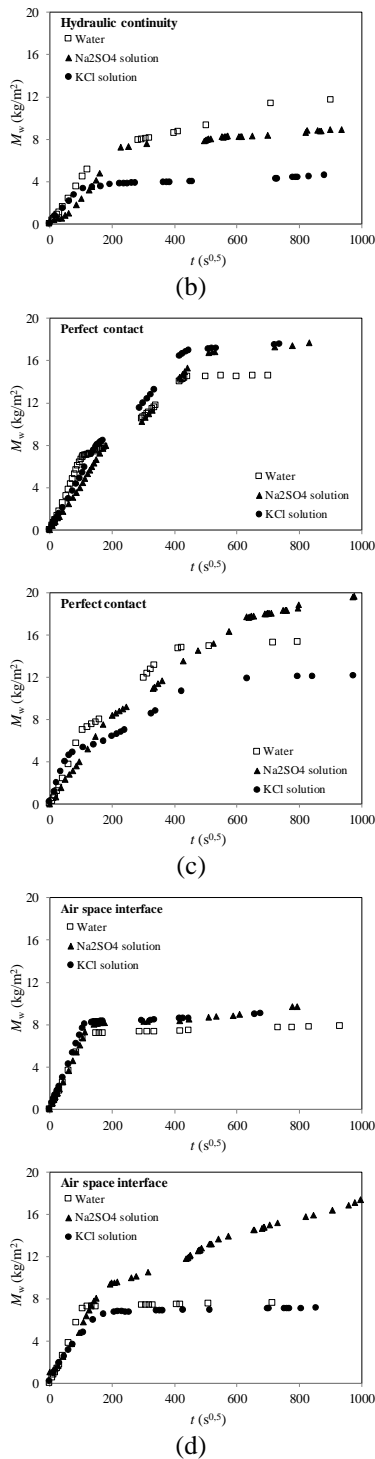


Figure 4: Capillary absorption curve of Red Brick samples as a function of the root of time, after 1 and 2 cycles, with pure water and saturated solutions of KCl and Na₂SO₄, for: (a) monolithic specimens, (b) hydraulic continuity interface, (c) perfect contact interface and (d) air space interface.

Figure 6 shows the mass gain by the samples tested in water and both salts solutions, for the three different joints analysed. For hydraulic continuity interface, the contact between layers were done with a mortar joint of 7 mm and with an interpenetration of both layers. Figure 6 shows a slowing of the wetting process when

the moisture reaches the interface due to the interface hygric resistance. This result reveals the existence of a resistance associated with the maximum flow transmitted (FLUMAX), who presents the higher value FLUMAX, as showed in Figure 7. The maximum flow transmitted value is a parameter easy to obtain experimentally and an important input for the hygrothermal programs available in literature (Delgado et al., 2010). FLUMAX can be obtained with the curve that relates the weight variation as a function of the time and can be defined as the pendent of the curve, after the water reach the interface, which means, the pendent of the second part of the curve.

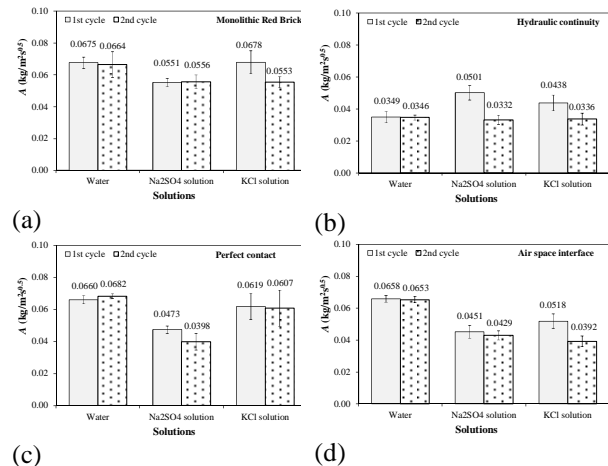


Figure 5: Water absorption coefficient of Red Brick samples after 1 and 2 cycles, with pure water and saturated solutions of KCl and Na₂SO₄, for: (a) monolithic specimens, (b) hydraulic continuity interface, (c) perfect contact interface and (d) air space interface.

In the case of the perfect contact interface, the curve in Figure 6 shows a slowing of the wetting process when the moisture reaches the interface, due to the interface hygric resistance. Once again, this result reveals the existence of a resistance associated with the maximum flow transmitted, but the lower slow mass gain by the samples indicate a high hygric resistance and an expectable lower maximum flow transmitted value than the obtained in the hydraulic continuity interface situation.

Finally, for the samples with air space interface, the samples are separated by about 3 mm of an air space in order to have an hidric cut that prevents the moisture transfer in liquid phase. Figure 6 shows a slowing of the wetting process when the moisture reaches the interface due to the interface hygric resistance however, this hygric resistance is higher than the resistance observed in the perfect contact interface. This phenomenon is observed by the extremely slow weight gain presented in Figure 6, for the situation described, and once again reveals the existence of a resistance associated with the

maximum flow transmitted. This value is expected to be lower than the obtained with a perfect contact interface (see Figure 7).

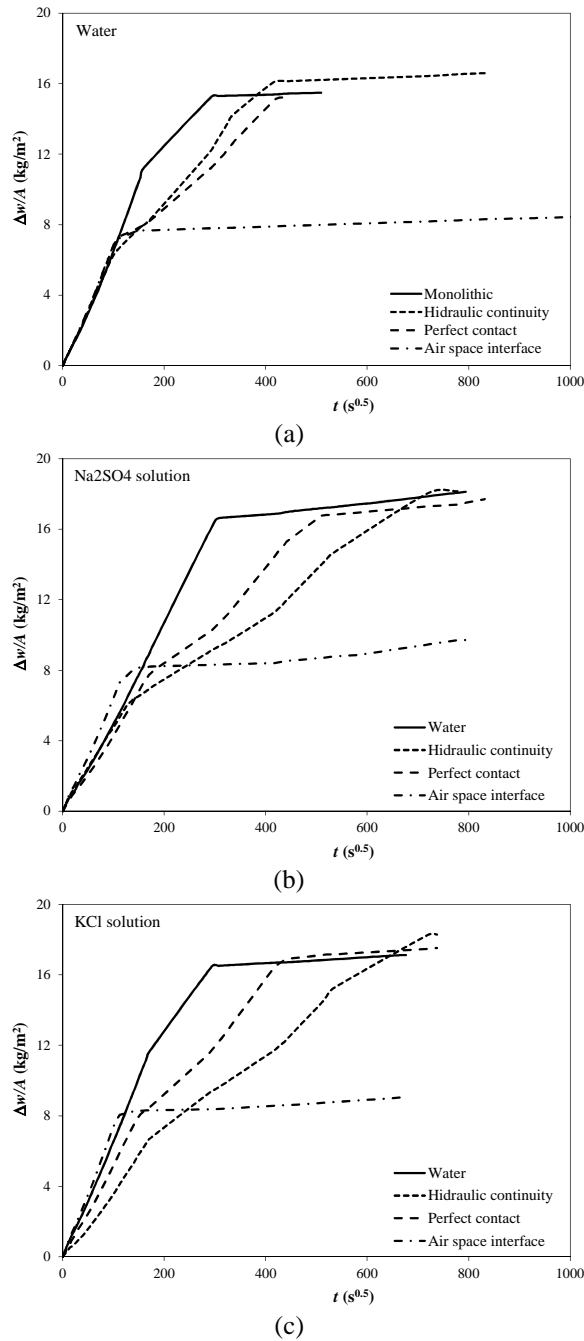


Figure 6: Representation of the absorption in the monolithic specimens, and specimens with hydraulic continuity interface, Perfect contact interface and air space interface, for: (a) pure water, (b) saturated solution of KCl and (c) saturated solution of Na₂SO₄.

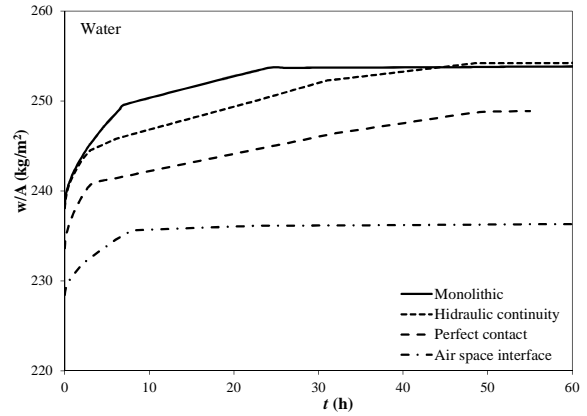


Figure 7: Effect of the different interfaces on the FLUMAX of monolithic specimens, hydraulic continuity interface, perfect contact interface and air space interface.

CONCLUSIONS

In this work an extensive experimental campaign was presented to study the effect of different absorption cycles of two different saturated solutions of sodium sulphate and potassium chloride in the capillary absorption curves obtained through the partial immersion of red brick samples without and with different joints. The drying kinetic process was also analysed for all the samples tested.

The main conclusions were:

- Both salts influence the capillary absorption coefficient in a distinct way. The presence of sodium sulphate induces a decrease in this coefficient compared to tests performed with pure water, while the tests performed with potassium chloride showed an increase of the capillary absorption coefficient compared to pure water, despite presenting a lower difference.
- All three types of interface studied presented hydric resistance during the capillary absorption tests, although with different levels of magnitude. Specimens with air space between layers offered much more resistance to moisture transport through their interface compared to both perfect contact and hydraulic contact specimens due to the fact that moisture only flow in vapour phase unlike the other two which also support liquid phase transport.
- Comparing our results with those obtained by Freitas (1992) helped sustaining the author's theory that maximum moisture flow through the air space and perfect contact interfaces (individually) may be fixe within a close range of values for the same material, since the maximum moisture flow values determined in this work were very close to the author's for a similar used material.
- Specimens with hydraulic contact interface presented more heterogeneous results. Furthermore this kind of interface's hydric resistance depends on several factors like the water/cement ratio and

curing conditions. Despite the difference between the specimen's characteristics, a comparison between ours and Cunha's results shows distinct behaviours in moisture transport through the interface despite using the same cement material.

REFERENCES

- [1] A.S. Guimarães, J.M.P.Q. Delgado and V.P. de Freitas; "Rising damp in walls: Evaluation of the level achieved by the damp front"; *Journal of Building Physics*; Vol. 37(1); 6-27; 2013.
- [2] A.S. Guimarães, J.M.P.Q. Delgado and V.P. de Freitas; "Rising damp in building walls: the wall base ventilation system"; *Heat and Mass Transfer*; Vol. 48(12); 2079-2085; 2012.
- [3] H.S. Hens; "Building physics – heat, air and moisture – fundamentals and engineering methods with examples and exercises"; Ernst & Sohn, Belgium; ISBN: 978-3-433-01841-5; 2007.
- [4] C. Hall; "Water sorptivity of mortars and concretes - a review"; *Magazine of Concrete Research*; Vol. 41; 51–61; 1989.
- [5] R.J. Gummerson, C. Hall and W.D Hoff; "Water movement in porous building materials-III. A sorptivity test procedure for chemical injection damp proofing"; *Building and Environment*; Vol. 16 (3); 193-199; 1981.
- [6] C. Hall and W.D Hoff; "Water transport in brick, stone and concrete"; London, UK, New York, NY: Taylor & Francis; ISBN: 0-419-221890-X; 2002.
- [7] J.M.P.Q. Delgado, N.M.M. Ramos and V.P. de Freitas; "Can moisture buffer performance be estimated from sorption kinetics?"; *Journal of Building Physics*; Vol. 29(4); 281-299; 2006.
- [8] L. Pel, H. Huinink and K. Kopinga; "Salt transport and crystallization in porous building materials"; *Magnetic Resonance Imaging*; Vol. 21; 317–320; 2003.
- [9] D. Young; "Salt attack and rising damp, A guide to salt damp in historic and older buildings"; Heritage Council of NSW, Heritage Victoria, South Australian, Adelaide City Council, ISBN 978-0-9805126-4-9; 2008.
- [10] T. Gonçalves; "Salt crystallization in plastered or rendered walls"; PhD Thesis Technical University of Lisbon and LNEC, Lisbon, Portugal; 2007.
- [11] J. Azevedo; "Capillary absorption of porous materials in salt solutions"; MSc. Thesis; Faculty of Engineering, University of Porto, Porto, Portugal; 2013.
- [12] V.P. de Freitas; "Moisture transfer in building walls – Interface phenomenon analyse"; PhD Thesis; Faculty of Engineering, University of Porto, Porto, Portugal; 1992.
- [13] A.S. Guimarães, J.M.P.Q. Delgado and V.P. de Freitas; "Influence of mortar joints on the moisture transfer in layered materials"; *Defect and Diffusion Forum*; Vol. 365; 160-165; 2015.
- [14] H. Derluyn, H. Janssen, and J. Carmeliet; "Influence of the nature of interfaces on the capillary transport in layered materials"; *Construction and Building Materials*; Vol. 25(9); 3685–3693; 2011.
- [15] RILEM TC 25-PEM; "Recommended tests to measure the deterioration of stone and to assess the effectiveness of treatment methods"; *Materials and Structures*; Vol. 13; 204-209; 1980.
- [16] P. Mukhopadhyaya, K. Kumaran, N. Normandin and P. Goudreau; "Effect of surface temperature on water absorption coefficient of building materials"; *Journal of Thermal Envelope and Building Science*; Vol. 16; 179-195; 2002.
- [17] J.M.P.Q. Delgado, N.M.M. Ramos, E. Barreira and V.P. de Freitas; "A critical review of hygrothermal models used in porous building materials"; *Journal of Porous Media*; Vol. 13(3); 221-234; 2010.

A THERMAL CONDUCTIVITY PREDICTION MODEL FOR POROUS BUILDING BLOCKS

W. Van De Walle and H. Janssen

KU Leuven, Department of Civil Engineering, Building Physics Section
Kasteelpark Arenberg 40 – bus 02447, BE-3001 Heverlee (Leuven), Belgium

Wouter.VanDeWalle@kuleuven.be

ABSTRACT

A 3D model for the prediction of the effective thermal conductivity of porous building blocks is introduced. Simulations are performed directly on the microstructure using voxel images and the finite element technique. Very good agreement with analytical solutions is achieved. The model is used to investigate the miscalculation effect of 2D simulations, clearly indicating the need for a 3D model. Furthermore, a method for incorporating radiative heat transfer at the microscale is implemented and applied on a synthetic sample, demonstrating the influence of thermal radiation on the effective thermal conductivity.

INTRODUCTION

Highly porous building blocks find frequent use in the construction of buildings because of their relatively high resistance to heat transfer. Typical examples include cellular concrete, cellular glass, and more recently also building blocks based on slag waste and other secondary materials. However, due to increasingly stringent energy regulations, there is an ever growing demand for even better insulating building blocks.

The heat flow through such building materials is usually described at the macroscale with Fourier's law using the effective thermal conductivity (ETC), while in fact it originates from the aggregation of conductive, radiative and convective heat transfer at the microscale. The relative contribution of each of these heat transfer mechanisms depends strongly on the microstructural parameters, i.e. porosity, pore size, matrix connectivity etc. (Carson et al. 2003). A correct understanding of the direct relation between these microstructural parameters and the total heat transport is therefore crucial in the development of improved building blocks. However, current models attempting to study their influence still exhibit large errors due to 2D simplifications, neglect of thermal radiation or their very limited applicability for a restricted class of materials (Randrianalisoa & Baillis 2014).

This paper presents a newly developed 3D FEM model for simulating the heat transport through a porous structure at the microscale. The first part

explains the workflow of the model, followed by a verification study on an elementary pore structure. Subsequently, a method for incorporating radiative heat transfer at the microscale is studied and extended. Finally, in the remainder of the paper, the model is used to make a first study on the discrepancy between 2D and 3D simulations of the same sample, and to study the share of thermal radiation on the ETC.

SIMULATION MODEL

The effective thermal conductivity of a porous material is obtained by simulating the heat transfer through a representative cubic sample at the microscale. The model is subdivided in three steps: (1) obtaining the geometrical representation of the microstructure, (2) creating a finite element mesh and (3) simulating the heat flow through the microstructure. All three steps are explained below. Each step is completely controlled via a set of Matlab routines, hence leading to an automated and easily parameterized workflow. A summarizing overview of the model workflow is shown in Figure 1.

Geometry: 3D voxel image of the microstructure

The model is based on a 3D voxel image – the 3D equivalent of a 2D pixel image – representation of the microstructure. The numeric value of each voxel indicates which material phase is located at that specific location. These voxel images can generally be acquired in two ways: via micro-CT scanning or via synthetic generation techniques.

Using the micro-CT technique, the microstructure of a physical sample is obtained through x-ray imaging and computed tomography. Objects containing features down to several micrometers can be resolved, hence allowing to incorporate the true microstructural properties of the sample. A CT scan voxel image of a cellular concrete is shown in Figure 1a.

Using synthetic generation methods, the 3D voxel image is constructed in a deterministic or stochastic manner. The technique hence allows for fast designing and testing of new microstructures and a more thorough study of specific microscale parameters. A classic method is the generation and insertion of spherical pores in a solid material like described by

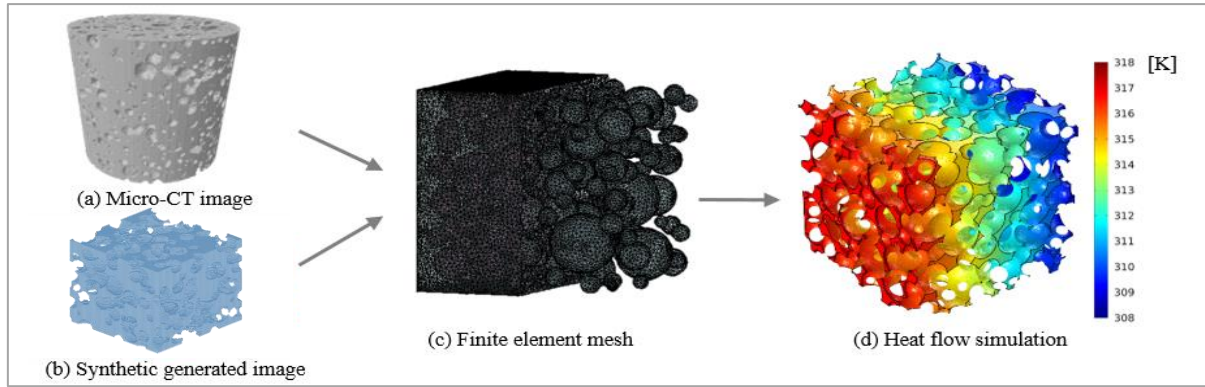


Figure 1: Different steps in the workflow of the model

She et al. (2014). Besides, the discrete voxel image format also allows for the generation of non-analytically describable pore structures, leading often to much more realistic microstructures. Recent examples can be found in Gaiselmann et al. (2014). For this paper, we have currently implemented a simple sphere generation algorithm based on the method of W. She. An example of a generated structure is shown in Figure 1b.

Both methods provide a 3D voxel image, with a level of detail depending on the used resolution (the total amount of voxels). A higher resolution should hence be used for resolving smaller features, taking into account the increasing memory usage. Finally, the image can be imported into Matlab as a 3D binary matrix. This allows for an easy manipulation of the sample and the calculation of several microstructural properties like porosity, pore size distribution etc.

Meshing procedure

A finite element mesh is created from the 3D voxel image using the open source iso2mesh Matlab toolbox (Fang & Boas 2009). This provides an extensive set of routines for manipulating the sample and extracting a tetrahedral mesh based on the c++ CGAL library (Alliez et al. 2015). To cope with the complex pore scale geometry, the code makes use of the Delaunay triangulation technique, resulting in a fast generation of relatively qualitative elements. Furthermore, the technique inherently smooths jagged surfaces between the different material phases. We extended the meshing procedure with a point insertion algorithm, leading to a better approximation of the straight edges of the cubic sample. The density of the mesh is controlled through the set maximum radii for the surface and tetrahedra circumscribing Delaunay ball. A quadratic shape function is used in all the elements. An example mesh is shown in Figure 1c.

Simulation

The finite element mesh is imported into the *COMSOL* simulation package to perform heat transfer simulations. The thermal conductivity of the gaseous and solid phase are applied to the respective regions. A method for including thermal radiation is elaborated

further in the paper. Natural convection on the other hand can effectively be neglected for pores with a diameter smaller than 4 mm (Clyne et al. 2006) and is hence not implemented.

A temperature difference of 10 K is applied between opposing boundaries while the other boundaries are set to adiabatic boundary conditions. The successive over relaxation (SOR) solver with relative tolerance of 10^{-4} is applied, showing good performance for solving the system of equations. An example temperature profile of a sample is shown in Figure 1d.

After the stationary simulation, the ETC can finally be calculated by rewriting the Fourier heat law according to J. Chen et al. (2015) for cubic samples:

$$\lambda_{eff} = \frac{\int_{V_{cube}} q_x * dV}{(T_{hot} - T_{cold}) * (L_{sample})^2} \quad (1)$$

λ_{eff} = the effective thermal conductivity of the sample [W/mK]; V_{cube} = the volume of the cubic sample [m³]; q_x = the heat flux in every element in the direction of the applied temperature gradient [W/m²]; T_{hot}/T_{cold} = the temperature applied at the hot, respectively cold side [K]; L_{sample} = the thickness of the cubic sample.

VERIFICATION OF THE MODEL

The model is verified using a synthetic sample having identical spherical pores arranged in a lattice of the face-centred cubic (fcc) type. This elementary packing of spheres consists of a repetitive cube having a pore centered on every corner and on every face, as shown in Figure 2b.

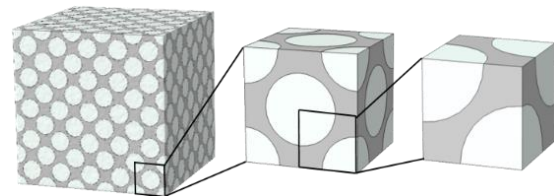


Figure 2: A sample with fcc packing at 50% porosity (a), the repetitive cube (b), and the unit cell (c).

Although the heat flow through such a repetitive cube is – due to the perfect symmetry – representative for larger arrangements, a larger sample is generated to demonstrate the possibilities of the model for working with larger datasets. A cubic sample consisting of $5 \times 5 \times 5$ of these representative cubes is generated, following the recommendations of Chen et al. (2015) on the size of a representative volume for heat transfer in random microstructures. Samples at 5 different porosities between 10 % and 90 % and with a side length of 1 mm are obtained by varying the diameter of the pores. A sample of 50 % porosity is shown in Figure 2a. A resolution of 400^3 voxels is used for constructing the 3D binary image of the microstructure together with a maximum Delaunay radius of 1/50 mm for the meshing procedure. The thermal conductivity of the matrix and the air-filled pores are set to respectively 1 W/mK and 0.025 W/mK, the temperature difference across the sample to 10 K.

The resulting effective thermal conductivities of the samples are calculated using Eq. 1, and are shown in Figure 3 as a function of porosity. They are compared with solutions of an analytical approximation derived by McKenzie et al. (1978) for the effective conductivity of fcc sphere packings up to their maximum porosity of 74 %. The analytical approximation still neglects however higher order terms, resulting in deviations from the correct solution at high porosities. Therefore, this analytical reference solution is complemented with numerical simulations performed directly in *COMSOL*. A representative unit cell of the fcc structure shown in Figure 2b is modelled, using the program’s own geometry and mesh creation functions. These results are also shown in Figure 3, together with the relative error η between the model and this numerical reference solution.

The pore-scale model agrees very well with both of the reference solutions until a porosity of about 60 %, showing relative errors of less than 2 %. As expected, above 60 % porosity the analytical approximation gets

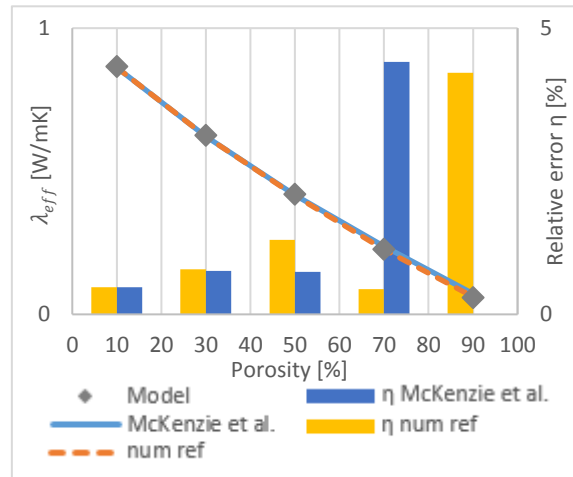


Figure 3: Verification of model with reference solutions.

less accurate showing larger discrepancies with the numerical reference model. The pore-scale model still performs very good though when compared with the numerical reference model, resulting in relative errors of less than 5 % for porosities up to 90 %.

Influence of resolution and mesh size

The accuracy of the simulations depends strongly on a correct approximation of the porous structure by the 3D image and the extracted finite element mesh. This is affected by the model through the resolution and maximum mesh element size. To investigate the influence of both parameters, 9 unit cells with different porosities of the face centred cubic pore structure are simulated using the voxel-image-based model. Each sample is modelled using 3 different resolutions (25^3 , 50^3 and 100^3) and 3 different maximum mesh sizes ($L_{sample}/10$, $L_{sample}/25$ and $L_{sample}/50$). The results are compared with the numerical reference model of the unit cell modelled in *COMSOL*. The relative errors are shown in Figure 4 as a function of porosity, resolution and mesh size.

As expected, a finer resolution and smaller mesh size generally lead to more accurate results. Resolution

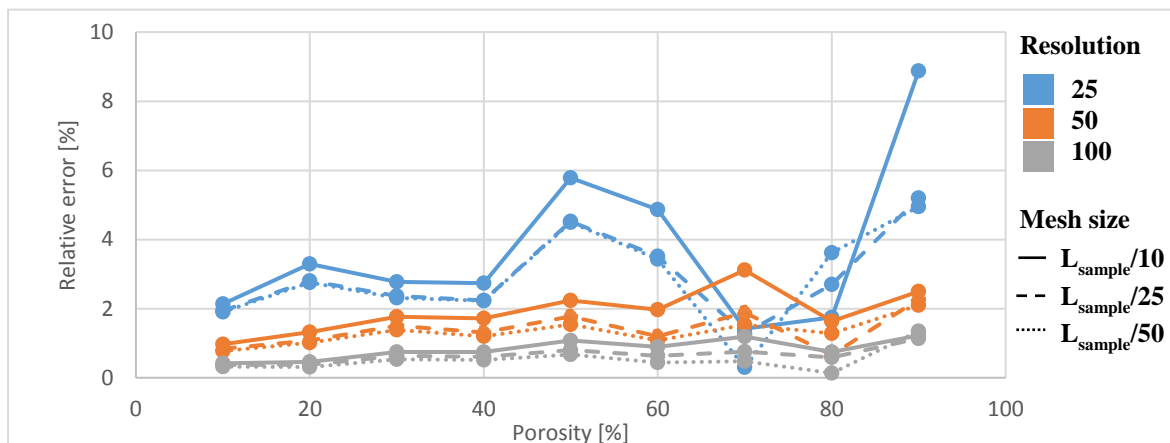


Figure 4: Influence of porosity, resolution and mesh size on accuracy.

seems to be the most important parameter, with a resolution of 50^3 or higher leading to relative errors lower than 5 % for every studied porosity and mesh size. Furthermore, it appears that high porosity samples require a finer resolution. This phenomenon could be attributed to the matrix walls becoming thinner at higher porosities, which means they get represented by a relatively smaller amount of voxels leading to a poor conformity between the mesh and the geometry. These findings should be considered when applying the model in future studies.

INCORPORATION OF RADIATIVE HEAT TRANSFER

Radiative heat transfer between the pore walls can play an important role in the total heat flow through the material, particularly in materials with high porosity, at elevated temperatures, or with a low thermal conductivity gas in the pores (i.e. vacuum insulation). However, due to its modelling complexity and 4th order terms, it is often neglected to simplify simulations, leading to underestimations of the real ETC as pointed out by Wang & Pan (2008). Simple corrections for the neglect of thermal radiation are then often made by adding a macroscale effective radiative conductivity to the effective thermal conductivity:

$$\lambda_{eff} = \lambda_{cond,macro} + \lambda_{rad,macro} \quad (2)$$

The value for $\lambda_{rad,macro}$ is usually obtained via either a formula based on averaged microscopic properties or via an experimental test defining a mean extinction coefficient. However, both methods are often not very accurate and the experimental parameters are cumbersome to obtain. Furthermore, the mutual influence of conductive and radiative heat transfer at the microscale is not taken into account.

To overcome the aforementioned limitations, the model developed in this study includes radiation directly at the pore scale. Classic thermal radiation modelling methods using view factors or Monte Carlo beams would however require unreasonable amounts of both CPU time and RAM memory due to the large total pore surface area. Therefore, a method introduced by Loeb (1954) is adopted and expanded. Based on the analogy with radiative heat transfer between parallel plates, he described the radiative heat transfer in a pore as a conductive process by defining an equivalent radiative thermal conductivity $\lambda_{rad,pore}$ at the pore scale as a function of the pores characteristics:

$$\lambda_{rad,pore} = 4 * \epsilon * \sigma * d_{max} * \gamma * T^3 \quad (3)$$

ϵ = the radiative emissivity of the matrix walls; σ = the stefan-boltzmann constant; T = the mean temperature of the pore in Kelvin; d_{max} = the maximum distance inside the pore; γ = a geometrical factor.

Loeb analytically determined the geometrical factor γ to be $2/3$ for spherical pores and $\pi/4$ for cylindrical

pores perpendicular to the heat flow. This $\lambda_{rad,pore}$ can subsequently be added to the thermal conductivity of the gas inside the respective pore (i. e. 0.025 W/mK for air). Hence, radiation is incorporated locally at the microscale, while maintaining a feasible simulation model. This method was further investigated by Bakker et al. (1995), numerically determining the geometrical factor for a range of oblate ellipsoid shaped pores. His results showed values for γ varying from 0.45 to 0.66, hereby demonstrating the large dependence of the geometrical factor on the pore geometry. However, until now a clear relation between the pore's geometrical parameters and the geometrical factor γ is still lacking, hence impeding the correct incorporation of radiative heat transfer at the microscale.

Therefore, this paper extends the studies of Loeb and Bakker with a large range of elliptic and ellipsoidal pores, considering the fact that most pores inside porous building materials can effectively be approximated using ellipsoids. An analytical formula relating the geometrical factor to the pore's geometry is proposed.

2D calculation of radiation in pores

As a stepping stone for more complex 3D simulations, we start with 2D simulations of radiative heat transfer in elliptic pores. The equivalent geometrical factor γ is calculated performing a set of simulations on a square containing just one such elliptic pore. Different ellipses are studied by varying the 3 different geometrical parameters (the long diameter 'a', the ratio of the diameters 'b/a' and the angle ' α ' with the horizontal) shown in Figure 5.

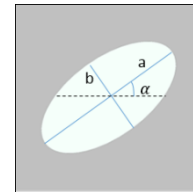


Figure 5: View on the elliptic pore parameters

The opposing sides of the squares are assigned with a temperature difference of 1 K, while the matrix and air thermal conductivity are set to 1 W/mK and 0.025 W/mK. Simulations are performed at 7 different mean temperatures. In this first study, only an emissivity of 0.9 is considered, although Fitzgerald & Strieder (1997) have shown that the pore scale radiative conductivity does not behave completely linear with emissivity for all pore shapes. This will be addressed in future studies, together with the influence of the matrix's thermal conductivity. Caution should therefore be applied when extending the results to low emissivities. The parameters and studied values are listed in Table 1. All mutual combinations are studied, hence covering a very broad range of possible elliptic pore shapes.

Table 1:
Studied parameters for 2D elliptic pores.

PARAM.	VALUES
a [mm]	0.1 – 0.25 – 0.5 – 0.75 – 1 – 1.5 – 2
b/a [-]	0.33 – 0.5 – 0.75 – 1
α [°]	0 – 18 – 36 – 54 – 72 – 90
T_{mean} [K]	263 – 273 – 283 – 293 – 303 – 313 – 323

The heat flow through the square is simulated including radiative heat transfer inside the elliptical pore using the view factor method in *COMSOL*. The effective thermal conductivity $\lambda_{eff,with\ direct\ rad}$ of the square is obtained via the Fourier formula. Subsequently, the same simulation is performed without including radiative heat transfer, resulting in a $\lambda_{eff,no\ rad}$. Finally, a search algorithm determines the equivalent $\lambda_{rad,pore,numerical}$ that should be added to the thermal conductivity of the air inside the pore so the relative error defined in Eq. 4 is smaller than 0.1%:

$$\frac{\lambda_{eff,with\ direct\ rad} - \lambda_{eff,with\ conductive\ rad}}{\lambda_{eff,with\ direct\ rad} - \lambda_{eff,no\ rad}} \quad (4)$$

The determined values for $\lambda_{rad,pore,numerical}$ show to be perfectly related to the temperature according to the T^3 term in Loeb's formula. For every pore the resulting geometrical factor γ can then be calculated as:

$$\gamma_{pore} = \frac{\lambda_{rad,pore,numerical}}{4 * \epsilon * \sigma * T^3 * d_{max}} \quad (5)$$

As expected, it was found that γ depends strongly on the geometrical parameters 'a', 'b/a' and ' α '. To avoid calculating these 3 parameters for every pore in future studies, a new, more easy to calculate factor is introduced combining the effect of all 3 geometrical parameters:

$$S_{f,i} = \frac{MH_{pore}}{MD_{pore}} \quad (6)$$

$S_{f,i}$ = the slenderness factor in direction 'i' of the cube [-]; i = the direction of the heat flow; MH_{pore} = the mean height of the pore, calculated perpendicular to the direction 'i' [m]; MD_{pore} = the mean distance of the pore, calculated parallel to the direction 'i' [m].

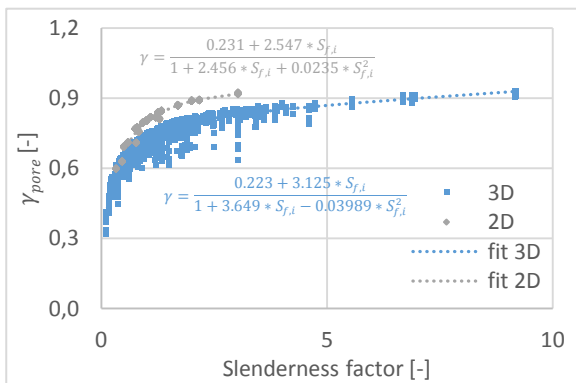


Figure 6: Relation between γ_{pore} and the slenderness factor (for 2D and for 3D pores)

A low slenderness value means that the pore is elongated in the direction of the heat flow while a high value means the pore is elongated in a direction perpendicular to the heat flow. A circular pore has by definition a slenderness of 1. Important to notice is that the slenderness of a pore depends on the direction of the heat flow. Furthermore, we propose to replace the maximum distance ' d_{max} ' used in Loeb's formula (Eq. 3) with the mean distance MD_{pore} , for more consistency in the formula. This is also adapted in the calculation of γ for every pore. The relation between γ and the slenderness factor is shown in Figure 6.

It can be seen that a very close relation exists between the factor γ_{pore} and the slenderness factor. The results furthermore confirm the intuitive idea that a vertically elongated ellips, with a high slenderness factor, has a larger γ and hence higher radiative heat transfer. The fitted relation between both is used to adapt Loeb's formula to:

$$\lambda_{rad,pore,analytical} = \frac{4 * \epsilon * \sigma * T^3 * MD_{pore} * (0.231 + 2.547 * S_{f,i})}{1 + 2.456 * S_{f,i} + 0.0235 * S_{f,i}^2} \quad (7)$$

Figure 7 compares for all the pores the analytical and numerical calculation of $\lambda_{rad,pore}$, showing good agreement.

3D calculation of radiation in pores

The same methodology as described for 2D pores is applied for the 3D case. A cube containing one ellipsoidal pore is simulated modelling radiative heat transfer directly using view factors and subsequently determining the equivalent radiative thermal conductivity of the pore. The parameters in 2D are extended with the length c of the short axis in the 3rd dimension, and 2 other angles to allow the pore to have any form and orientation. Only one temperature of 293 K is studied since the 2D calculations confirmed already the adoption of T^3 in Loeb's formula. For the emissivity, again only a value of 0.9 is used, keeping in mind the remarks made under the 2D calculations.

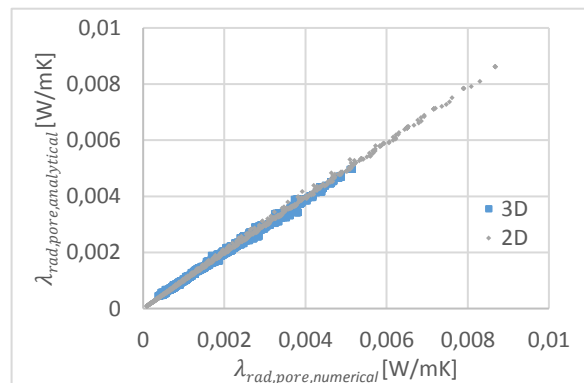


Figure 7: Comparison of numerical and analytical calculation of $\lambda_{rad,pore}$ (for 2D and 3D pores)

The combination of all the parameters and their studied values are listed in Table 2.

Table 2:
Studied parameters for 3D ellipsoidal pores.

PARAM.	VALUES
a [mm]	0.5 – 1 – 1.5 – 2
b/a [-]	0.33 – 0.5 – 0.75 – 1
c/a [-]	0.33 – 0.5 – 0.75 – 1
α_1 [°]	0 – 30 – 60 – 90
α_2 [°]	0 – 30 – 60 – 90
α_3 [°]	0 – 30 – 60 – 90

The slenderness factor is now extended to the 3rd dimension by incorporating the mean width MW_{pore} of the pore:

$$S_{f,i} = \frac{MH_{pore} * MW_{pore}}{(MD_{pore})^2} \quad (8)$$

The geometrical factor γ can again be calculated using Eq. 5 where again the distance of the pore is replaced with the mean distance. A good relation between the slenderness factor and γ appears also for 3D pores, as shown in Figure 6.

The Loeb formula can be expanded in an analogous manner as the 2D case:

$$\lambda_{rad,pore,analytical} = \frac{4 * \epsilon * \sigma * T^3 * MD_{pore} * (0.223 + 3.125 * S_{f,i})}{1 + 3.649 * S_{f,i} - 0.03989 * S_{f,i}^2} \quad (9)$$

Figure 7 compares for all the pores the analytical and numerical calculation of $\lambda_{rad,pore}$. Good agreement is again obtained demonstrating the validity of the analytical approximation.

Implementation in Matlab

The adapted Loeb formula is used to assign an equivalent radiative thermal conductivity to every pore in the sample based on the pore's slenderness factor. A number of Matlab scripts have been implemented with the purpose of calculating this slenderness factor for every pore.

The first step consists of splitting the pore space into separated pore clusters. Indeed, in high porosity materials often a large part of the pores are interconnected with smaller connection zones. However, when the opening width of the connection between two pore clusters is relatively small, thermal radiation travelling from one cluster to the other can effectively be neglected. Hence the 2 pore clusters should be separated and a different slenderness factor for both clusters should be calculated. The splitting of the pores is executed according to the watershed-based procedure described in Morpho+ (Brabant et al. 2011), by calculating the distance transform of the binary

image matrix. This procedure will split all the pores at their narrowest point, resulting in a set of completely disconnected pores. However, when pore clusters were originally connected via a relatively large opening width, their splitting is not desirable since thermal radiation travelling between 2 pore clusters will have an important impact in this case. Therefore, the rejoining procedure described in Morpho+ is also implemented. This procedure first calculates the radii of the maximum inscribed balls of 2 originally connected pores. Subsequently, the largest of both radii is compared to the radius of the maximum inscribed circle in the connection zone between both pores. If the ratio of these radii is larger than a set value (the rejoin factor R_f), the pores are rejoined:

$$\frac{r_{inscribed\ circle\ of\ connection}}{\max(r_{inscribed\ balls\ of\ pores})} > R_f \quad (10)$$

If the rejoin factor is set to 0, all separated pores will be rejoined, if set to 1 all pores will stay separated. The binary image matrix is hence transformed to an image matrix consisting of several pore clusters, each arising from a number of pores that pass the rejoining test. For every pore cluster the slenderness factor is calculated using Eq. 8, which is finally used to calculate the equivalent radiative thermal conductivity in every pore cluster. Since these conductivities can simply be added to the thermal conductivity of the gas in the pores, the whole simulation procedure remains the same as described in the first section.

PRELIMINARY INVESTIGATIONS USING THE MODEL

The model is used to investigate the impact of both the difference between 2D and 3D simulations and the influence of thermal radiation on the total heat transfer. A synthetic sample is generated, having a porosity of 81.73 %, a side length of 1 cm and a pore size distribution as shown in Figure 8 (left). The resolution is set to 600³, the mesh size parameter to $L_{sample}/50$. The sample is shown in Figure 8 (right).

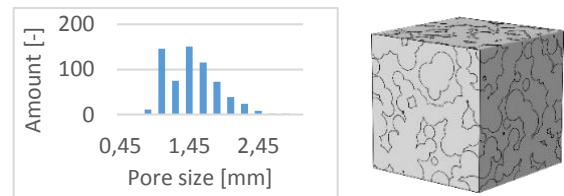


Figure 8: The pore size distribution (left) and a render of the investigated sample (right)

The effective thermal conductivity excluding thermal radiation is calculated with the model, resulting in a value of 0.064 W/mK.

2D versus 3D calculations

For simplification, a lot of calculation models use a 2D approach with an image acquired via generating

algorithms or scanning electron microscopy as input. This is however a strong simplification of the real microstructure and the pathways of the heat flow through the material. This is demonstrated on the generated 3D sample: five equidistant 2D slices are cut through the sample, starting and finishing with the bottom and upper slice. The middle slice is shown in Figure 9.

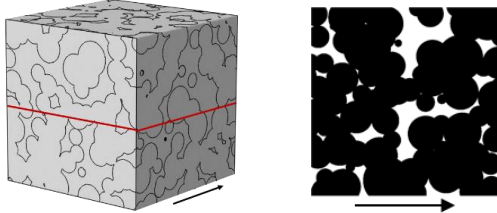


Figure 9: Location of the slice (left) and 2D view of the slice (right)

The effective thermal conductivity of every slice is calculated using the model, excluding thermal radiation. The resulting ETC of the respective slices are shown in Figure 10.

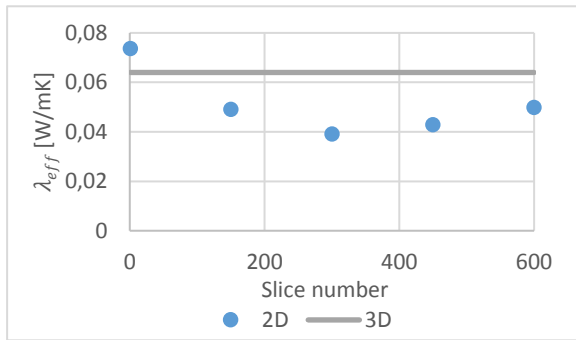


Figure 10: 2D versus 3D calculation.

A first conclusion is that the 2D calculated values differ a lot from each other, due to the different porosity and microstructure of each slice. Furthermore, most of the values are lower than the 3D value, and so is also the average of the 2D values. This is due to the fact that in 3D the heat flow can pass the 2D obstructions in the 3rd dimension. Hence, 2D calculations will result in a strong underestimation of the true effective thermal conductivity.

Influence of radiation

The effect of radiative heat transfer on the ETC of the synthetic sample of Figure 8 is investigated. This is done through the method described before, incorporating radiation at the pore level. A rejoin factor of 0.5 is applied, leading to a subdivision of the pores in 13 pore clusters. For each cluster, the geometrical factor γ is calculated using the cluster's slenderness factor previously defined.

To reduce computation time, the mean sample temperature is used in the adapted Loeb formula

instead of the local temperature. With the temperature difference across the sample being set to 10 K, this should induce only a very small error. The simulation is performed at 3 different mean temperatures: 273 K, 293 K and 313 K. The results are summarized in Table 3, together with the ETC of the sample excluding thermal radiation. The relative difference with this value is also shown.

Table 3:
ETC at several temperatures, with and without radiation

T_{MEAN} [K]	ETC [W/MK]	REL. DIFFERENCE
No radiation	0.064	N.A.
273	0.0713	10.24 %
293	0.0730	12.33 %
313	0.0749	14.55 %

It is clear that thermal radiation has a non-negligible influence. Even at a mean temperature of 273 K, the ETC is found to be 10 % higher than the one neglecting thermal radiation. As expected, this increases with increasing temperature. It is furthermore expected that the influence will be even larger at higher porosities.

The model results are compared with two analytical macroscale calculations of the thermal radiation. The first is based on the calculation of the mean extinction coefficient following an empirical formula from Hsu & Howell (Howell 2000) for open-celled reticulated ceramic foams:

$$\lambda_{rad,macro} = \frac{16 * \sigma * T^3}{3 * \kappa} \quad (11)$$

$$\kappa = \frac{3}{d_{pore,mean}} * (1 - \phi) \quad (12)$$

The other method is a simplified calculation for closed cell materials derived by Batty et al. (1984):

$$\lambda_{rad,macro} = \frac{4 * \sigma * T^3 * d_{pore,mean}}{\frac{2}{\epsilon} - 1} \quad (13)$$

The values for $\lambda_{rad,macro}$ are summed with the thermal conductivity of the sample calculated without thermal radiation (0.064 W/mK). The results of the two analytical macroscale approximations are shown in Figure 11 as a function of mean temperature, alongside the results obtained with the model.

As expected, the model results lie in between both approximations, since the synthetic sample is neither completely closed- or open-celled. The much higher values for the Hsu & Howell model can be attributed to the fact that their formula is derived for very open porous ceramic foams. Though further verification studies are still needed, this is already a strong first indication of the possibilities of this microscale approach.

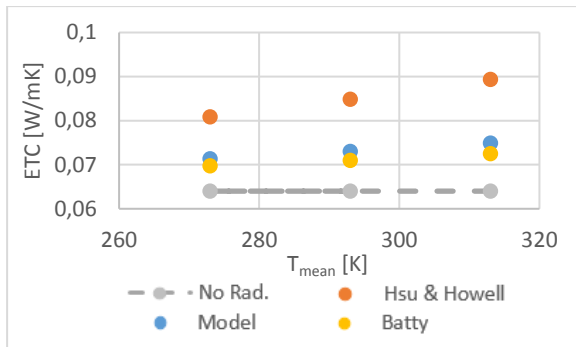


Figure 11: ETC at several temperatures, with and without radiation

CONCLUSION

This paper introduced a model framework for performing 3D heat simulations on microstructures of porous samples. Good agreement was found for an elementary type of pore structure for porosities between 10 % and 90 %. The method of Loeb for incorporating thermal radiation at the microscale has been implemented and extended on the basis of a broad set of pore scale radiative heat transfer simulations. A slenderness factor has been introduced, allowing for an accurate calculation of Loeb's geometrical factor. This makes it possible for including radiative heat transfer at the pore scale, based on local structural characteristics instead of Loeb's non-intuitive factor γ . The model is subsequently used to show the discrepancy between 2D and 3D simulations, and to show the importance of including thermal radiation.

ACKNOWLEDGEMENT

Research funded by a Ph. D. grant of the Agency for Innovation by Science and Technology (IWT).

REFERENCES

- Alliez, P. et al., 2015. 3D Mesh Generation. In *CGAL User and Reference Manual*. CGAL Editorial Board.
- Bakker, K., Kwast, H. & Cordfunke, E.H.P., 1995. The contribution of thermal radiation to the thermal conductivity of porous UO₂. *Journal of Nuclear Materials*, 223, pp.135–142.
- Batty, W.J., Probert, S.D. & O'Callaghan, P.W., 1984. Apparent thermal conductivities of high-porosity cellular insulants. *Applied Energy*, 18(2), pp.117–135.
- Brabant, L. et al., 2011. Three-dimensional analysis of high-resolution X-ray computed tomography data with Morpho+. *Microscopy and Microanalysis*, 17(2), pp.252 – 263.
- Carson, J. et al., 2003. An analysis of the influence of material structure on the effective thermal conductivity of theoretical porous materials using finite element simulations. *International Journal of Refrigeration*, 26(8), pp.873–880.
- Chen, J. et al., 2015. Evaluation of thermal conductivity of asphalt concrete with heterogeneous microstructure. *Applied Thermal Engineering*, 84, pp.368–374.
- Clyne, T.W. et al., 2006. Porous materials for thermal management under extreme conditions. *Philosophical transactions. Series A, Mathematical, physical, and engineering sciences*, 364(1838), pp.125–146.
- Fang, Q. & Boas, D.A., 2009. Tetrahedral mesh generation from volumetric binary and gray scale images. In *Proceedings IEEE International Symposium on Biomedical Imaging*. pp. 1142–1145.
- Fitzgerald, S. & Strieder, W., 1997. Radiation heat transfer across a compressed spheroidal cavity. *AIChE Journal*, 43(9), pp.2368–2372.
- Gaiselmann, G. et al., 2014. Quantitative relationships between microstructure and effective transport properties based on virtual materials testing. *AIChE Journal*, 60(6), pp.1983–1999.
- Howell, J.R., 2000. Part VI: Radiative transfer in porous media. In K. Vafai, ed. *Handbook of Porous Media*. pp. 663–698.
- Loeb, A., 1954. Thermal Conductivity: VIII, A theory of thermal conductivity of porous materials. *Journal of the American Ceramic Society*, 37(2), pp.96–99.
- McKenzie, D.R., McPhedran, R.C. & Derrick, G.H., 1978. The conductivity of lattices of spheres II. The body centred and face centred cubic lattices. *Proceeding of the Royal Society of London. Series A, Mathematical and Physical Sciences*, 362(1709), pp.211–232.
- Randrianalisoa, J. & Baillis, D., 2014. Thermal conductive and radiative properties of solid foams: Traditional and recent advanced modelling approaches. *Comptes Rendus Physique*, 15(8-9), pp.683–695.
- She, W., Zhang, Y. & Jones, M.R., 2014. Three-dimensional numerical modeling and simulation of the thermal properties of foamed concrete. *Construction and Building Materials*, 50, pp.421–431.
- Wang, M. & Pan, N., 2008. Modeling and prediction of the effective thermal conductivity of random open-cell porous foams. *International Journal of Heat and Mass Transfer*, 51(5-6), pp.1325–1331.

RESULTS OF BELGIAN QUALITY CONTROL FRAMEWORK FOR CAVITY WALL INSULATION

A. Janssens, M. Delghust, N. Van den Bossche
Research Group Building Physics, Construction and Services
Ghent University (UGent), Gent, Belgium

ABSTRACT

Since 2012 a quality control system is in operation in Belgium to provide confidence in the quality of the works of cavity wall insulation in existing walls. When the works are in line with the quality framework, the installer may provide a declaration of conformity to the client, which he can use to receive subsidies or for energy performance certification.

A field study was performed to analyze the relationship between the information provided by installers in the declaration of conformity, the results of the conformity checks performed by the certification organization and the effective cavity wall performance measured on site.

INTRODUCTION

The mass market application of cavity wall insulation in existing walls is an important measure to achieve a reduction of the energy use and greenhouse gas emissions related to heating the existing Belgian housing stock. Approximately 25% of the existing Flemish housing stock still has non-insulated cavity walls today ($U \approx 1.5 \text{ W/m}^2\text{K}$), with cavity widths larger than 50 mm in more than 80% of the houses.

Since 2012 a quality control system is in operation in Belgium to provide confidence in the quality of the works of cavity wall insulation in existing cavity walls. This technique allows to insulate existing cavity walls by blowing or pumping insulation product into the empty cavity through pre-drilled holes in the outer or inner masonry leaf.

Existing cavity walls are considered suitable for correct installation of thermal insulation on following conditions: (1) the minimum cavity width is 50 mm, (2) the façade and wall are in good condition, with no sign of damage or cracks (3) the driving rain load is limited – façade height should typically be lower than 8m, (4) the indoor moisture load is limited (STS 2012).

For cavity wall insulation to perform correctly, three criteria must be met: (1) the building must be inspected and shown to be suitable, (2) the insulation system must have been tested and shown to meet a

number of criteria and (3) trained technicians must carry out the installation to a high standard (STS 2012, Janssens et al. 2012).

When the works are performed according to these criteria, the installer may provide a declaration of conformity to the client. In the Flemish region in Belgium the authorities subsidize the installation of cavity wall insulation in existing walls on the condition that a declaration of conformity is presented by the building owner. Furthermore, if the installation of insulation is part of a major renovation for which energy performance requirements apply, the retrofitted cavity wall should have a declaration of conformity and achieve a U-value not higher than $0.55 \text{ W/m}^2\text{K}$.

The whole system is managed by a quality control and certification organization which is responsible for the assessment and approval of products and systems, the training of installers, and the conformity checks on building sites. The Belgian technical approval authority in construction (UBAte) and the Belgian construction certification association (BCCA) take up this role. Typically over 1500 installations per month are executed within the system (on a market of 600.000 houses with non-insulated cavity walls) (www.ikisoleermijnspouw.be, 2015).

The reported cavity width is an important element in deciding whether the cavity may be filled with insulation product, and in defining the U-value of the wall in EPC-reports. Therefore the installer should measure the cavity width at least at one point per façade during inspection, and at least once every 10 m² façade surface during installation, with a minimum of 3 measurements for each façade.

Previous studies showed that the quality of installation of cavity wall insulation might be a concern. For example, a field study was carried out in the UK to determine the as built thermal performance of a sample of 70 dwellings during 2005 and 2006 based on in-situ U-value measurements (Doran and Carr 2008). The study showed that the actual realised improvements to U-values were in many cases less than would be expected on the basis of calculating U-values. The improvement in thermal resistance was,

on average, 38% less than that which would be expected on the basis of measured cavity widths.

Since the quality control system in Belgium has been operational for a relatively small time span, and the conformity checks are performed on a small sample of all installations, it is unclear whether the system effectively meets the objectives of improving the quality of the works. Therefore a field study was performed to analyze the relationship between the information provided by the installers in the declaration of conformity, the results of the conformity checks performed by the certification organization and the effective cavity wall performance on site.

The analysis of the field study is focusing on both the compliance of input data and the quality of the works by confronting the different sources of information:

- Compliance of input data: to what extent is the information provided by installers conforming with specifications (wall area, cavity width,...).
- Quality of the works: relation between measured U-values and theoretical U-value based on reported cavity width and insulation product data.

METHODS

The study is based on the field investigation of 26 detached and semi-detached houses, built between 1900 and 1995, with retrofit cavity wall insulation installed in 2012 or 2013 under the quality control framework. The field measurements were performed in winter 2014. The projects were selected in collaboration with BCCA, the organization responsible for the independent audits of certified materials and installers. The selected case studies in the sample were scattered over Flanders, to get representative results. Next to that, the case studies can be split according to two parameters: type of insulation product and conformity after installation; which is shown in Table 1.

Three insulation products are considered, as these are the only products with technical approval used on the Belgian market: loose-fill glass wool, EPS-beads and PUR-foam (for this application typically of the open cellular type). More than half of the houses in the sample were checked by the certification organization and have an auditing report available. During an audit on site the assessor checks whether the technical guidelines for inspection and product installation are correctly followed, and takes material samples for further analysis of product properties. It was also decided to include a number of projects for which the declaration of conformity was not granted due to non-compliance to one of the installation guidelines. Typical non-conformities are of a procedural nature,

eg incorrect registration of tests of the installation equipment prior to installation.

The share of assessed and non-compliant projects in the sample is not representative for the amount of projects which are checked in practice or for the amount of projects that are non-compliant. These cases were included in the sample to be able to investigate whether the occurrence of independent assessments, or the occurrence of non-conformities had an influence on the performance of the insulated cavity walls.

Table 1:

Number of cases included in each control group

	Check BCCA Compliant (CC)	Check BCCA Non-compliant (CNC)	Not checked by BCCA (NC)
MW	3	2	4
EPS	3	2	3
PUR	3	2	4

For each case study information was collected from the certification organization and the owners, to allow for an accurate estimation of the U-value of the walls, and for an assessment of the correctness of input data provided by the installers. The following information was used for further analysis:

- the declared thermal conductivity of the insulation product λ_D , available in the technical approval document
- cavity width d , provided in the inspection and installation reports by the installers (in 12 out of 26 projects the installer only reported a single value, contrary to specifications)
- results of conformity checks, provided in auditing reports by the independent assessor
- wall composition, derived from analysis of architectural drawings and from observation on site.

U-value calculation

For each project the collected information was used to estimate the wall U-value. The correctness of data provided by the installers as well as the quality of the works was assessed based on the comparison between the U-value measured on site and the calculated U-values.

The design value of a retrofit insulated cavity wall is calculated according to section 7.2 of STS 71-1 (STS 2012). This method is also included in the specifications for defining transmission characteristics in the framework of energy performance regulations (TRD 2014), which are in force if the installation of insulation is part of a major